Measurement of the absolute ν_μ-CCQE cross section at the SciBooNE experiment

–Tesis Doctoral–

José Luis Alcaraz Aunión

supervised by Dr. Federico Sánchez Nieto

Institut de Física d'Altes Energies
Universitat Autònoma de Barcelona

Barcelona, July 2010

Agradecimientos

Me gustaría empezar agradeciendo a mi tutor de tesis, Federico Sánchez, su apoyo, tiempo y dedicación hacia mí y el trabajo aquí presentado. I would like to thanks to the SciBooNE collaboration people for their support and the days we enjoyed together at Fermilab. Thanks to Nakaji for his patience answering thousands of my e-mails and always available for helping me. Gracias a mis compañeros de neutrinos, con quien he compartido agradables momentos. A Gabriel por su ayuda y amistad.

Un agradecimiento a todos mis amigos por su apoyo y paciencia, aguantando mis quejas cada vez que me preguntaban por la tesis. També als amics que he fet aquí a Barcelona, pels seus consells i la seva gran amistat, gràcies per fer-me sentir com a casa.

Quisiera agradecer de forma muy afectiva a Joan y Michel. A Joan por su compañerismo, su amistad y por aquellas inolvidables estancias en Fermilab. A Michel por su ayuda, con aquellos interminables e-mails de sugerencias que tanto me han enseñado, por su optimismo que tanto he necesitado y por su amistad.

Un cariñoso agradecimiento a mis padres por su constante apoyo. A mis suegros, por cuidar de Angels y cambiar los pañales de mi hijo Marc en la recta final de este trabajo.

Por último, el agradecimiento más especial y cariñoso para mi mujer Angels, que desde el principio ha estado a mi lado, compartiendo los problemas y las ilusiones que un trabajo como este conlleva. Por su paciencia y comprensión, y por entender el sacrificio de tiempo personal que, en ocasiones, ha necesitado este trabajo. Te quiero.

Abstract

This thesis presents the measurement of the charged current quasi-elastic (CCQE) neutrino-nucleon cross section at neutrino energies around 1 GeV. This measurement has two main physical motivations. On one hand, the neutrino-nucleon interactions at few GeV is a region where existing old data are sparse and with low statistics. The current measurement populates low energy regions with higher statistics and precision than previous experiments. On the other hand, the CCQE interaction is the most useful interaction in neutrino oscillation experiments. The CCQE channel is used to measure the initial and final neutrino fluxes in order to determine the neutrino fraction that disappeared. The neutrino oscillation experiments work at low neutrino energies, so precise measurement of CCQE interactions are essential for flux measurements.

The main goal of this thesis is to measure the CCQE absolute neutrino cross section from the SciBooNE data. The SciBar Booster Neutrino Experiment (SciBooNE) is a neutrino and anti-neutrino scattering off experiment. The neutrino energy spectrum works at energies around 1 GeV. SciBooNE was running from June 8th 2007 to August 18th 2008. In that period, the experiment collected a total of 2.65×10^{20} protons on target (POT). This thesis has used full data collection in neutrino mode 0.99×10^{20} POT.

A CCQE selection cut has been performed, achieving around 70% pure CCQE sample. A fit method has been exclusively developed to determine the absolute CCQE cross section, presenting results in a neutrino energy range from 0.2 to 2 GeV. The results are compatible with the NEUT predictions. The SciBooNE measurement has been compared with both Carbon (MiniBoonE) and deuterium (ANL and BNL) target experiments, showing a good agreement in both cases.

Contents

Chapter 1

Neutrino Physics

This chapter is dedicated to the neutrino physics. The first section is a brief cronology of the main hits of the neutrino in the history. The neutrino properties are detailed in the second section. The third section describes the neutrino oscillation model. The last sections are dedicated to the weak interactions.

1.1 Introduction

The neutrino "was born" in the year 1930, when W. Pauli attempted to explain the continuous spectrum of the beta-decay particles through *"a way out for saving the law of conservation of energy"* [1]. Twenty six years later, the neutrino particle was detected by the first time in the Cowan and Reines experiment[2]. The Cowan and Reines experiment detected neutrinos coming from a nuclear reactor (the Savannah River nuclear reactor at South Carolina, EEUU).

In 1962, the BNL laboratory prepared the first experiment with neutrinos produced in an accelerator. The neutrino beam was generated through pion decays produced by interactions of accelerated protons with a target. The experiment proved the existente of two kind of neutrinos [3](ν_μ and ν_e).

At the end of the sixties (1968), the experiment of R. Davis Jr.[4], that measured the solar neutrino flux, shown a solar neutrino deficit compared with the theoretical predictions. The neutrino oscillation model[] demostrated to be the best candidate to explain such results. In the next 30 years, many other neutrino experiments [5, 6, 7] not only have confirmed the Davis results but also have validated the neutrino oscillation model.

1.2 Neutrino Properties

The current standard model of the particle physics classifies the fundamental components of the matter in the quark and the lepton sectors (see 1.1). Both may be divided in three families: u and d quarks and ν_e and e leptons to the first family; c,d, ν_μ and μ to the second family; t, b,ν_τ and τ to the third family. Each lepton family has assigned a different conserved lepton number, identified as electron, muon and tau flavours. Then, the neutrinos are characterized by a flavour type.

The components of matter are fermions with spin 1/2. However, the force carriers (photons, gluons, Z^0 and $W^\pm$) are bossons with spin 1. Although the figure 1.1 only shows the matter components, the anti-matter follows the same classification.

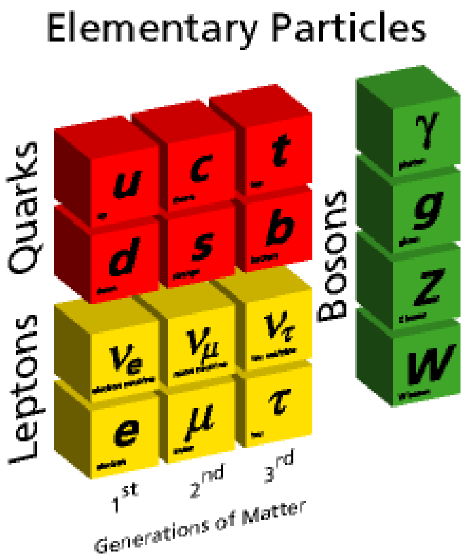

Figure 1.1: The basic elements of the Standard Model, quarks, leptons and force carries (green block).

The neutrinos are only affected by the weak interactions, responsibles of the beta decay prosesses. The neutrino weak interactions are not invariant under spatial inversion symmetry, i.e. do not conserve parity[8].

The Standard Model considers the neutrino as a massless particle. In such an assumption, the electroweak theory[9, 10, 11] was developed. However, several neutrino experiments, based on neutrino flux measurements from the sun [5], the atmosphere[6], nuclear reactors[12] and accelerators[7], has shown evidence of neutrino oscillation. This phenomena can only occur when the neutrino has mass and the masses of the neutrinos are different. Theories beyond the standard model, like the neutrino oscillation model, has been incorported to include neutrino masses.

The neutrino oscillation experiments can only measure differences of squared neutrino masses. An absolute value of the neutrino mass requires complementary techniques. A common technique consists in to measure the endpoint region of the β-spectrum from Tritium decay, which is expected to be shifted for massive neutrinos. The results of this technique have reported upper limits[13], with indications that neutrino masses are orders of magnitud smaller than the rest of the fundamental particles (see mass scale 1.2).

Another technique to measure the absolute neutrino mass is based on the search of double beta decay ($0\nu\beta\beta$) processes. The neutrino mass in these cases is proportional to the decay rate. However, this process can only be observed if the neutrino behaves as a Majorana particle, i.e., the neutrino and anti-neutrino are the same paritcle. Up to now, experiments using this technique [14] has not shown indications of $0\nu\beta\beta$.

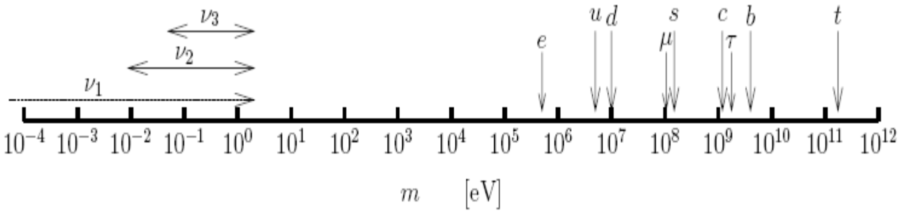

Figure 1.2: Mass scale of the fundamental particles[15].

1.2.1 Neutrino oscillation

The neutrino oscillation is closely related with the non-zero neutrino mass. This fact requires a theoretical description beyond the Standard Model. The neutrino oscillation model is a minimal extension of the Standard Model. In this model, the neutrinos produced by the weak interactions, so-called weak eigenstates, are not states of definite mass but a linear superposition of mass eigenstates. Such a relation is usually given by a mixing matrix. Assuming only two neutrino species, the neutrino mixing equation can be expressed as follows:

$$\begin{pmatrix} \nu_\alpha \\ \nu_\beta \end{pmatrix} = \begin{pmatrix} \cos\theta & \sin\theta \\ -\sin\theta & \cos\theta \end{pmatrix} \begin{pmatrix} \nu_1 \\ \nu_2 \end{pmatrix} \tag{1.1}$$

where (ν_α, ν_β) and (ν_1, ν_2) correspond to the weak and the mass eigenstates. The α and β represent the neutrino flavours and m_1 and m_2 the mass eigenvalues associated to the mass eigenstates. θ is the neutrino mixing angle.

Taking now the relation (1.1), a weak eigenstate (ν_α) produced in the instant time t=0 can be represented as follows:

$$\nu_\alpha(t=0) = sin\theta|\nu_1> + cos\theta|\nu_2> . \tag{1.2}$$

However, in an instant time $t \neq 0$, each mass eigenstate propagates with a distinct phase factor. Then, the equation (1.2) results,

$$\nu_\alpha(t) = |\nu_1> sin\theta e^{-iE_1t-px} + |\nu_2> cos\theta e^{-iE_2t-px}, \tag{1.3}$$

where $E_{1,2}$ are the energies of the mass eigenstates with momentum p. In the extreme relativistic approximation for tiny neutrino masses $(m << p)$,

$$E_{1,2} \approx p + \frac{m_{1,2}^2}{2p}, \tag{1.4}$$

the equation (1.3) is simplified in the way:

$$\nu_\alpha(t) = |\nu_1> cos\theta e^{-\frac{im_1^2L}{2E}} + |\nu_2> sin\theta e^{-\frac{im_2^2L}{2E}}, \tag{1.5}$$

where here E=p and L is the distance from the neutrino production to the neutrino detection. Hence, after a propagation distance L, the probability of finding out a different neutrino flavour results:

$$P(\nu_\alpha \to \nu_\beta, t) = |<\nu_{beta}|\nu_\alpha(t)>|^2 = sin^2 2\theta sin^2\frac{\Delta m^2 L}{4E}, \tag{1.6}$$

where $\Delta m^2 = m_2^2 - m_1^2$ is the square of difference of mass.

1.3 The weak interactions

Since the Pauli prediction of the neutrino, this particle has played an important role in the knowledge of the weak interacttions. Fermi was the first including the neutrino particle to describe the β-decay process. The most important prediction of the electroweak theroy, the neutral currents, where discovered with neutrino interactions at the Gargamelle bubble chamber experiment [16]. The following two subsections present a brief historial introduction to the weak interactions, from the Fermi theory to the most recent electroweak interactions.

1.3.1 Nuclear β-decay: The Fermi theory

The Fermi theory, published by E. Fermi in 1934[17], describes the beta decay process as the change of the neutron into a proton with the production of two additional particles, an electron and the particle postuled by Pauli, the neutrino. The reactions can be written as follows:

$$n \rightarrow p + e^{-} + \bar{\nu_e}. \tag{1.7}$$

The beta decay process can be treated as a transition probability, expressed by the Fermi's Golden Rule as follows:

$$\lambda_{if} = \frac{2\pi}{\hbar} |\mathcal{M}_{if}|^2 \rho_f, \tag{1.8}$$

where $\mathcal{M}_{if}$ represents the transition amplitude and ρ_f the density of the final states. The density of final states can be determined by the number of ways it is possible to share out the available energy ($E_0 \rightarrow E_0 + dE_0$) between the final states (p, e and ν).

The transition amplitude ($\mathcal{M}$) includes the interaction occurred in the process. Fermi formulated the weak interaction in analogy to the electromagnetic interactions, descrbied by the Quantum electrodynamics (QCD) theory. So in order to understand the Fermi theory, let's start first with the electromagnetic case. Consider the process of electromagnetic scattering given by the following reaction:

$$e + p \rightarrow e + p. \tag{1.9}$$

In such a reaction, the interaction is described as the interaction of two currents, a leptonic ($J_{leptonic}$) and a barionic (J_{barion}) current, via ex-change of a virtual photon. The invariant amplitude ($\mathcal{M}$) is then expressed as follows [18]:

$$\mathcal{M} = \frac{e^2}{q^2} J_{barion} \times J_{lepton}, \tag{1.10}$$

where e is the electron charge and q the momentum transfer. The electromagnetic currents are expressed in terms of relativistic fermions. The nucleons (protons and neutrons) are considered structureless Dirac particles, matemaically described by two-component spinors (ψ) operated by a 4×4 matrix operator (Θ). In the electromagnetic case, the involved vector operator is defined in terms of γ matrices, $\Theta_{em} = \gamma_4 \gamma_\mu$. Thus, the currents can be expressed as follows:

$$\begin{aligned} J_{lepton} &= \psi_e^\star \Theta_{em} \psi_e = \psi_e^\star \gamma_4 \gamma_\mu \psi_e = \bar{\psi}_e \gamma_\mu \psi_e & (1.11) \\ J_{barion} &= \bar{\psi}_p \gamma_\mu \psi_p, & (1.12) \end{aligned}$$

where $\bar{\psi} = \psi^\star \gamma_4$. The γ's correspond to 4×4 matrices represented as follows:

$$\begin{aligned} \gamma_k &= \begin{pmatrix} 0 & -i\sigma_k \\ i\sigma_k & 0 \end{pmatrix}, k = 1, 2, 3. & (1.13) \\ \gamma_4 &= \begin{pmatrix} I & 0 \\ 0 & -I \end{pmatrix}, & (1.14) \end{aligned}$$

where I and σ_k represent the 2×2 identity and Pauli matrices, respectively.

The invariant amplitud from equation (1.10) can be then reformulated as follows:

$$\mathcal{M} = \frac{e^2}{q^2} (\bar{\psi}_p \gamma_\mu \psi_p)(\bar{\psi}_e \gamma^\mu \psi_e), \tag{1.15}$$

where expressions for leptonic and barionic current (1.12) have been included. At this point and by analogy with the expression 1.15, the invariant amplitud for *beta*-decay processes can be formulated as follows:

$$\mathcal{M} = G_F \cdot J^{weak}_{barion} \cdot J^{weak}_{lepton} = G_F (\psi_p \gamma_\mu \psi_n)(\psi_e \gamma^\mu \psi_\nu), \tag{1.16}$$

where the *beta*-decay reaction (1.7) has been re-written in the form $n+\nu \rightarrow p+e$. In this case, G_F corresponds with the weak coupling constant (the Fermi constant).

Two important attributes can be remarked from equation (1.16). First, all the fields are evaluated at the same point in space time i.e., there is no $1/q^2$ factor. The weak interaction in the Fermi theory is treated as short range or point-like interaction. Second, the electric charges of the lepton and baryion currents change by one unit in the interaction, something that does not happen in electromagnetic interactions. For such a reason, the β-decay is referred as charge-changing weak interaction.

In 1956, Lee and Yang predicted that weak interactions do not conserve parity[8]. One year later, the predictions were confirmed in an experiment carried out by Madame Wu[19]. The parity violation property was later included in the Fermi theory such that, the expression (1.16) is finally written as follows:

$$\mathcal{M} = \frac{G_F}{\sqrt{2}}(\psi_p \gamma_\mu (1 - g_A \gamma_5)\psi_n)(\psi_e \gamma^\mu (1 + \gamma_5)\psi_\nu), \tag{1.17}$$

where $\gamma_5 = \gamma_1\gamma_2\gamma_3\gamma_4$ and $g_A = -1.26$[20] for neutron decay.

The Fermi theory has represented a significant progress in describing charged current weak interactions. However, mathematical difficulties prevent this from being a complete theory. It was in the 1960's when an elegant unification of the electromagnetic an weak forces came out through the language of the group theory.

1.3.2 Toward the electroweak unification

The weak interaction based on the four-fermion Fermi model presents divergences when is applied to high energies. Several authors, like Yukawa[21], proposed a boson-exchange model to explain the charge-changing weak interactions. In this model, the weak interaction is mediated by the boson W. The boson introduces a propagator term $1/(q^2 + m^2)$ that reduces the divergences, although quadratic divergences still appears. The boson-exchange model leads to the Fermi point-like interaction at the limit of low momentum transfer (q^2), fig. 1.3.

The W bosson introduces itself divergencies, like the process $e^+e^- \to W^+W^-$, with a photon mediating the interaction. The divergence can be canceled by introducing ad hoc a neutral boson Z^0 (Glashow). In that case, the Z^0 coupling constant should be similar to the electromagnetic coupling constant. This discussion form part of the so-called electroweak theory, the unification theory of the weak and the electromagnetic interactions. The electroweak theory was

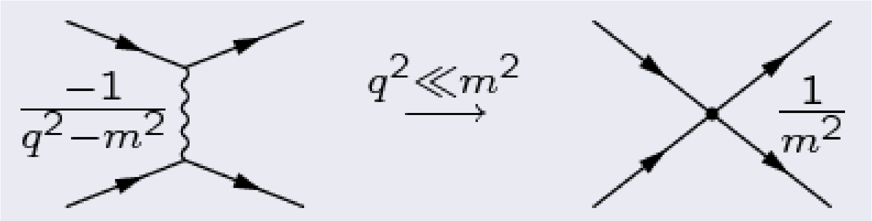

Figure 1.3: Left hand diagram represents a Feynman diagram showing the propagator of the interaction ($1/(q^2 - m^2)$), with q^2 and m representing the momentum transfer and the mass of the propagator bosson, respectively. In the case of low momentum transfer ($q^2 << m^2$), the diagram transforms in a point-like interaction described by the Fermi theory.

developed in 1967-1968 by Weinberg, Salam and Glashow[9, 10, 11]. Citing to Steven Weinberg[9]:

> *"Leptons interact only with photons, and with intermediate bosons that presumably mediate weak interactions. What could be more natural than to unite these spin-one bosons into a multiple of gauge fields.......We migh hope to understant these differences (between the boson masses and their coupling) by imagining that the symmetries relating the weak an electromagnetic interactions are exact symmetries of the Lagrangian but are broken by the vacuum."*

The electroweak theory makes important predictions like the existence of the weak neutral currents and the masses of the heavy bossons $W^{\pm}$ and Z^0.

The electroweak theroy is a gauge theory based on the symmetry group $SU(2)$ of "weak isospin" and $U(1)$ of "weak hypercharge". The fundamental vector bossons, responsible of the interaction, are expressed by the massless isovector triplet $W_\mu = (W_\mu^1, W_\mu^2, W_\mu^3)$ from SU(2) and a massless isosinglet B_μ from U(1), so-called weak eigenstates. As a result of spontaneous symmetry breaking, three bosons, denoted by $W_\mu^{\pm}$ and Z_μ^0, acquire mass (so-called mass eigenstates), and one, the A_μ identified as the photon, remains massless. The mass and weak eigenstates are related by a mixing matrix, as is discussed below.

The lagrangian associated to the electroweak interaction consists of an isotriple of vector fields (W_μ^i) coupled with strength g to the weak isospin current J_μ^i, together with a single vector field B_μ coupled to the weak hypercharged current J_μ^Y with strength g'. The expression is matematically expressed as follows:

$$L = g(J^i)^\mu \cdot W_\mu + g'(J^Y)^\mu B_\mu, \tag{1.18}$$

defining the weak hypercharge as Y= Q - I_3, with Q the electric charge and I_3 the third component of weak isospin. The hypercharge current is then written in the form

$$J^Y_\mu = J^{e.m.}_\mu + J^3_\mu, \tag{1.19}$$

where $J^{e.m.}_\mu$ is the electromagnetic current and J^3_μ the third component of isospin current J_μ. The charged ($W^\pm$) and neutral (Z_μ, A_μ) mass eigenstates bossons are related with the weak eigenstates (W_μ and B_μ) by the following linear combinations:

$$\begin{aligned} W^\pm &= \frac{1}{\sqrt{2}}(W^1_\mu \pm iW^2_\mu), && (1.20)\\ W^3_\mu &= \frac{gZ_\mu + g'A_\mu}{\sqrt{g^2+g'^2}} && (1.21)\\ B_\mu &= \frac{-g'Z_\mu + gA_\mu}{\sqrt{g^2+g'^2}} && (1.22) \end{aligned}$$

Hence, the expression 1.18 can be written, in terms of the mass eigenstate bossons, as follows:

$$\begin{aligned} L &= g(J^1_\mu W^1_\mu + J^2_\mu W^2_\mu) + g(J^3_\mu W^3_\mu) + g'(J^{e.m}_\mu + J^3_\mu)B_\mu \\ &= g/\sqrt{2}(J^-_\mu W^+_\mu + J^+_\mu W^-_\mu) + J^3_\mu(gW^3_\mu + g'B_\mu) + J^{e.m}_\mu g'B_\mu, \end{aligned}$$

where $J^\pm_\mu = J^1_\mu + iJ^2_\mu$. Inserting the expressions for W^3_μ and B_μ from 1.22 and setting

$$g'/g = tan\theta_W, \tag{1.23}$$

where θ_W is the weak mixing angle (Weinberg angle), the lagrangian of the electroweak interactions is finally expressed in the form:

$$L = \underbrace{\frac{g}{\sqrt{2}}(J_\mu^- W_\mu^+ + J_\mu^+ W_\mu^-)}_{\text{weak charge current}} + \underbrace{\frac{g}{cos\theta_W}(J_\mu^3 - sin^2\theta_w J_\mu^{e.m})Z_\mu}_{\text{weak neutral currents}} + \underbrace{gsin\theta_W J_\mu^{e.m.} A_\mu}_{\text{e.m. current}}. \tag{1.24}$$

The lagrangian of the electroweak interactions is the sum of three terms, each one representing the weak charge current, the weak neutral current and the electromagnetic neutral current, respectively. From the last term, we know that the coupling constant must be the electric charged, so $e = gsin\theta_W$.

Chapter 2

Neutrino-Nucleon scattering

2.1 Inclusive cross section

The neutrino-nucleon interactions are described by the following reactions:

$$\nu(\bar{\nu}) + N \rightarrow l^{-}(l^{+}) + X, \tag{2.1}$$

and,

$$\nu(\bar{\nu}) + N \rightarrow \nu(\bar{\nu}) + X, \tag{2.2}$$

where $l^{\pm}$ represents an arbitrary lepton and N and X the initial and final nucleons. These reactions are characterized by producing a lepton or a neutrino in the final states, defined as charged and neutral current interactions respectively. The reactions 2.1 and 2.2 can be represented by a Feynman diagram as figure 2.1 shows.

The differential cross section for neutrino-nucleon scattering is calculated as follows (see appendix B):

$$\frac{d\sigma}{dQ^2} = \frac{1}{64\pi^2 m_N^2 E_\nu^2}|\mathcal{M}|^2, \tag{2.3}$$

where Q^2 is de momentum transfer defined as

$$Q^2 = 2E_\nu - 2|k||k'|cos\theta - m_l, \tag{2.4}$$

where m_N is the nucleon mass, E_ν the incident neutrino energy and $|\mathcal{M}|$ is called the invariant amplitude. Then, for a given incident neutrino energy (E_ν), the total cross section is just the integral over the Q^2,

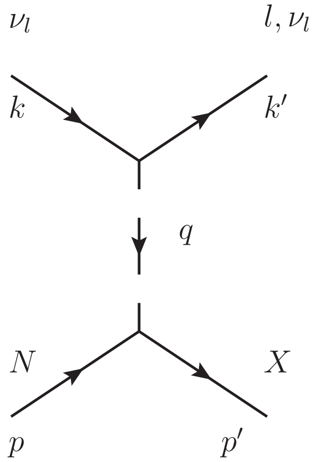

Figure 2.1: Feynman diagram of a neutrino-nucleon interaction. The (k,p) and (k',p') represents the initial and final momenta of the particles and q corresponds to the momentum transfer.

$$\sigma(E_\nu) = \int_{Q^2_{min}}^{Q^2_{max}} \sigma dQ^2, \tag{2.5}$$

where Q^2 runs in the range of

$$\begin{aligned} Q^2_{min} &= -m_l + 2E_\nu(E_l - |k'|) & (2.6)\\ Q^2_{max} &= -m_l + 2E_\nu(E_l + |k'|), & (2.7) \end{aligned}$$

being E_l the lepton energy. At this point, the invariant amplitude is the only unspecified factor to determine the cross section. Such a quantity can be evaluated using the Feynman rules[22] for the quantum field theory. According to these rules, the invariant amplitude can be expressed as the product of interaction fields, the coupling vertexes and the propagator (see figure 2.2).

The fermionic fields $(\nu, l^\pm)$ are represented by Dirac spinors $(\bar{u}_l, u_\nu)$. The hadronic current is, at the moment, denoted by the following expression:

$$< X(p')|J_\beta|N(p) > . \tag{2.8}$$

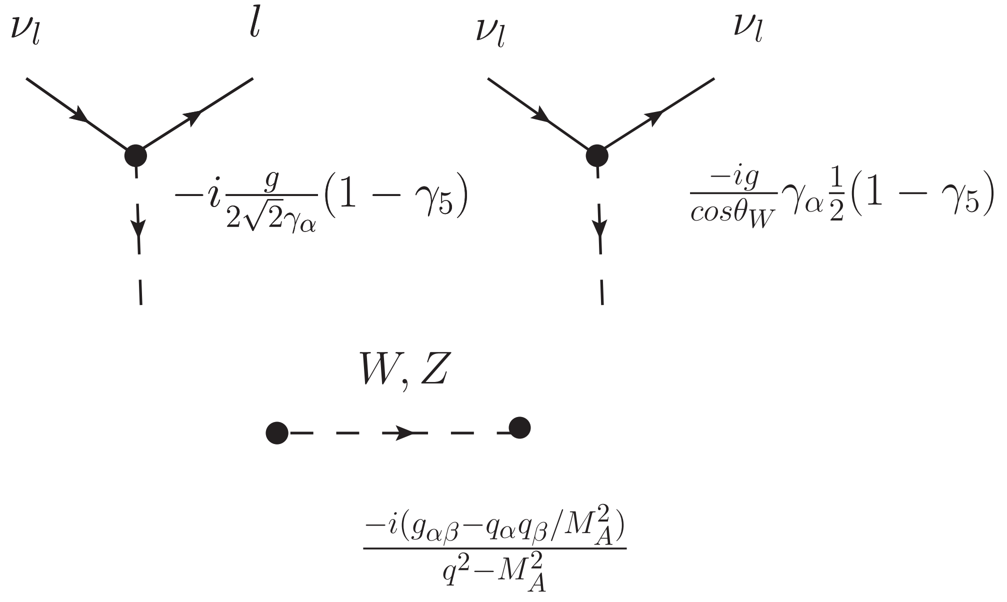

Figure 2.2: Feynman rules for the weak interactions. Top diagrams represent, reading from left to right, the coupling vertexes for the charged and neutral interactions. The botton diagram corresponds to the virtual propagator (with A representing the $W^{\pm}, Z^0$

With all these ingredients, the invariant amplitude for a charged current weak interaction results of the form:

$$\mathcal{M} = (\frac{g}{2\sqrt{2}})^2 \bar{u_l}(k')\gamma_\alpha(1-\gamma_5)u_\nu(k)\frac{-i(g^{\alpha\beta}-q^\alpha q^\beta/M_W^2)}{q^2-M_W^2} < X(p')|J_\beta|N(p) > . \tag{2.9}$$

In analogous way, the neutral weak interactions can be extracted (using the neutral coupling term and changing $M_W \rightarrow M_Z$ in the propagator expression). For simplicity, only the equation (2.9) is developed here.

The equation 2.9 can be simplified if a low momentum transfer ($|q^2| << M_W^2$) is assumed. In this case, the propagator takes the form:

$$\frac{-i(g^{\alpha\beta}-q^\alpha q^\beta/M_W^w)}{q^2-M_W^2} \rightarrow \frac{-ig^{\alpha\beta}}{M_W^2}, \tag{2.10}$$

obtaining

$$\mathcal{M} = -i\frac{g^2}{8M_W^2}\bar{u_l}(k')\gamma_\alpha(1-\gamma_5)u_\nu(k) < X(p')|J^\alpha|(p) > . \tag{2.11}$$

The square of the invariant amplitude (2.11) can be expressed, in a contracted form, in terms of leptonic ($L_{\alpha\beta}$) and hadronic ($W_{\alpha\beta}$) tensors. The expression is written as follows:

$$|\mathcal{M}|^2 = \frac{G_F^2}{2} L_{\alpha\beta} W^{\alpha\beta}, \tag{2.12}$$

where the Fermi constant (G_F) has been defined as

$$\frac{G_F}{\sqrt{2}} = \frac{g^2}{8M_W^2}. \tag{2.13}$$

The leptonic tensor is calculated of the following way[23]:

$$\begin{aligned}
L_{\alpha\beta} &= \sum_{s_i}\sum_{s_f} [\bar{u}_l(k')\gamma_\alpha(1-\gamma_5)u_\nu(k)]^\dagger[\bar{u}_l(k')\gamma_\beta(1-\gamma_5)u_\nu(k)] && (2.14)\\
&= Tr[(\not{k} + m_l)\gamma_\alpha(1-\gamma_5)(\not{k}' + m_l)\gamma_\beta(1-\gamma_5)] && (2.15)\\
&= 8[k'_\alpha k_\beta + k'_\alpha k'_\beta - g_{\alpha\beta} k\cdot k' + \epsilon_{\alpha\beta\rho\sigma}k^\rho k'^\sigma] && (2.16)\\
&= L^S_{\alpha\beta} + iL^A_{\alpha\beta}, && (2.17)
\end{aligned}$$

where the two sums, at the first expression, include the total number of initial (s_i) and final (s_f) spin states and the superscript S and A, at the last expression, refer to the symmetry under interchange of the Lorentz indices (α,β). For anti-neutrinos the anti-symmetric piece gets a minus sign, so the leptonic tensor is in general written as follows:

$$L_{\alpha\beta} = L^S_{\alpha\beta} \pm iL^A_{\alpha\beta}. \tag{2.18}$$

The hadronic tensor:

$$W^{\alpha\beta} =< X(p')|J_\alpha|(p) >^\dagger < X(p')|J_\beta|(p) > \tag{2.19}$$

must represent the structure of the nucleon, so the final expression is not as simple as the leptonic case. The most general hadronic tensor is given by the expression:

$$\begin{aligned}
W^{\alpha\beta} &= -g^{\alpha\beta}W_1 + \frac{p^\alpha p^\beta}{M^2}W_2 + \frac{i\epsilon^{\alpha\beta\rho\sigma}p^\alpha q^\sigma}{2M^2 W_3} + \frac{q^\alpha q^\beta}{M^2}W_4\\
&+ \frac{p^\alpha q^\beta + q^\alpha p^\beta}{2M^2}W_5 + \frac{i(p^\alpha q^\beta + q^\alpha p^\beta)}{2M^2}W_6 && (2.20)
\end{aligned}$$

where W_i are structure functions. A more detailed development of the hadronic tensor is given in the section 2.3.

2.2 Decomposition of the neutrino cross section

In the previous section, the neutrino interactions have been decomposed in charged and neutral interactions. Hence, the neutrino cross section can be expressed as follows:

$$\sigma = \sigma^{CC} + \sigma^{NC}. \tag{2.21}$$

Each one of these inclusive cross sections can be broken up in basically three processes, the quasi-elastic (σ^{QE}), the resonance (σ^{RES}) and the deep inelastic (σ^{DIS}) cross sections[1]:

$$\sigma^{CC,NC} = \sigma^{QE} + \sigma^{RES} + \sigma^{DIS}. \tag{2.22}$$

1. *Quasi-elastic*

   This channel, main goal of this study, is dominant at energies below 1 GeV as the figure 2.3 shows. The interaction is a two body elastic scattering between the neutrino and the nucleon. The term quasi refers to the fact that the neutrino can change its identity to a charged lepton as well as the neutron can suffer a quark flip becoming a proton.

2. *Resonance production*

   The resonance reaction is characterized by the production of a resonant state due to the excitation of the nucleon during the interaction process. When the excitation is produced by the whole nucleus instead of the nucleon, the specific reaction is called coherent. In both cases, the exited states decay to their fundamental states producing other particles, like kaons and pions.

3. *Deep inelastic*

---

[1] The cross section classification is in someway artificial. There are kinematic regions where the classification is not completely clear

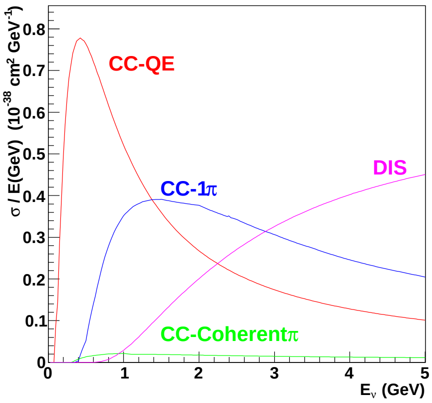

Figure 2.3: Total cross sections as a function of the neutrino energy decomposed in QE, RES and DIS.

This reaction is dominant at high neutrino energies (see 2.3). It is characterized by a high momentum transfer (q), so the nucleon tends to break up and produce new hadrons. The process is called "deep" because the interaction is produced at the quark level. Expressed in other way, the associated wavelength of the propagator ($1/|q|$) is of the size of the nucleon constituents.

2.3 Quasi-elastic charged current cross section

The neutrino charged current quasi-elastic (CCQE) interaction is given by the following reaction:

$$\nu(\overline{\nu}) + n(p) \longrightarrow l^-(l^+) + p(n). \tag{2.23}$$

The derivation of the cross section will be given explicitly for neutrinos although it can be straightforward extended to anti-neutrinos. At the same time, the calculations are not restricted to any particular neutrino flavour.

As it was mentioned in the previous section, the square of the invariant amplitude can be written as follows:

$$|\mathcal{M}|^2 = \frac{G_F^2}{2} L_{\alpha\beta} W^{\alpha\beta}, \tag{2.24}$$

The leptonic tensor was already calculated in (2.17). For the hadronic tensor, just a general expresion was given (2.20). Here, in order to introduce our hadronic vertex, the associated current is defined as follows:

$$J_\alpha^{CC} =< p(p')|J_\alpha^{CC}(0)|n(p) >, \tag{2.25}$$

where p(p') and n(p) denote a proton and a neutron with momentum p and p' respectively. The transformation of a neutron into a proton means, in the valence quark model, the transformation of a down quark into an up quark. Then, a Cabbibo mixing angle must be included ($cos\theta_C$). Following Lorentz invariant arguments, as used in lepton tensor, the hadronic charged current is written as follows:

$$J_\alpha^{CC} = cos\theta_C (V_\alpha^{CC} - A_\alpha^{CC}), \tag{2.26}$$

where V_α^{CC} and A_α^{CC} correspond to the vector and the axial parts. Since each part must be a Lorentz four-vector, one can construct the most general form of the vector and axial parts by using the four-momentum vectors (p,p'and q) and the Dirac γ matrices following the arguments from Ref. [24]. Hence, the vector part can be expressed as follows [25]:

$$V_\alpha = \gamma_\alpha F_1^V(Q^2) + \frac{i}{2M}\sigma_{\alpha\beta}q^\beta F_2^V(Q^2) + \frac{iq_\alpha}{2M}F^S(Q^2), \tag{2.27}$$

where $Q^2 = -q^2$, $\sigma_{\alpha\beta}$ represents the Pauli matrix and M is the nucleon mass. $F_{1,2}^V$ and F^S are vector and scalar form factors. The same procedure is given for the axial part:

$$V_\alpha = \gamma_\alpha F_A(Q^2) + \frac{i}{2M}\sigma_{\alpha\beta}q^\beta F_T(Q^2) + \frac{iq_\alpha}{2M}F_P(Q^2), \tag{2.28}$$

where F_A, F_T and F_P are the axial the tensor and the pseudo-scalar form factors respectively. In general, the form factors are functions that contains information of the structure of the nucleon and traditionally adopt a dipole form (see appendix C).

The hadronic current can be simplified just by assuming two symmetries. On one hand, the time reversal invariance that vanishes the imaginary part of the form factors. On the other hand, the charge symmetry that, together with the time invariance, cancels the F^S and F^T form factors (see ref. [26],[27]). With those symmetries, the hadronic current is written as follows:

$$J^{CC}_\alpha = cos\theta_C u_p(p')[\gamma_\alpha F^V_1 + + \frac{i\sigma_{\alpha\beta}q^\beta F^V_2}{2M} + +\gamma_\alpha\gamma_5 F^A + \frac{q_\alpha\gamma_5 F^P}{2M}]u_n(p). \quad (2.29)$$

At this point, the cross section can be expressed in a contracted way by using a parameterization model described by the Llewellyn-Smith formalism[28]. This formalism allows to describe the cross section in terms of functions that only depend on the momentum transfer (Q). The neutrino cross section is then written as follows:

$$\frac{d\sigma^{\nu\overline{\nu}}}{dQ^2} = \frac{M^2 G_F^2 cos^2\theta_C}{8\pi E_\nu^2}\left[A(Q) \pm \frac{s-u}{M^2}B(Q) + \frac{(s-u)^2}{M^4}C(Q)\right]. \quad (2.30)$$

where $s - u = 4ME_\nu - Q^2 - m_l^2$. Here, neutrino and anti-neutrino cross section just differ by the sign in the B term (minus for anti-neutrinos). The A, B and C functions are defined as follows:

$$\begin{aligned} A &= \left(\frac{m_l^2 + Q^2}{M^2}\right)[(1+\tau)F_A^2 \\ &\quad -(1-\tau)(F_1^V)^2 + \tau(1+\tau)(F_2^V)^2 + 4\tau F_1^V F_2^V \\ &\quad -\frac{m_l}{4M^2}\left((F_1^V + F_2^V)^2 + (F_A + F_P)^2 - (\frac{Q^2}{M^2} + 4)F_P^2\right)] \end{aligned} \quad (2.31)$$

$$B = \frac{Q^2}{M^2}F_A(F_1^V + F_2^V), \quad (2.32)$$

$$C = \frac{1}{4}(F_A^2 + (F_1^V)^2 + \tau(F_1^V)^2), \quad (2.33)$$

where $\tau = Q^2/4M^2$. Note that F_P is multiplied by m_l^2/M^2, so that contribution is negligible for ν_e and ν_μ but not for ν_τ flavour.

Summarizing, the cross section can be expressed in terms of four form factors, F_1^V,F_2^V,F_A and F_P. The vector form factors $F_{1,2}^V$ can be expressed, assuming conserved vector current (CVC)[29], in terms of the Dirac and Pauli electromagnetic form factors ($F_1^{p,n}$ and $F_2^{p,n}$), in the following way:

$$F_{1,2}^{V}(q^2) = \frac{F_{1,2}^{p}(q^2) - F_1^{n}(q^2)}{2}. \tag{2.34}$$

The Dirac and Pauli electromagnetic form factors have been measured in electron scattering experiments. The electromagnetic form factors can be written, using the Galster et all formalism[30], in the following way:

$$F_1^N = \frac{G_E^N + \tau G_M^N}{1+\tau} \tag{2.35}$$

$$F_2^N = \frac{G_M^N - G_E^N}{1+\tau}, \tag{2.36}$$

where $\tau = -q^2/4M^2$. The G_E and G_M are called the Sachs form factors [31],[32] and are parameterized in the way:

$$G^p = \frac{G^p}{\mu_p} = \frac{G^n}{\mu_n} = -(1+\lambda_n\tau)\frac{G_E^n}{\mu_n\tau} = \left(1 - \frac{q^2}{4M_D^2}\right) \tag{2.37}$$

where λ_n and the dipolar mass M_D are free parameters with values determined experimentally ($\lambda_n = 5.6$ and $M_D = 0.843GeV$).

The pseudo-scalar form factor (F_P) can be related to the axial form factor (F_A) by requiring partially conserved vector current (PCAC), in the following way:

$$F_p(q^2) = F_A(q^2)\frac{2M}{m_\pi^2 - q^2}, \tag{2.38}$$

with m_π and M representing the pion and nucleon masses. The axial form factor commonly adopt the following dipolar form:

$$F_A(q^2) = \frac{g_A}{\left(1 - \frac{q^2}{M_A^2}\right)^2}, \tag{2.39}$$

where parameters g_A and the axial mass M_A are obtained through experimental data fits. So, the best current value for g_A, extracted from beta decay experiments, is -1.267[33]. The axial mass can only be determined by neutrino experiments. The world average value is 1.026[27], although the most current experiments have reported higher values [34], [35] and [36].

2.4 Nuclear Effects

In last sections, the neutrino-nucleon scattering has been described under the assumption that nucleons behave as free particles. However, nucleons are bound to the nuclei and two important effects must be considered, the Fermi motion, the Pauli blocking, derived both from the Fermi gas model. Moreover, re-scattering and absorption inside the nuclei takes importance as well.

2.4.1 Fermi Gas Model

There are different models attempting to describe the nuclear structure, although no single model is detailed enough to encompass all the aspects of the nucleus. The most simplistic model considers the nucleus an ideal gas composed of weakly interacting fermions, protons and neutrons. This model description is known as the Fermi gas model. The system obey Fermi-Dirac statistics, leading to the Pauli exclusion principle. Fermions are confined within nuclear potencial wells (see sketch 2.4).

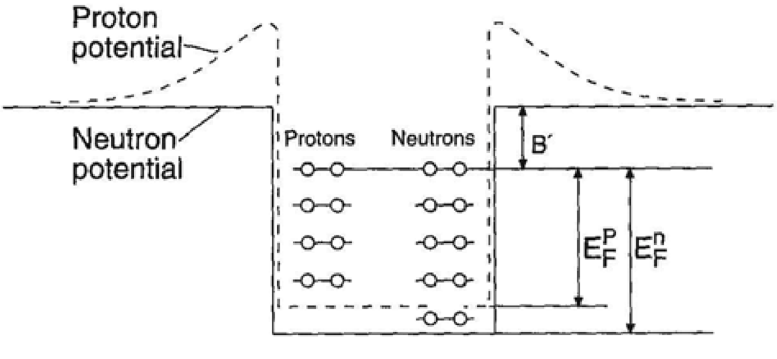

Figure 2.4: Sketch of the proton and neutron potential wells and states in the Fermi gas model[37]. E_F^p and E_F^n represent the Fermi energy of the proton and neutron, respectively. B' corresponds with the binding energy. See text for details.

The number of states of protons (or neutrons) within the nuclear volume V is given by:

$$dn = \frac{4\pi V dp}{(2\pi\hbar)^3} V. \tag{2.40}$$

For the nucleus in its ground state, the lowest states will be filled up to a maximum momentum, called the Fermi momentum (p_F). The total number of states follow from integrating from 0 to p_F:

$$n = \frac{V p_F^3}{6\pi\hbar^3}, \tag{2.41}$$

where here the two posible nucleon states (spin) have been considered.

In the electron scattering, the nuclear radius is $R = r_0 A$ (with r_0= 1.21 fm) and N = Z = A/2. In this case, the Fermi momentun, derived from equation (2.41), results of 250 MeV/c. The Fermi energy (E_F), defined as the energy of the highest occupied nucleon level, is then $E_F = p_F^2/2m_N \approx 33MeV$. The difference between the edge of the potencial well and the Fermi level is defined as the binding energy B' (see sketch 2.4).

In the Fermi gas nuclear model, a neutrino-nucleon interaction only can occur if the nucleon involved recieves enough momentum (above the Fermi momentum) because all the states are already occupied. This suppresion is called Pauli blocking and is specially present at low momentum transfer, because the momentum transfer is comparable to the Fermi momentum (for $Q^2 < 0.2\ GeV^2$).

The Fermi gas model provides a reasonable qualitative description of the continuum nuclear response, but is indeed limited. The effects of dynamical nucleon-nucleon correlations in the initial an final states, that play a critical role in specific kinematical regions, are not included. Nowdays, several efforts are underway to incorporate better models beyond the Fermi gas model[38, 39, 40].

2.4.2 Absorption and rescattering processes

The intra-nuclear innteractions of the mesons and nucleons, produced in neutrino interactions, are also important nuclear effects to take into account. Pion absorption interactions are events in which pion is not observed in the final states. A re-scattering of protons can modify the momentum of the particle. All these kinematics changes can modify the event type classification performed in the analysis.

Chapter 3

The SciBooNE experiment

This chapter introduces the SciBooNE experiment, explaining the main physicis purposes. A description of the experimental setup is reported.

3.1 Introduction

The SciBar Booster Neutrino Experiment (SciBooNE)[41] is a neutrino and anti-neutrino scattering experiment located at the Fermi National Accelerator Laboratory (FNAL) in Chicago (USA). The main goal is to measure the neutrino and anti-neutrino cross sections at neutrino energies around 1 GeV.

The SciBooNE experiment is composed of three detectors: a fully active fine grained Scintillator Bar detector (SciBar), an Electromagnetic Calorimeter (EC) and a Muon Range Detector (MRD).

The SciBooNE experiment takes advantage of the Booster Neutrino Beam line (BNB) which has been used in the MiniBooNE experiment[36]. So, the SciBooNE detectors are placed at 100 meters downstream of the target and 440 meters upstream of the MiniBooNE detector.

3.2 History of SciBooNE

The idea of the experiment came up in early 2005, right after the completion of the K2K experiment. The SciBooNE collaboration was formed in summer 2005. In

2006, the SciBar and EC detectors, placed at KEK in Japan, were disassembled and moved to FNAL. We participated during the summer of 2006 in the construction, piece by piece, of the MRD detector. In April 2007, all the detectors were installed in the detector hall. Finally, in June 2007, after the commissioning, the experiment started to take data (see table 3.1 for a detailed cronology of the experiment).

2005 Summer	Collaboration was formed.
2005 Dec.	Proposal was approved by FNAL PAC (FNAL E954).
2005 Nov. - 2006 Feb.	The SciBar/EC detectors were disassembled at KEK.
2006 Jul.	The SciBar/EC components were moved to FNAL.
2006 Sep.	Civil construction of the detector hall was started.
2006 Nov. - 2007 Mar.	Sub-detectors were built up and tested with cosmic-rays.
2007 Apr.	Detector was installed into the detector hall.
2007 May.	Sub-detector systems were merged and commissioned.
2007 Jun. - 2007 Aug.	Data-taking with antineutrino beam (Run-I).
2007 Oct. - 2008 Apr.	Data-taking with neutrino beam (Run-II).
2008 Apr. - 2008 Aug.	Data-taking with antineutrino beam (Run-III).
2008 Aug.	SciBooNE completed data-taking.

Table 3.1: Cronology of the SciBooNE experiment.

3.3 Physics motivations

The main SciBooNE goal is to measure the neutrino/antineutrino-nucleus cross section in Carbon around 1 GeV. Three physical motivations support such measurments: (1) to contribute with high and precise cross section measurements at low energies, where existing old data are rather sparse and with low statistic,(2) to provide additional cross section measurements to neutrino oscillation experiments and (3) to measure the neutrino/anti-neutrino flux from booster neutrino beam, helpful to constraint flux predictions used in MiniBooNE oscillation analysis.

3.3.1 Precisse neutrino cross section measurements

The first neutrino cross sections measurements around 1 GeV were made in the decades of 70's and 80's. In many cases, the detection technique was based on bubble chambers ([42, 43]). This technique, although precisse, was limited by low statistics and large flux uncertainties. Figure 3.1 shows a collection of the world's charged current (CC) neutrino cross section data as a function of energy. Note the low data population below 1 GeV neutrino energy. In addition, table 3.2 shows a comparison of detection techniques and statistics for several neutrino experiments.

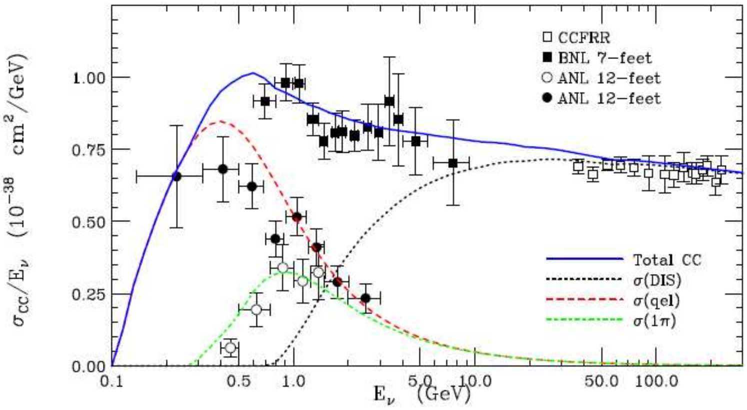

Figure 3.1: Charged current cross section data for several past experiments as a function of the neutrino energy. Predictions come from NUANCE MC (plot extracted from [44]).

Experiment	end-run	$< E_\nu >$	ν-target	detection type	ν-interactions
ANL	1973	1.6	deuterium	Bubble chamber	$\sim 10^3$
GGM	1973	2.2	propane	Bubble chamber	$\sim 10^3$
BNL-7ft	1981	1.6	deuterium	Bubble chamber	$\sim 10^3$
MiniBooNE	not finished	0.8	carbon	Cherenkov	$\sim 10^6$
K2K-SciBar	2004	1.2	carbon	segmented tracker	$\sim 10^4$
SciBooNE	2008	0.8	carbon	segmented tracker	$\sim 10^5$

Table 3.2: Comparison of various attributes between the old (ANL, GGM and BNL) and recent neutrino experiments (K2K, SciBooNE and MiniBooNE).

In the last years, the neutrino detection techniques have been mainly dedicated to Cherenkov light and scintillator traking detectors, allowing a high data collection. At the same time, the neutrino flux prediction has been improved with results from hadron production experiments. Such experiments, like HARP[45], have measured the hadron production cross sections with different targets and different neutrino energies. Therefore, high statistic and accurate neutrino flux prediction have improved the quality of the cross section data at low energies reported by recent neutrino experiments. This is the case of the SciBooNE experiment that, together with past (K2K[46]), present (MiniBooNE[36],Minos[47], T2K[48]) and near future (Minerva[49]) experiments will contribute to populate the cross section data at low neutrino energies, helping to fill the gap in the understanding of neutrino interactions at few GeV.

3.3.2 Neutrino oscillation experiments

The goal of next-generation long baseline accelerator-based neutrino oscillation experiments is to measure a non-zero θ_{13} via ν_e appearance as well as improve the precission in oscillation parameters related to ν_μ disappearance. Currently, two experiments are planned, the Tokai-to-Kamioka (T2K) experiment[48] and the NuMI Off-axis ν_e Appearance (NOvA) experiment[50]. The oscillation parameters are obtained from the measurement of the initial and final neutrino flux, using the CCQE interaction channel for such a purpose. In this task, the main contamination comes from the CC1π and CCπ^0 (for ν_e disappearance measurements) interaction channels. So, good extraction of the oscillation parameters relies on precise measurements of neutrino cross section [51]. In such a context, the SciBooNE data will provide helpful information, specially to T2K experiment since the neutrino energy spectra are similars as figure 3.2 shows.

3.3.3 Flux measurements

The MiniBooNE and SciBooNE experiments shares the neutrino beam line. For such a reason, SciBooNE flux measurements can provide additional constraints to the MiniBooNE flux predictions, acting like ”near detector” for MiniBooNE. The anti-neutrino mode is specially relevant. In this case, a large fraction of neutrino contamination is expected, around 30%[41] of the total anti-neutrino mode event rate. Unlike the MiniBooNE, the SciBar detector technique can distinguish neutrino versus antineutrino charged current quasi elastic (CC-QE) interactions on an event-by-event basis. This is based on the different event topology for neutrinos and anti-neutrinos: CC-QE neutrino interactions are expected to have two tracks

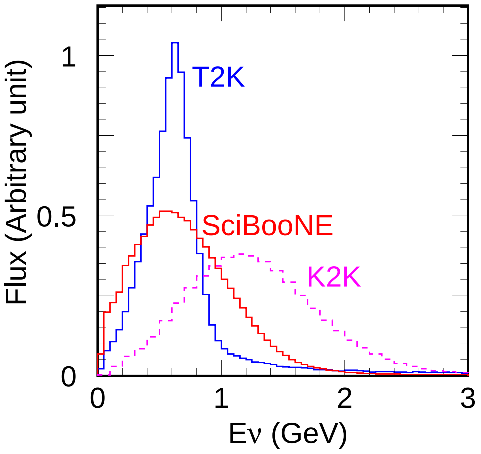

Figure 3.2: Comparison of the muon neutrino energy spectra at K2K, T2K and SciBooNE. All curves are normalized to unit area[41].

(one each from the muon and proton) while antineutrino interactions are expected to have only one track (from the muon), since the neutron is not detected. So by selecting 1-track sample in anti-neutrino mode, SciBooNE produces a data sample with 80% of right sign events, although by taking the 2-track m+p sample, a 70% wrong-sign events is obtained (see fig. 3.3).

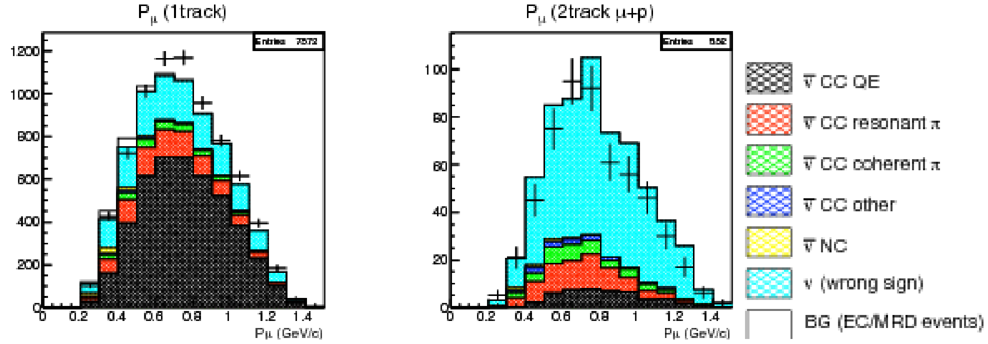

Figure 3.3: SciBooNE muon momentum distributions for the 1-track (left plot) and 2-track (right plot) samples corresponding to anti-neutrino running mode. The fill histograms represent the Monte Carlo, broken up in neutrino channels (colours). Dots represents the data.

3.4 Experimental setup

The SciBooNE detectors are installed in a 7 meters deep hall, located at 100 meters downstream from the target. The SciBooNE emplacement is on the axis of the Booster Neutrino Beam (BNB) direction, which points to the MiniBooNE detector, located at 540 meters downstream of the target (see figure 3.4).

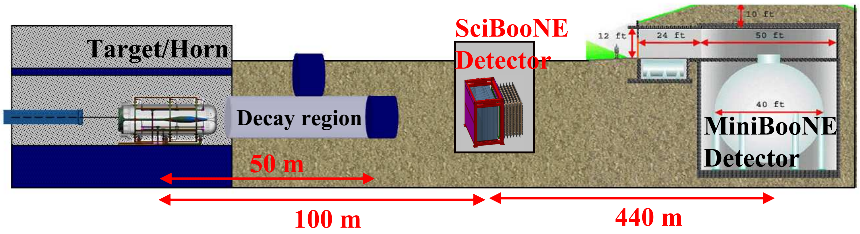

Figure 3.4: Schematic drawing of the experimental SciBooNE setup.

3.4.1 The Booster Neutrino beam line

The Booster accelerator produces the primary proton beam, accelerated up to 8 GeV. Selected batches containing approximately 4-5$\times 10^{12}$ protons are extracted and bent toward the target hall via dipole magnets. The spill duration is of 1.6 μs. Each spill is composed of 81 bunches of protons of 6 ns wide each and 19 ns apart.

The primary proton beam strikes a thick beryllium target made of seven cylindrical slugs with a radius of 0.51 cm and 71 cm long. The target is installed within the magnetic focusing horn, a high-current-carring device. The horn selects the secondary particles that emerge from the proton hadronic interactions, focusing them towards the SciBooNE detector direction (see fig. 3.5). The focusing is produced by the toroidal magnetic field present in the air volume between the two coaxial conductors that compose the horn. The horn current, synchronized to each beam spill, is of 175 kA. Given the pulsed nature of the horn current, a residual magnetic field also penetrates the horn inner conductor (skin depth effect). The polarity of the horn current flow can be (and has been) switched, in order to focus negatively-charged mesons, and produce an antineutrino instead of a neutrino beam. The secondary mesons coming out from the target/horn region

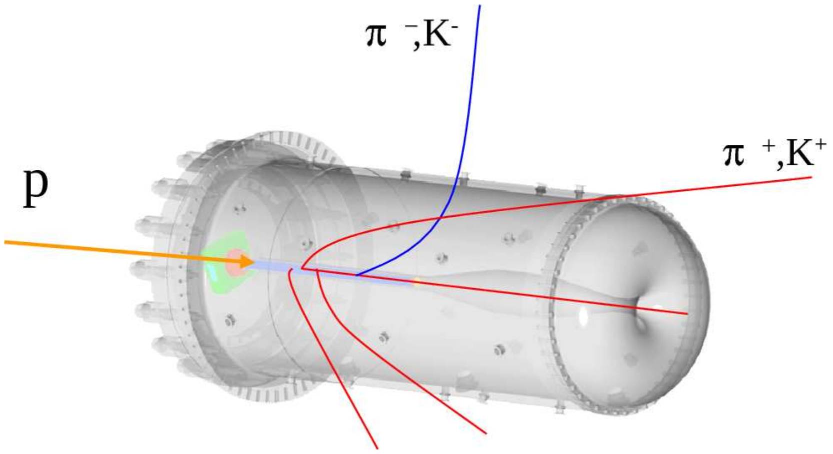

Figure 3.5: Schematic drawing of the magnetic fousing horn in neutrino-mode.

are collimated via passive shielding. The survival mesons, composed mainly of pions, are allowed to decay ($\pi \rightarrow \mu + \nu$) in a cylindrical decay region (see fig. 3.4). This region, 50 meters long and 2 meters in diameter, is just filled with air at atmospheric pressure. A beam absorber, located at the end of the decay region, stops hadronic particles and muons, emerging finally a pure neutrino beam.

Chapter 4

SciBooNE detectors

The SciBooNE experiment is composed of three detectors: the SciBar, the electron catcher and the muon range detectors distributed as the schematic drawing 4.1 shows. The SciBar and the EC detectors are inside of a dark box. The dark box provides a shielding light (specially to the SciBar detector) and a reference for the SciBar-EC alignment. In the following sections, the detector technical details are described.

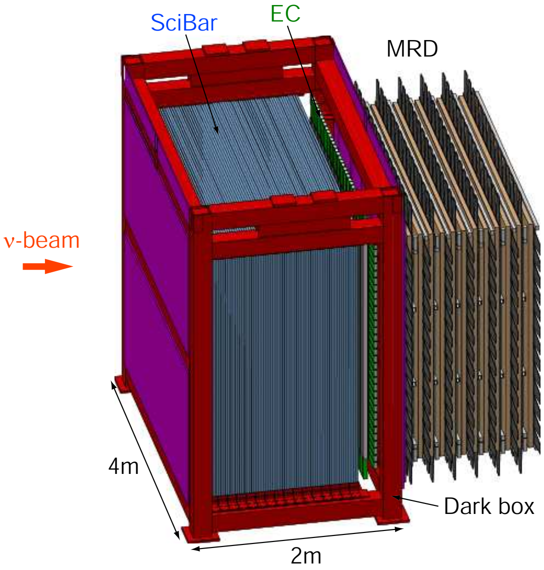

Figure 4.1: Schematic drawing of the SciBooNE detectors.

4.1 The SciBar detector

The SciBar is a finely segmented fully-acitve detector designed originally for the K2K experiment[52]. The detector tracker consists of 14,336 extruded plastic scintillator strips which serves as the target for the neutrino beam as well as the active detection medium. The strips, with dimension of $1.3 \times 2.5 \times 300 cm^3$, are arranged in 64 layers, each one containing an horizontal and a vertical plane. The plane is composed of 116 strips glued together in horizontal or in vertical to define the y or x positions respectively. The total detector volume is of $3 \times 3 \times 1.7 m^3$ with a total mass 15 tons (see fig. 4.2).

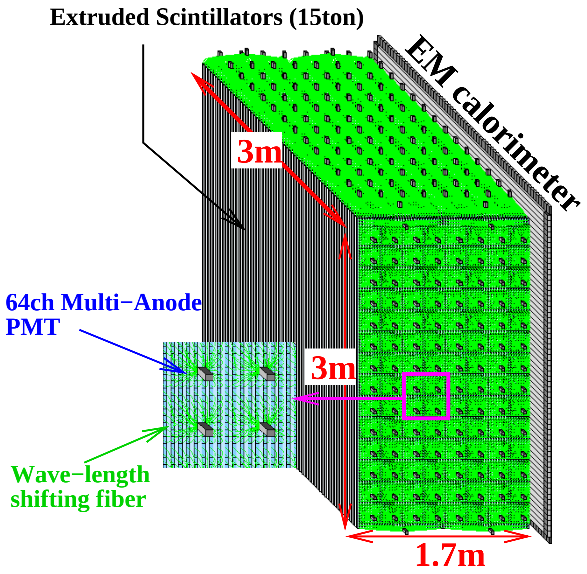

Figure 4.2: Schematic view of the SciBar detector.

The SciBar detector is designed to reconstruct the neutrino-nucleus interactions measuring the final states. The detector segmentation structure allows to reconstruct the trajectory of charged particles in the two projections (x-z) and (y-z). The scintillator strips measures the energy deposited by the charged particles and, combined with the measured length, is able to identify the charged particles. The minimum reconstructed track length is 8 cm (3 layers), which corresponds to 450 MeV/c proton and 100 MeV/c muon energy thresholds.

4.1.1 The scintillator strips

The scintillator strips are made of polystyrene (C_8H_8), infused with the fluors PPO and POPOP (1% and 0.03% respectively). The figure 4.3 shows a schematic drawing of the strip. The strip, with a rectangular cross section of $13 \times 25mm$, is covered with a reflective coating composed of TiO_2 (0.25 mm thickness), which improves the light collection efficiency. In the middle, a hole of 1.8 mm diammeter is used to insert the wavelength shifting fiber (WLS), which collect and transport the scintillating ligth to the photo-detector.

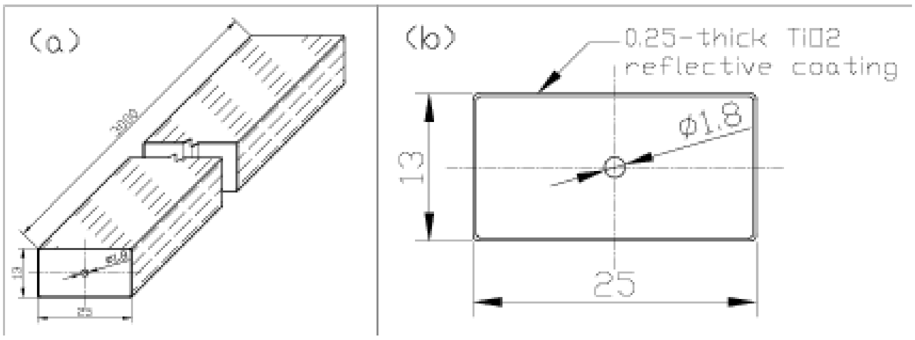

Figure 4.3: Schematic drawing of the scintillator strip. Units are in milimeters.

The light yield from the scintillator is not in general proportional to the energy given by the ionization process. There is a reduction of the light yield at larger energy deposition, the effect is called scintillator quenching. The relation between the visible energy ΔE_{vis} and the actual deposited energy ΔE is expressed by Birk's law[53]:

$$\frac{\Delta E_{vis}}{\Delta E} \propto \frac{1}{1 + c \cdot dE/dx_{exp}}, \tag{4.1}$$

where dE/dx_{exp} is the expected energy deposition per unit legth, and c is Birk's constant which depends on material. The Birk's constant measured for the SciBar scintillator is 0.0208±0.0023 cm/MeV.

4.1.2 Wave length shifting fibers

The green wavelength shifting (WLS) fibers are used to collect the scintillation light for readout. The absorption peak wavelength of the fiber matches with the emission peak wavelength of the scintillator, see fig. 4.4. Each fiber is double-clad

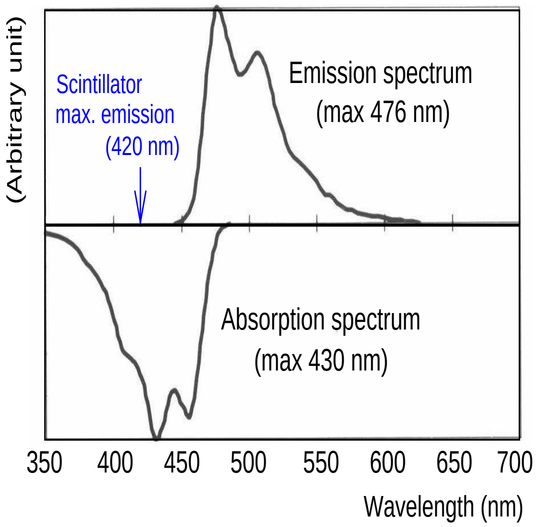

Figure 4.4: Absorption and emission spectra of the Kuraray Y11(200)MS type WLS fiber.

type to capture the maximum light fraction. The fiber core is made of polystyrene (reflective index n=1.56) covered by a thin intermediate acrylic layer (n=1.49) and a thin polyfluor outer clad (n=1.42). The diameter is 1.5 mm and the length is 335 cm for vertical and 360 cm for horizontal fibers. Each sixty four fibers are bundled together and glued to a cookie (see fig. 4.5), which is attached to the multi-anode photo-multiplier.

The attenuation length of the WLS fibers were measured for the K2K installation. The averaged attenuation length resulted of 350 cm. Before the SciBooNE installation, the attenuation length was checked again by sampling a 4% of the total. The results were a 2% shorter than the K2K measurements.

4.1.3 The multi-anode photo-multipliers

The scintillation light is detected by a Hamamatsu H8804 multi-anode photo-multiplier, MA-PMT (see fig. 4.6). Each MA-PMT has 64 channels, whose pixel size is 2 × 2 mm, arranged in an 8 × 8 array. The photo-cathode area is made of bialkali material (Sb,K and Cs). The quantum efficiency is about 12% at

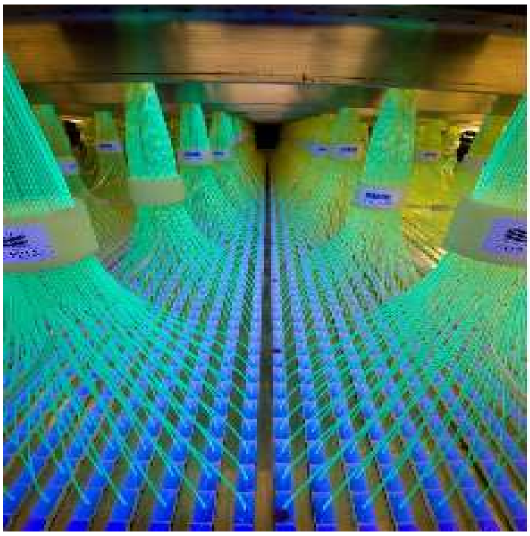

Figure 4.5: Bundles of 64 WLS fibers going out from the scintillator strips in the SciBar detector.

a wavelength of 500 mm. The operation high voltage of each MA-PMT is typically 800 Volts.

The dense packaging of the pixels introduces some adverse features like the cross-talk and the non-uniformity of pixel response. The cross-talk effect is caused by the incident light spreading at the surface of photocathode. This effect has been measured at the laboratory. The amount of measured cross-talk is 3.15±0.4% for an adjacent channel and 0.7% for a diagonal channel. The cross-talk to a next-to-next channel is between 0.1% and 0.3%. The response linearity is kept within 10% up to 200 photoelectrons.

4.1.4 The readout system

The readout system, initally developed for K2K experiment[54], records the charged and timing information from each MA-PMT. The system is composed of a front-end electronics board (FEB) attached directly to the MA-PMT and a back-end VME module (see fig.4.7). Each FEB has two VA/TA chips (VA32HDR11 and TA32CG)[55] employed to multiplex pulse-height information from each anode of the MA-PMT. The back-end VME module, called the DAQ board, controls the readout of the FEBs. The charge information from MA-PMT is digitized with a

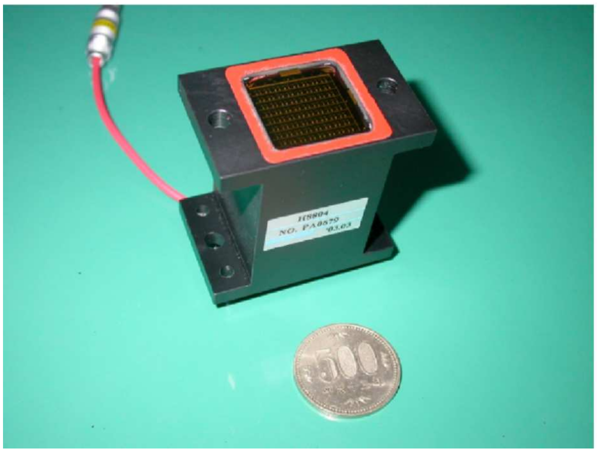

Figure 4.6: A Hamamatsu H8804 multi-anode PMT.

12-bit flash ADC (analog-to-digital converter) and read out through the VME bus. The linearity of the ADC response is kept up to 300 photoelectron. The timing information is processed and recorded by a TDC (time-to-digital converter). The timing resolution and full range are 0.78 ns and 50 μs respectively.

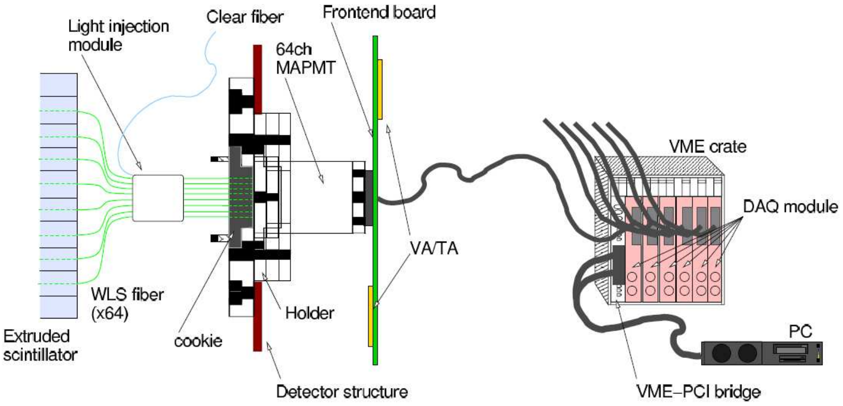

Figure 4.7: Schematic drawing of the SciBar read-out system.

4.1.5 Gain monitor system

The gain of the MA-PMTs is sensitive to small changes like temperature differences and high voltage variations. For such a reason, a gain monitoring system has been used to control the stability gain during the data-taking. The system consist of light sources, PIN phot-diodes and clear fiber bundles. Figure 4.8 shows a schematic drawing of the SciBar monitoring system.

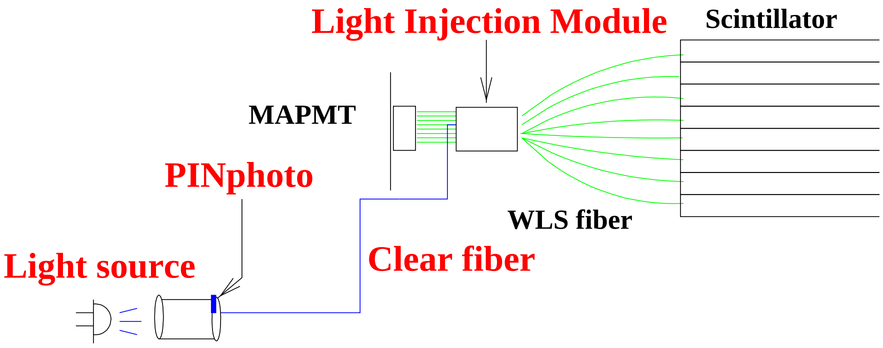

Figure 4.8: Schematic drawing of the SciBar gain monitoring system.

A blue LED, used as the light source, pluses light. The clear fibers transports the pluse light through the light injection module that, assembled to the WLS fiber bundle. distributes the light to each fiber bundle. The MA-PMT signal obtained from that process is compared with the signal coming up from illuminating 2 inch MA-PMT directly or a pin photo-diode. The resultant relative gain for the whole data-taking period was stable within ±2%.

4.1.6 Energy scale calibration

The energy of each scintillator strip is calibrated with cosmic-ray muons. Figure 4.9 shows the number of photo-electrons for cosmic-ray muons in a typical channel (left hand plot). The averaged light yield for a minimum ionizing particle is around 20 p.e./1.3 cm. The energy calibration constant, that converts photoeletrons to visible energy, is measured for each channel. The right plot of figure 4.9 shows the energy calibration constants for all channels, with an averaged value of 8.1 p.e./MeV and channel-by-channel variation about 20%.

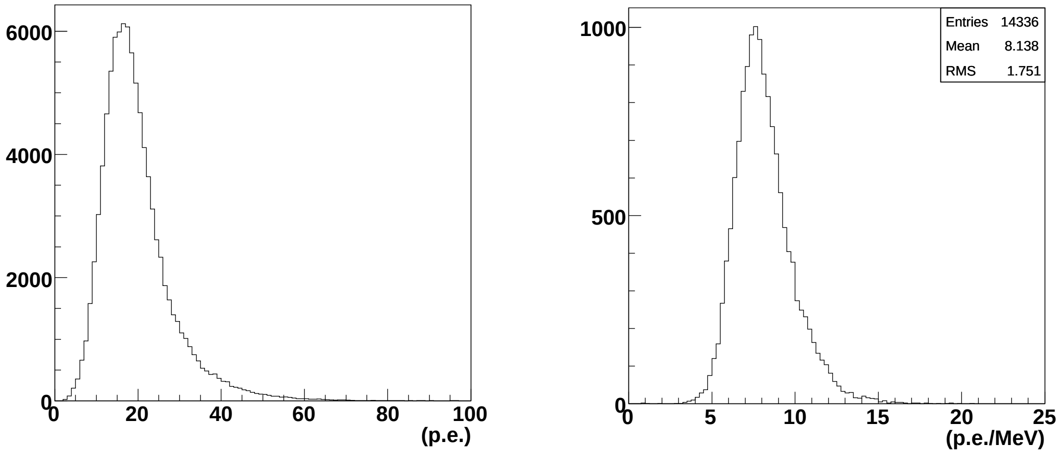

Figure 4.9: Right hand plot represents the number of photo-electrons (p.e) for a cosmic-ray muon in a typical scintillator channel. Left hand plot shows the energy calibration constants for all the channels.

4.2 The Electromagnetic Calorimeter

The electromagnetic calorimeter (EC)[56] was installed downstream of the SciBar detector. The EC was originally built for the CHORUS experiment[57], but it was used in HARP[45] as well as in the K2K experiment. The main purpose of the EC detector is longitudinal containment of the electromagnetic showers that scape from the SciBar detector.

The "spaghetti" calorimeter is composed by a horizontal and a vertical plane with 32 modules each. The module consists of a stack of 21 lead sheets and 740 scintillating fibers (see fig. 4.10). The 1 mm diameter fibers are positioned within the lead sheet grooves made for that purpose. The planes cover an active area of $2.7 \times 2.6\ m^2$ with a thickness equivalent to 11 radiation lengths ($11X_0$), enough to absorb photons and electrons below 3 GeV with 85% energy containment.

At the end of the each module, the fibers are grouped in two bundles, coupled to a plexiglas light guide. The light guide is attached to the Hamamatsu R1315/SM PMT as shows 4.11. In total, the EC detector uses 256 PMTs. The cathode material is bialkali with an average quantum efficiency of 27% in the wavelength range of 350-450 nm. The operation voltage is of 1600 Volts. The non-linearity of the output signal vs input charge is 2% at 60 mA, corresponding to 600 photoeletrons, at a gain 2×10^6. The energy resolution for electrons measured

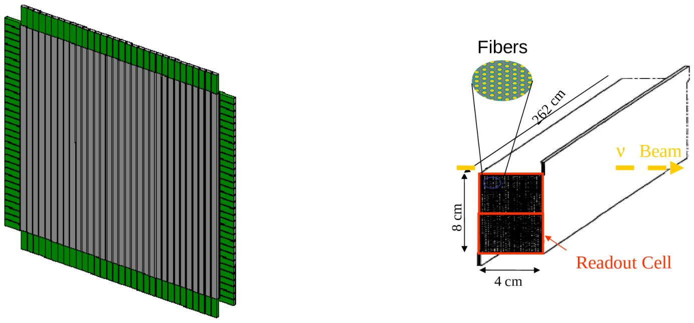

Figure 4.10: Schematic drawing of a EC horizontal plane (left) and a trasversal section of a EC module.

in a test beam resulted $14\%\sqrt(E)GeV^{1/2}$[57].

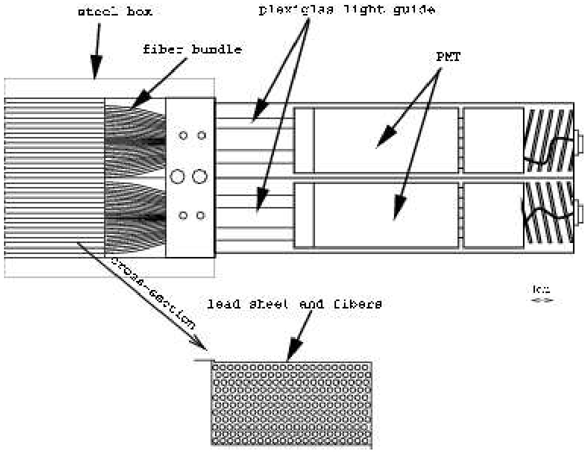

Figure 4.11: Schematic drawing of a EC module coupled to the PMT.

4.3 Muon Range detector

The MRD detector is installed donwstream of the EC. The main goal of this detector is to measure the momentum of the muons produced in charged current interactions. The typical muon momentum range measured by the MRD is from 0.2 to 1.2 GeV/c. Below this range, the muons produced at SciBar do not reach the MRD and above, the muons do not stop inside of the MRD.

The MRD detector, designed exclusively for the SciBooNE experiment, was constructed at the FNAL laboratories. The detector materials comes from recycled parts of past experiments[1]. The MRD consists of 12 iron plates and 13 alternating horizontal and vertical scintillator planes. Each iron plate is 5 cm thick, covering an area of 274×305 cm^2. The total mass of absorber material is around 48 tons. The density of a spare iron plate, measured at several positions, i 7.841 ± 0.002 g/cm^3. The iron plates are sandwiched with alternating horizontal and vertical scintillator planes. The scintillator plane is made of scintillator paddles 20 cm wide and 6 mm thick. The vertical scintillator plane is composed of 30 scintillator paddles 138 cm long, arranged in a 2×15 array to get an active area of 276×300 cm^2. The horizontal scintillator plane contains 26 modules 155 cm long, arranged in a 13×2 array to cover an area 260×310 cm^2. In total, 362 scintillator paddles were used in the MRD (see fig. 4.12).

A total of five types of PMTs has been used for the scintillator paddles readout. The vertical planes uses Hamamatsu 2154-05 PMTs and RCA 6342A PMTs from the NuTeV experiment. The horizontal planes takes EMI 9954KB PMTs from KTeV experiment and EMI 9839b and 9939b PMTs too[58].

The data adquisition system consists of CAMAC electronics supplied by Fermilab's electronic support group. The readout systems, recording timing and charge information, correspond to LeCroy 4300B ADCs and 3377 TDCs. The timing resolution and full range are 0.5 ns and 32 μs, respectively.

The MRD detector has a cosmic-ray trigger independent from SciBar and EC. The hit finding efficiency was continuously monitored using cosmic-ray data taken between beam spills. Figure 4.13 show the hit finding efficiency as a function of position for a typical scintillator plane. The average hit finding efficiency is around 99%.

4.4 Triggering system

There are two types of triggers, the neutrino data-taking (beam) and the detector calibration (off-beam) triggers. The beam-trigger is set by a fast signal sent by the extraction magnet placed at the horn. When the beam time window is open, only neutrino data information is collected into the detectors. This beam trigger

---

[1] For the reclycling effort, SciBooNE was awarded with the DOE 2008 Environment award.

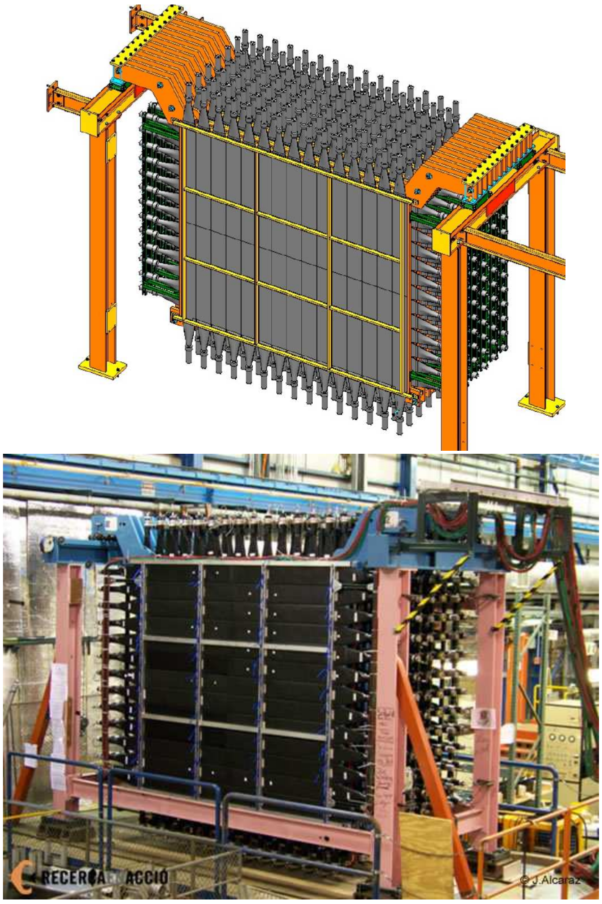

Figure 4.12: Schematic drawing (up) and photo (down) of the MRD detector.

signal has a typical repetition rate of 0.5 Hz, defined by the accelerator operation sequence.

A Global Position System (GPS) records timing triggers. The GPS is connected to a PCI module (a time and frequency processor), where the beam trigger information is recorded. The extraction time of the Booster protons is also recorded in the GPS. Then, at the offline level, detector data and accelerator information can be synchronized.

The off-beam trigger is setup between the spills, when the beam window is closed (see 4.14). There are three types of detector calibration data: the pedestal, the cosmic and the LED (only for SciBar detector). The pedestal and the LED data are triggered once per cycle. A common cosmic trigger is used for SciBar and EC meanwhile the MRD detector has an independent self-generated cosmic-ray

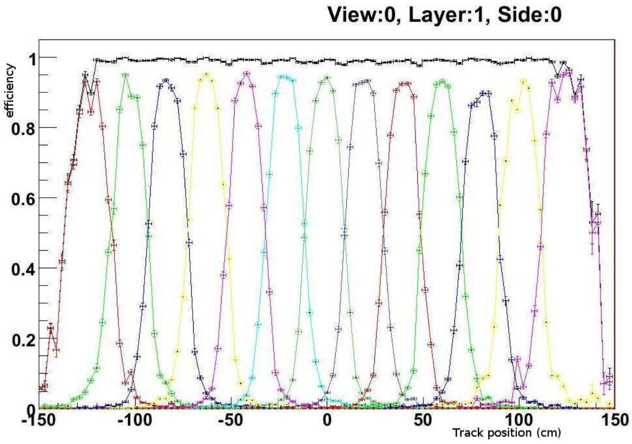

Figure 4.13: Hit finding efficiency as function of track position (coloured). The average hit finding efficiency corresponds to the black points.

trigger. In both cases, the cosmic-ray data is triggered 20 times per cycle.

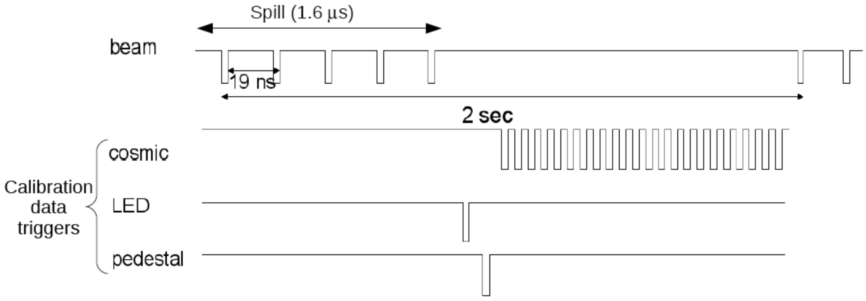

Figure 4.14: Timing structure of the trigger systems.

4.5 Detector coordinates and alignment

The SciBooNE uses a right-handed Cartesian coordinate system, where the z-axis correspond with the beam direction. The y-axis is the vertical upward direction and the x-axis the horizontal direction, perpendicular to the beam direction. The z-coordinate origin is located at the most upstream surface of the SciBar detector. The x and y coordinate origin are in the center of the SciBar detector.

The SciBar and EC detector alignment was performed with respect to the dark box. The SciBar scintillator layer alignment was surveyed during the installation in the dark box. Once the detectors were installed in the detector hall, the SciBar position of each layer was again measured using cosmic-ray muons. A linear fit over the muon-track, but masking a layer every time, is done. Then, the alignment is calculated as the deviation between the theoretical point obtained from the fit and the real position. Figure 4.15 shows the displacement of each scintillator layer with respect to the most upstream one using the two methods (surveying and cosmic-ray).

The relative positions of the EC planes were determined using cosmic-ray muons. The positions of the dark box and the MRD detector were surveyed with respect to the detector hall. In all the cases, the precision on the positions were estimated to be few milimiters.

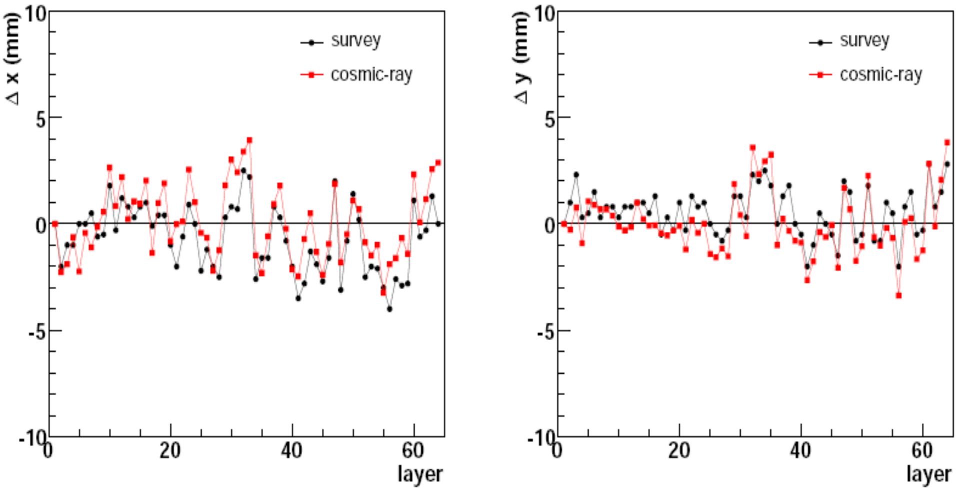

Figure 4.15: Alignment of each scintillator layer with respect to the most upstream layer.

Chapter 5

Monte Carlo Simulation

The SciBooNE Monte Carlo has been designed to simulate the complete experiment. The simulation is composed of three parts: the neutrino beam prediction, the neutrino interactions and the detector response simulations. This chapter describes, in a general way, each simulation process.

5.1 Neutrino Beam simulation

The Monte Carlo code for the neutrino flux predictions has been provided by the MiniBooNE collaboration[59]. The code is based in a GEANT4[60] software. The simulation includes realistic description of materials and geometry presents at the Booster neutrino beam hall and the decay region.

The interactions of primary protons with the beryllium target are simulated according to state-of-the-art hadron interaction data. The production and re-interaction of the resultant secondary particles are simulated using the GEANT4 physics processes. Since neutrinos are produced by π-decays, the π-production takes special relevance.

The prediction of the π-production in p-Be interactions is described by the Sanford-Wang parametrization model[61]. In this model , the double-differential cross section can expressed in terms of nine parameters in the following way:

$$\frac{d^2\sigma}{dpd\omega} = C_1 p^{C_2}\left(1-\frac{p}{p_B - C_9}\right) exp\left(-C_3\frac{p^{C_4}}{p_B^{C_5}} - C_6\theta(p - C_7 p_B cos^{C_8\theta})\right), \quad (5.1)$$

where p is the total meson momentum, θ is the angle of the meson with respect to the incident proton with momentum p_B. The C_i are the parameters determined by the fit using experimental data. The HARP[45] and BNL[42] experiments have provided the experimental inputs.

The K+ production cross-sections are predicted using the Feynman scaling hypothesis. According to this hypothesis, the double-differential cross section can be expressed in terms of seven parameters, determined through of experimental fits. The other hadronic and all the electromagnetic processes are described by the default GEANT4 physic lists.

The GEANT4 output is used as input in a second FORTRAN-based Monte Carlo. This Monte Carlo is responsible of generating the neutrino kinematics distributions from meson and muons decays. The neutrinos are extrapolated along straight lines toward the SciBooNE detector. All neutrinos whose trajectories cross any part of the detector volume are considered for the SciBooNE flux predictions. Each neutrino contains information of its flavour, energy, parent type, incoming direction and kinematics. This information, together with the interaction type and detector simulation, is used to compute a weight for each neutrino event. The weight represents the interaction probability of the event inside of the detector.

The Neutrino flux prediction at the SciBooNE detector, as function of neutrino energy, is shown in figure 5.1. In neutrino mode, the flux is dominated by muon neutrinos (93% of the total) with a small contribution from muon anti-neutrinos (6.4%) and electron neutrino and anti-neutrinos types (0.6%). In anti-neutrino mode, the flux is dominated by muon anti-neutrinos with a 84% of the total, however a strong contribution coming from muon neutrinos (15.6% of the total) is present.

5.2 Neutrino interactions (NEUT)

The neutrino interactions with nuclear targets are simulated with the NEUT program library [62, 63]. This neutrino generator software was originally developed for the Kamiokande experiment[64], running in a neutrino energy range from 100 MeV to 100 TeV. The targets of oxygen, carbon and iron have been used to simulate the neutrino interactions within the different SciBooNE detectors. The nuclear re-interactions of mesons and hadrons produced in the neutrino interactions are

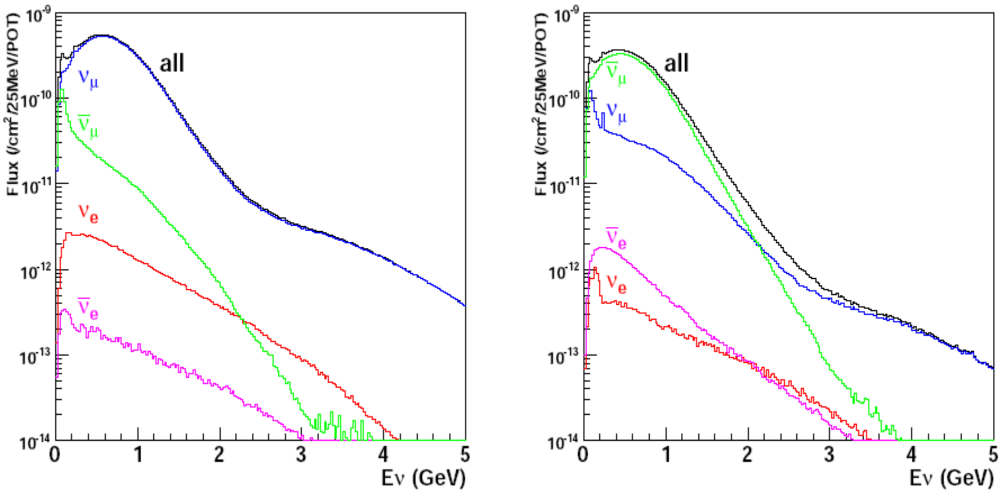

Figure 5.1: The neutrino (left) and anti-neutrino (right) flux predictions, as function of the neutrino energy, at the SciBooNE detector. Flux is normalized per unit area, POT and neutrino energy bin width. The spectra are averaged within 2.12 m from the beam center.

also simulated.

The following neutrino interactions in both charged and neutral current are simulated:

1. Quasi-elastic scattering: $\nu N \rightarrow lN'$
2. Single meson production: $\nu N \rightarrow lN'm$
3. Single gamma production: $\nu N \rightarrow lN'\gamma$
4. Coherent π production: $\nu C(orFe) \rightarrow l\pi C(orFe)$
5. Deep inelastic scattering: $\nu N \rightarrow lN'hadrons$

The table 5.1 shows the expected number of neutrino interactions in the SciBar fiducial volume for each interaction channel.

5.2.1 Quasi-elastic interactions

The quasi-elastic interaction, dominant reaction at the SciBooNE neutrino energies, is implemented using the Llewellyn-Smith parametrization model[28]. A

Channel	ν_μ-interactions
	(/10tons/10^{20}POT)
CCQE	50,800
CC resonant π	26,200
CC coherent π	1,700
CC DIS	6,300
NC elastic	21,400
NC resonant π	10,400
NC coherent π	1,000
NC DIS	2,000

Table 5.1: Expected number of neutrino interactions (ν_μ-mode) in the SciBar fiducial volume.

detail description of this model was exposed in chapter 2.3.

The neutral current elastic scattering can be determined through the CCQE interactions by using the following relations[65, 66]:

$$\sigma(\nu p \to \nu p) = 0.153 \times \sigma(\nu n \to \mu^- p) \tag{5.2}$$

$$\sigma(\overline{\nu} p \to \overline{\nu} p) = 0.218 \times \sigma(\overline{\nu} p \to \mu^+ n) \tag{5.3}$$

$$\sigma(\nu n \to \nu n) = 1.5 \times \sigma(\nu p \to \nu p) \tag{5.4}$$

$$\sigma(\overline{\nu} n \to \nu n) = 1.0 \times \sigma(\overline{\nu} n \to \overline{\nu} n) \tag{5.5}$$

The Fermi gas model of Smith and Moniz[67] is used for scattering off nucleons in the nucleus. In the Fermi gas model, the nucleons are treated like a quasi-free particles, so the Fermi momentum as well as the Pauli exclusion principle is taken into account. The momentum distribution is assumed to be flat up to a fixed Fermi surface momentum set to 217 MeV/c for carbon and 250 MeV/c for iron. The nuclear potential is set to 27 MeV for carbon and 32 MeV for iron. The axial vector mass is set to be 1.11 GeV/c^2.

5.2.2 Resonant single meson production

The resonant pion production is, at the SciBooNE energies, the second dominant channel after the CCQE. The process is described by the Rein and Sehgal model[68]. This model describes the double differential cross section in terms of probability transition amplitude of resonance states ($T(\nu N \rightarrow lN^*)$). Mathematically expressed as follows:

$$\frac{d^2\sigma}{dQ^2 d\mu} = \frac{1}{32\pi m_N E_\nu^2} \cdot \frac{1}{2} \sum_{spins} |T(\nu N \rightarrow lN^*)| \cdot \delta(W^2 - M^2), \tag{5.6}$$

where m_N is the nucleon mass, E_ν the neutrino energy, W the hadronic invariant mass and M the mass of the produced resonance state. The model includes the vector and axial-form factors using dipole parametrization form, with same values than the QE case. The transition probabilities are calculated using the Feynman, Kislinger and Ravndal[69] model.

For finite decay width, the δ-function in the equation (5.6) can be replaced by the Breit-Wigner formula:

$$\delta(W^2 - M^2) \rightarrow \frac{1}{2\pi} \frac{\Gamma}{(W - M)^2 + \Gamma^2/4}. \tag{5.7}$$

All the intermediate baryon resonances with mass less than 2 GeV are included, for greater values, the reaction is simulated as deep inelastic scattering. The corrections for the lepton mass effects[70] are simulated as well.

5.2.3 Coherent pion production

The Rein and Sehgal model[71] simulates the coherent pion production. The differential cross section can be expressed as follows:

$$\frac{d^3\sigma}{dQ^2 dy dt} = \frac{G_F^2 M_N}{2\pi^2} f_\pi^2 A^2 E_\nu (1-y) \frac{1}{16\pi} [\sigma_{tot}^{\pi N}]^2 (1+r^2) \frac{M_{A,coh}^2}{(M_{A,coh}^2 + Q^2)^2} e^{-b|t|} F_{abs}, \tag{5.8}$$

where Q^2 is the square of the 4-momentum transfer of lepton, t is the square of the 4-momentum transferred to the nucleus, m_A is the axial-vector mass, $f_\pi = 0.93 m_\pi$, b = 80 GeV^{-2}, G is the weak coupling constant, M_N is the nucleon mass, $y = E_\nu - E_l / E_\nu$ is the fraction of the lepton's energy loss, E_ν and E_l the neutrino and outgoing lepton energies. A is the atomic number of oxigen and $F_{abs} = e^{-x/\lambda}, \lambda = \sigma_{inel}^{\pi N} \rho$ accounts for the absorption of the pion in the nucleus, expressed as follows:

$$\begin{aligned} F_{abs} &= e^{-x/\lambda}, \qquad (5.9) \\ \lambda &= \sigma^{\pi N}_{inel}\rho \qquad (5.10) \end{aligned}$$

where x is the average path length of the pion in oxygen. $\rho = 4\pi/3R^3$ is the nuclear density with radius R. The $\sigma^{\pi N}_{tot}$ and $\sigma^{\pi N}_{inel}$ are the averaged total and inelastic pion-nucleon cross sections, obtained from experimental results and fitted results given in the Rein and Sehgal's paper[71].

5.2.4 Deep inelastic scattering

The cross section of this interaction is calculated by integrating following equation in the range of W > 1.3 GeV, where W is the invariant mass of the hadronic system:

$$\begin{aligned} \frac{d^2\sigma}{dxdy} &= \frac{G_F^2 M_N E_\nu}{\pi}((1 - y + \frac{1}{2}y^2 + C_1)F_2(x, Q^2) \pm (1 - y + \frac{1}{2}y + C_2)[xF_3(x, Q^2)] \qquad (5.11) \\ C_1 &= \frac{y m_l^2}{4M_N E_\nu x} - \frac{xyM_N}{2E_\nu} - \frac{m_l^2}{4E_\nu^2} - \frac{m_l^2}{2M_N E_\nu x} \qquad (5.12) \\ C_2 &= \frac{m_l^2}{4M_N E_\nu x}, \qquad (5.13) \end{aligned}$$

where $x = -Q^2/(2M_N(E_\nu - E_l))$ and $y = ((E_\nu - E_-))/E_\nu$ are the Bjorken parameters, G_F is the Fermi coupling constant, M_N is the mass of the nucleon, m_l the lepton mass, E_ν and E_l the neutrino and the outgoing lepton energies in the laboratory frame, Q^2 the square of the lepton momentum transfer and $F_{2,3}$ nucleon structure functions.

The multi-pion and in general heavy mesons production are common in deep inelastic interactions. Multiple pion production takes place when the invariant mass W of the νN system is larger than 1.4 GeV/c^2. The number of pions produced in the interactions depends logarithmically on W, estimated from the result of Fermilab 15-foot hydrogen bubble chamber experiment[72]:

$$< n_\pi >= 0.09 + 1.83 lnW^2 \qquad (5.14)$$

5.2.5 Intra-Nuclear interactions

The intra-nuclear interactions of the mesons and nucleons, generated inside of the nucleus by the neutrino interactions, are also simulated. These interactions are treated by using the cascade model, and each of the particles is traced until escapes from the nucleus. The generated position of the pion in nucleus is set according to the Woods-Saxon type nucleon density distribution:

$$\rho(r) - \frac{z}{A}\rho_0 \left[1 + exp\left(\frac{r-c}{a}\right)\right]^{-1}, \tag{5.15}$$

where $\rho_0 = 0.48 m_\pi^3$ and A and Z are mass number and atomic number of the nucleus, respectively. The Fermi motion and Pauli blocking effect are taken into account in the simulation. In the case of the pion, the following intra-nuclear interactions has been considered: inelastic scattering, charge exchange and the absorption.

The re-interactions of the recoil protons are also simulated. This process is especially important because the nucleon-nucleon interactions can modify the outgoing nucleon's momentum and direction. The elastic process and the pion production are considered. The differential cross section used in the simulation were obtained from nucleon-nucleon scattering experiments[73]. For pion production, the data is reported from reference [74].

5.3 Detector simulation

The output information from the NEUT Monte Carlo is used as input for the GEANT4 detector simulation. The final states from neutrino interactions are propagated through the detectors. The simulation includes a detailed geometric model of the detector, including the detector frame, hall and soil.

The detector response is simulated for all the SciBooNE detectors. The attenuation light into the fibers is simulated, taking measured values from cosmic rays. The number of photo-electrons, from PMT signal, is smeared by Poisson statistic and by the PMT resolution, then it is converted in ADC counts. In this process, the electronic noise and threshold effects are included. In the SciBar detector, additional effects like the scintillator quenching and the crosstalk effect are simulated as well. For the MRD detector, gaps between scintillator counters in each plane, which cause inefficiency, are included in the simulation.

Chapter 6

Software Reconstruction

A specific tracking reconstruction software has been used for the SciBar detector. The SciBar algorithm works in two steps. A first step is based on reconstruction of two dimensional (2D) tracks. A Cellular Automaton algorithm has been applied for such a purpose. The second step looks for three dimensional (3D) tracks by using a developed matching criteria. Finally, another matching criteria has been designed to match SciBar track with MRD hits or tracks.

6.1 2D track reconstruction

The 2D track reconstruction algorithm is based on a SciBar Cellular Automaton Tracking[75]. This algorithm was originally used in T2K experiment and has been adapted for SciBooNE. The cellular automaton are dynamical systems which evolve in discrete steps, following certain evolution laws. The cellular automaton system consists of a regular grid of cells in a finite number of states. The states are updated according to the evolution laws.

When a track pass through the SciBar detector, the energy is deposited in the scintillator strips following the trajectory of the track. Each of these scintillator strips are called hits of the track. For track reconstruction, hits are sometimes grouped forming clusters. The cluster represents a collection of adjacent hits in the same plane. That object allows to include all the energy deposited by the particle in the same plane.

The SciBar cellular automaton tracking defines the cell, the neighbours and the evolution rules as follows:

1. **CAT cell**: A straight line connecting two hits or clusters in adjacent layers. To include detector inefficiencies, the segment can skip one layer. For geometrical reasons, if the angle with respect to the z-direction of the segment is larger than 1.1 radians, the clusters must contain more than one hit. Two clusters are connected by a segment if the hit timing different between both are less than 100 ns.

2. **CAT neighbour**: CAT cells sharing a common end point. However, the two CAT cells are connected only if the χ^2, resulting of the least square method for lineal regresion, is less than 4.5. This value allows certaing degree of multiple scattering for the reconstructed track and for detector resolution.

3. **CAT rules**: the CAT cells are initially in the lowest state value, set to one. The evolution algorithm starts at the most upstream region of the CAT cells, where the edge of the segment is not connected to others. Then, the algorithm look for neighbours, increasing the state value of them in one unity. The process is repetead again for each neighbour until no more neighbour are in the same state value.

Picture 6.1 shows an sketch of the cellular automaton tracking in three steps. The CAT cells are represented by arrows and the clusters by circles. Initially, the CAT cells have assigned a state value one, figure 6.1 (A). In a first step, the CAT cell state evolves following the CAT rules, see figure 6.1 (B). The temporal line of the CAT cell evolution follows the z-direction, such that, the state value of a CAT cell at layer Z must be one unity lower than state value of CAT cell at layer Z+1, see figure 6.1 (C).

The collection of track candidates is done by starting from the CAT cell with lowest state value and adding CAT neighbors in order of states values (1-2-3-.....). The procedure runs along CAT cells until all combinations are considered. At this level, tracks with splitting branches are considered. The source of splitting tracks have both physical and instrumental motivations. Detector segmentation design can produce sometimes a splitting track effect, for example, elastic scattering of low energy protons. However, physical processes like the delta ray emission or the muon decays produces splitting tracks as well.

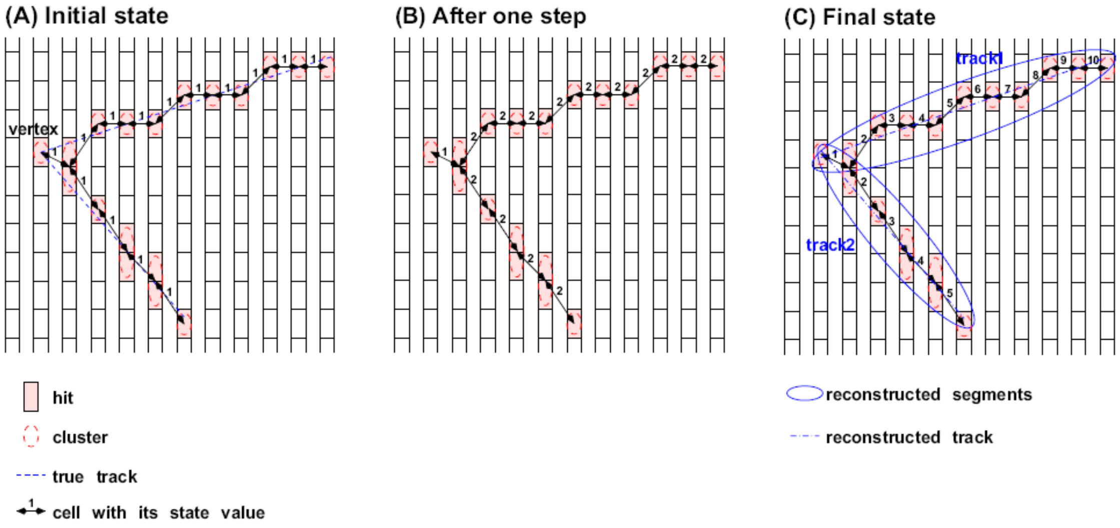

Figure 6.1: Sketch of a cellular automaton tracking process.

6.2 3D track reconstruction

The 2D tracks are just projections in the XZ and YZ views. The 3D reconstructed track is then a matching process of the 2D tracks from the two views. The matching criteria is based on the z-edges and time difference of the 2D tracks. The time is calculated as the average time of the hits associated to the 2D track. The time difference between two 2D tracks must be less than 50 ns. There are three matching cathegories based on the z-edge difference between two 2D tracks. When the z-edges difference is one layer (1.3 cm), the matching is type I. The matching type II and III allows a z-edge difference of three and five planes to take into account vertex activity and cross talk effects. Figure 6.2 shows an sketch with the three types of matching tracks.

When two or more 2D tracks in one view compite to be matched with a 2D track in the other view, the procedure to select the best combination is as follows: the smaller z-edge difference is favored, in case of same z-edge differences, the χ^2 of the energy deposition per unit length between two 2D tracks is calculated. Then, the combination with smallest χ^2 is selected.

The z-edges of the 3D track is defined as the most upstream (downstream) z-edge of the matched 2D tracks. Once z-edges (z_{init} and z_{end}) are defined, the x

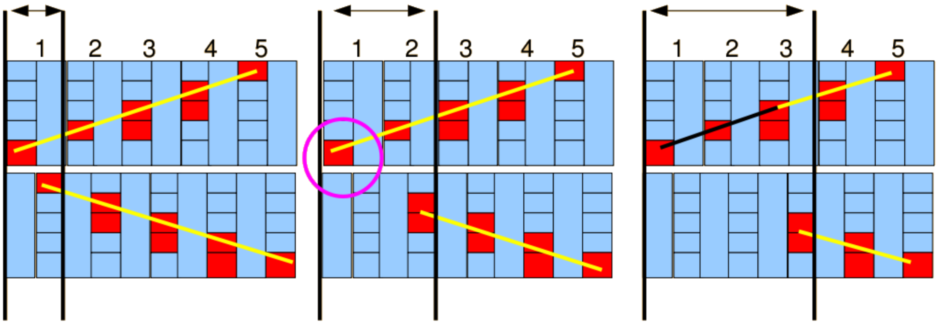

Figure 6.2: Three types of 2D track matching. From left to right, matching type I, II and III.

and y positions are calculated by extrapolating in the following way:

$$x_{init/end} = z_{init/end} \cdot tan\theta_{zx} + x_0 \tag{6.1}$$

$$y_{init/end} = y_{init/end} \cdot tan\theta_{zy} + y_0, \tag{6.2}$$

where θ_{zx} (θ_{zy}) and x_0 (y_0) are the slope and offset of the 2D track in the ZX (ZY) projection, obtained by fitting the 2D track with a straight line.

Once the 3D track is reconstructed, the position of each hit within the fiber is completely defined. At this point, the correction due to light attenuation effect in the WLS fiber is applied. The charge information after correction is evaluated as follows:

$$q' = q \cdot exp\left(\frac{XY - XY_0}{\lambda}\right), \tag{6.3}$$

where λ is the attenuation length of the WLS fiber, XY is the position of the hit within the fiber and XY_0 is the reference position, set to the scintillator edge close to the MA-PMT.

6.3 SciBar-MRD matching track

The 3D reconstructed track at the SciBar detector can be matched with hits or tracks from the MRD detector. The matching process is produced at the 2D level.

That can occur when the most downstream edge of the 2D SciBar reconstructed track is on the last two layers of the SciBar detector. The resultant track is then so-called SciBar-MRD matched track. There are two matching methods: the track-based and the hit-based matching.

6.3.1 Track-based matching

The MRD detector has an independent reconstruction software. The software is based on simple linear fits and is used when the MRD track penetrate at least three steel plates (four scintillator layers), imposing a muon momentum threshold of 350 MeV/c. The track-based matching selects MRD tracks to match with the 2D reconstructed SciBar tracks. The most upstream edge of a MRD track must be in either one of the first two layers of the MRD. The transverse distance between the SciBar and MRD tracks at the first layer of the MRD must be less than 30 cm. The angle difference between SciBar and MRD track, with respect to the beam direction, is given by $|\theta_{MRD} - \theta_{scibar}| < \theta_{max}$, where θ_{max} is a function of the MRD track length, varying between 0.4 and 1.1 radians. The function is calculated as the 3σ boundary of the distribution in each MRD scintillator plane with the MC simulation. The timing difference between SciBar and MRD tracks must be less than 100 ns.

6.3.2 Hit-based matching

When no MRD tracks are found, the SciBar track is extrapolated to the MRD detector to look for contiguous hits, identified as a short muon track. The requirement for the hit position must satisfy:

$$tan(\theta - \theta_{max}) \times \Delta Z - Z_0 < \Delta L < tan(\theta + \theta_{max}) \times \Delta Z + Z_0, \tag{6.4}$$

where θ is the angle of the SciBar 2D track with respect to the beam direction. ΔZ is the distance between the downstream edge of SciBar and the MRD hit position in the z-dimension. ΔL is the distance between the extrapolated position and the MRD hit position in the x or y dimension. θ_{max} is set to 0.5 radians and Z_0 is set to 10 cm. The requirement is basically a cone with an aperture of ±0.5 radians and a transverse offset within 10 cm of the extrapolated SciBar track at the upstream edge of the MRD. Figure 6.3 shows an schematic drawing of the matching between SciBar and MRD detector.

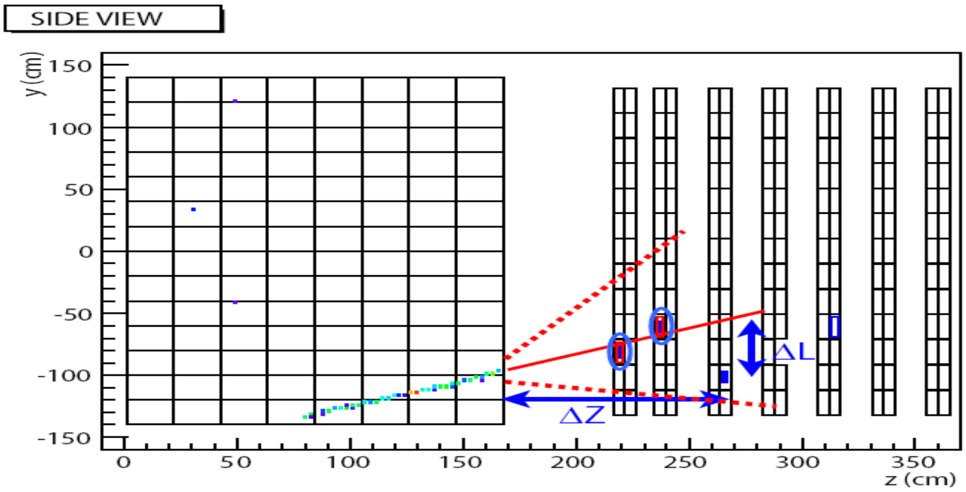

Figure 6.3: Schematic drawing of the SciBar-MRD track matching. The solid line represents the extrapolation from the SciBar track. The dashed lines shows the boundaries. The hits with a circle correspond to the SciBar-MRD matching hits.

Chapter 7

Data set and quality cuts

7.1 Data-taking

The SciBooNE data-taking started on June 8th June 2007 and was completed on August 18th 2008. On that period, the neutrino and anti-neutrino data were collected in three runs (see table 7.1). The figure 7.1 shows the history of the accumulated number of protons on target (POT). A total of 2.64×10^{20} POT were collected although 2.52×10^{20} POT remains after data quality cuts, see section 7.2. For this analysis, the full neutrino data of 0.99×10^{20} POT has been used.

Run	mode	Period	POT
I	anti-neutrino	June - August (2007)	$0.52{\times}10^{20}$
II	neutrino	October(2007) - April(2008)	$0.99{\times}10^{20}$
III	anti-neutrino	April - August(2008)	$1.01{\times}10^{20}$

Table 7.1: Summary table of the SciBooNE data-taking periods.

7.1.1 Stability of beam data-taking

The stability of the beam data-taking was checked periodically at semi-online level. This process is based on counting the number of charged current (CC) candidates occurred in SciBar. The CC-candidates must fulfill the following requirements:

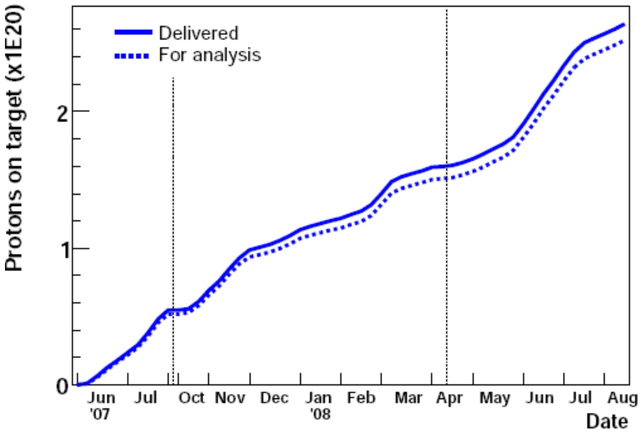

Figure 7.1: History of accumulated POT for the complete SciBooNE data-taking.

1. **Number of hits**: Three or more hits per view, with more than two photo-electron threshold each.

2. **Tracking algorithm**: an additional tracking algorithm, different from sbcat, was performed exclusively to check the data-taking stability. The algorithm simply looks for contiguous hits in each view to reconstruct 2-dimensional tracks. Three dimensional tracks are constructed by matching the edges of the 2-dimensional tracks.

3. **Muon candidate**: The longest track must penetrate more than four layers in SciBar, reaching the most downstream SciBar layer. This track is considered a muon candidate.

4. **Fiducial volume**: The neutrino interaction vertex, defined as the upstream edge of the muon candidate, must be inside of SciBar fiducial volume ($\pm 130cm$ for x and y and $2.62 < z < 157.2$cm for z).

5. **Event time**: The time of the event, obtained as the mean time of muon candidate hits, must be inside of the 2 μs beam time window.

It is important to remark that this criteria is only for data stability checks, not for the analysis presented here. Figure 7.2 shows the beam data-taking stability represented by he number of charged current events normalized to the number of protons on target. The Booster neutrino beam receives 2 to 6×10^{16}POT/hr, that means 11 to 33 neutrino charged current event candidates every hour or 2 to 8 anti-neutrino events/hr in SciBar. The differences between neutrino and anti-neutrino mode are due to the different neutrino and anti-neutrino cross sections and the positive and negative meson cross section production in the p-Beryllium interactions.

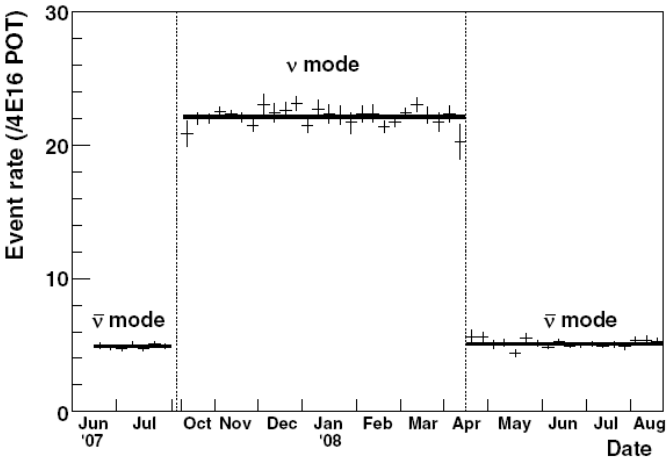

Figure 7.2: Beam data-taking stability measured at SciBar for charged current candidates, normalized to POT.

7.2 Quality cuts

In the SciBooNE data-taking seasons, online checks were frequently made in order to keep a good quality in the data acquisition. These data quality cuts are related to the proton beam, the toroid, the horn current, the targeting efficiency and the GPS time difference (see fig.7.3). The intensity of the primary proton beam is measured on a spill-by-spill basis by using two toroidal transformer, placed at 5 and 200 meters upstream from the target, respectively. Since a typical proton beam contains 4-5$\times 10^{12}$ protons per pulse, only spills with more than 0.1×10^{12} protons per pulse were selected (see fig. 7.3 a). The difference between the readout of the two toroids should be less than 10% to ensure that proton beam was transported correctly (see fig. 7.3 b).

The horn current operates in average at 174 kA (-176 kA in anti-neutrino mode), so values greater than 170 kA are required, fig.7.3 (c). The targeting efficiency measures the fraction of the beam passing through the entire length of the target. The measurements are done with two sets of horizontal an vertical beam position monitors located upstream of the target. Efficiencies larger than 95% were required, fig. 7.3 (d). A synchronization check is done with GPS system, measuring the time difference between the proton beam and the detector trigger system. Since the minimum span between beam spills is 67 msec (proton beam pulse comes out in a row at 15 Hz), a $|t_{beam} - t_{det}| < 10$ ms is required, fig. 7.3 (e).

The data quality cuts rejects less than 1% of the total number of protons on target accumulated during the run. Table 7.2 summarizes the beam quality cuts and fractions of the total number of protons on target that were failure.

Cut	Fail fraction
Proton beam intensity	0.06%
Toroid agreement	0.07%
Peak horn current	0.09%
Targeting efficiency	0.15%
GPS time difference	0.13%

Table 7.2: Beam quality cuts and fractions of total number of protons on target failure.

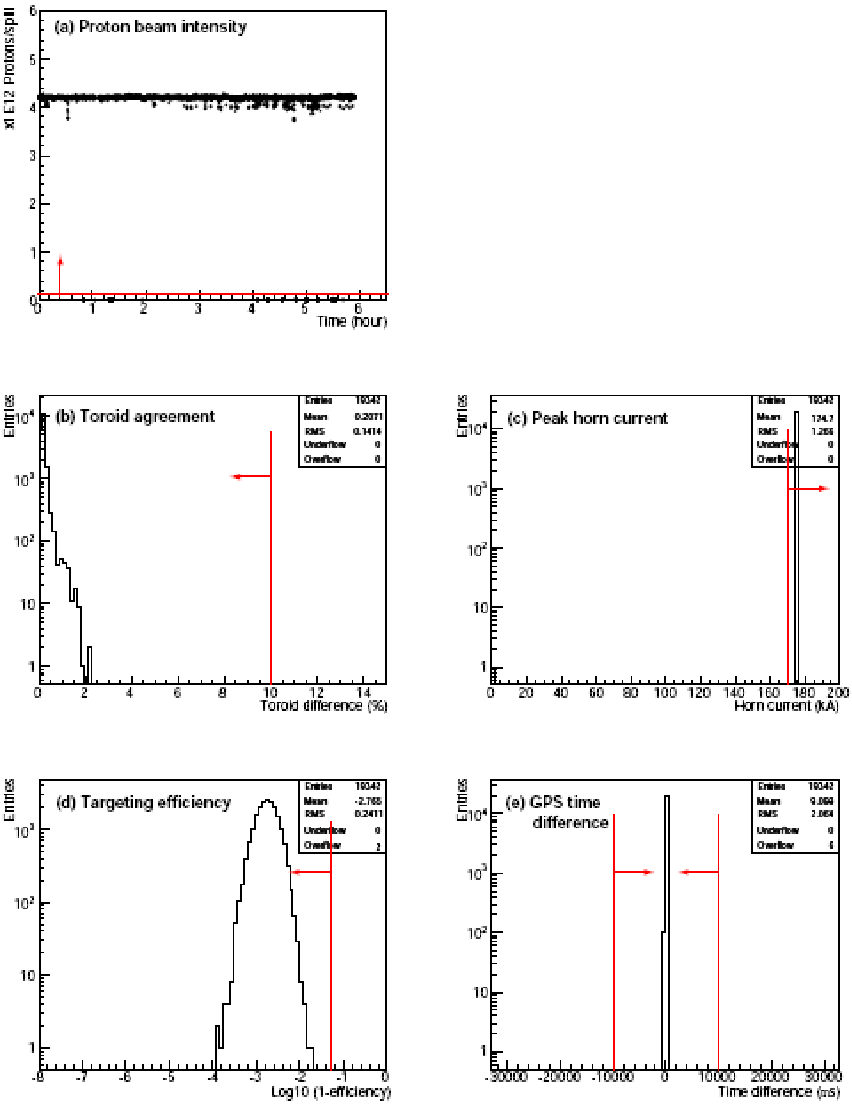

Figure 7.3: Distributions of the beam quality variables for in a typical SciBooNE data-taking check. See section 7.2 for details.

Chapter 8

Charge current quasi-elastic event selection

This chapter is dedicated to the selection of the charged current quasi-elastic (CCQE) events. The CCQE event selection is divided in two parts. The first one describes the selection process to get the charged current sample. The second part is dedicated to the quasi-elastic selection cuts. The last sections analyze the kinematics of the final selection samples.

8.1 Charged current event selection

The charged current sample is selected by applying three cuts to the initial sample: the detector fiducial volume, the beam time window and the muon-track candidate to the event. Detailed description of each cut is discussed below.

Detector Fiducial volume
Many neutrino interactions are generated in the surrounding materials like the walls of the detector hall and dirt. The particles produced outside can penetrate into the detectors. This background can be rejected by requiring that neutrino interactions are produced in a certain inner SciBar volume, called fiducial volume (FV). Hence, a neutrino interaction vertex, defined as the upstream edge of the largest SciBar-track of the event, must be inside of the following SciBar FV limits:

$$-130 < x < 130 \text{ cm}$$

$$-130 < y < 130 \text{ cm}$$
$$2.62 < z < 157.2 \text{ cm (2nd-60th layer)},$$

that corresponds to a fiducial volume mass of 10.6 tons, the 70.7% of the total mass. The effect of the fiducial volume can be seen in figure 8.1. Background events produced by neutrino interactions in the EC and the MRD detectors have been simulated in the MC as well.

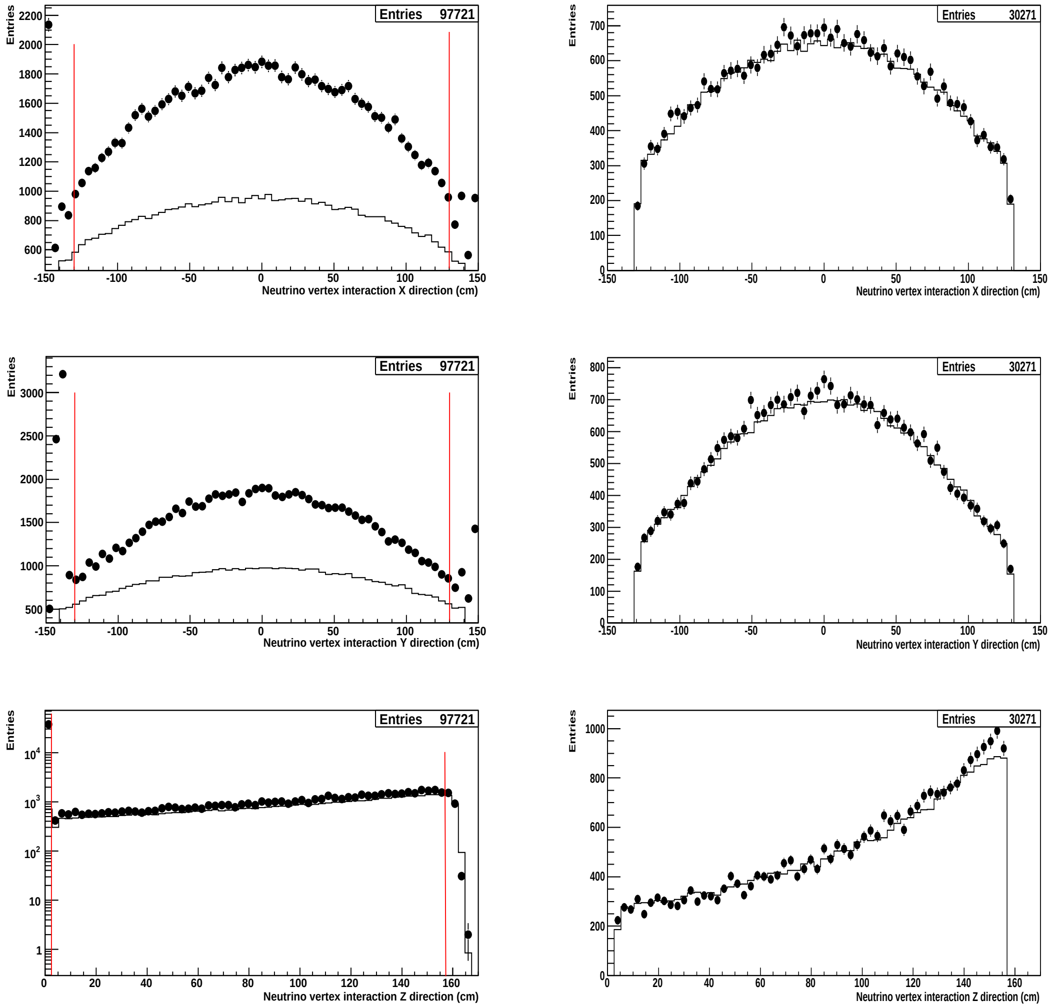

Figure 8.1: Vertex distributions of neutrino interactions in the different projections before (left hand) and after (right hand) the fiducial volume cut. Dots correspond to data and line to MC.

Beam time window

A neutrino interaction event must be produced within the beam time window ($0 < t < 2\mu$s). The event time is calculated as the temporal mean of the hits associated to the largest SciBar-track of the event. Figure 8.2 shows the event time distribution in the temporal window between 0 and 5 μs. The off-time events are mainly produced by cosmic-ray contamination. The cosmic background contamination has been estimated by using a beam-off time window ($10 < t < 12\mu$s) and represents only a 0.6% of the total events that are inside of the beam time window.

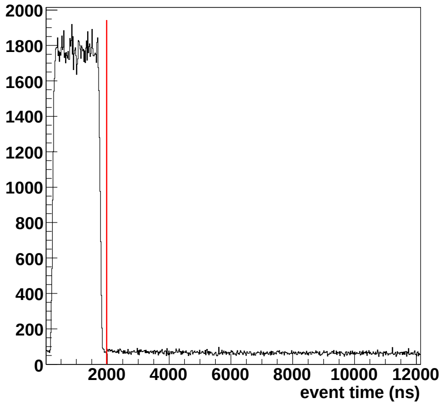

Figure 8.2: Event time distribution for data.

Muon track candidate

A charged current event is selected by requiring at least one muon-track. In this analysis, the muon-track candidate is defined as the SciBar track that reaches the MRD (SciBar-MRD matched track), which also correspond with the longest track of the event (see section 6.3 for details).

In summary, the charged current (CC) inclusive sample is defined as the sample with the following cuts: (a) the SciBar FV, (b) the beam time window and (c) a muon-track candidate. The CC-inclusive efficiency is calculated from MC as follows:

$$CC\ efficiency = \frac{CC\ events}{CC\ events\ in\ SciBar\ FV} = 29.8\%, \tag{8.1}$$

The CC inclusive efficiency is reduced when the μ-candidate cut is applied, see table 8.1. The μ-candidate cut rejects CC events where the muon stops in SciBar or in the EC and also muons with high angle escaping from sides of the SciBar detector. The small variation of CC-inclusive efficiency in the beam time cut is due to particle decays in off time window. The CC inclusive sample has been used to normalized the MC in this chapter.

cut	DATA events	MC events	CC-inclusive efficiency(%)	CC-inclusive purity(%)
SciBar FV	201017	115463	100.	79.8
Beam time	138345	115222	99.8	79.8
μ-candidate	**30271**	30271	**29.8**	**92.7**

Table 8.1: Summary table of the CC-inclusive selection cut. MC is normalized to the CC-inclusive sample.

8.2 Quasi-elastic event selection

Three samples have been selected in the analysis. These samples are the result of applying five cuts over the charged current inclusive sample (see sketch 8.3). With the first three cuts, the 1-track sample has been extracted. Two additional cuts have allowed to get both, the 2-track CCQE and the 2-track non-CCQE enriched samples. A complete description of each one of the cuts is exposed in the following subsections.

8.2.1 Muon track type

The charged current sample can be subdivided in three samples, according to the downstream edge of the muon-track. When the muon-track cross all the MRD planes, with hits in the last MRD layer, the muon is called a penetrated-muon (type 2). The muon that escapes from sides corresponds to side escaped-muons (type 1). If the muon does not satisfy the two previous conditions, that is, stops inside of MRD, the muon is called stop-muon (type 0) and the sample is called the muon-stop sample. Figure 8.4 shows the event distribution according to the muon type. Data/MC differences are present in the three kind of samples. Systematic

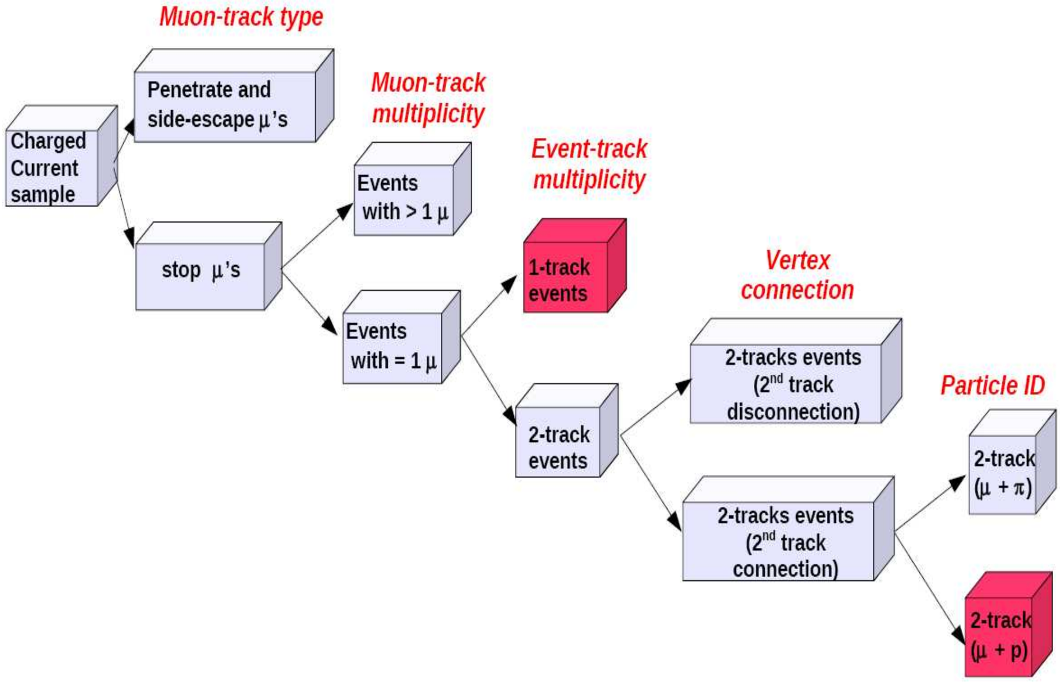

Figure 8.3: Sketch representing the CCQE cut selection. The sequence of the cuts read from left to right, starting with the charged current sample. The cut is identified by the red text and the resultant CCQE samples with red squares. See text for details.

sources related to the flux can explain the data/MC differences. In particular, the data deficit around 20% observed in the muon-penetrating type is due to the large uncertainties at high-energy flux coming from kaons decays, as plot 10.3 in the section 10.3 will show. For this analysis, the muon-stop sample has been selected. In this case, the muon energy is captured within the different detectors and the event kinematics is completely defined. However, the muon-penetrated and muon-side escaping samples will be considered for further studies. The muon-stop sample contains a 67% of the CCQE events from the CC inclusive sample.

The muon-penetrated and muon side-escaped samples could be introduced in the analysis to increase the statistics, specially at high energies. However at these energies, the flux is characterized by large errors, as commented above. So, no significative improvments in the final measurement of the cross section would be expected.

cut	DATA events	MC events	CCQE efficiency(%)	CCQE purity(%)
CC-inclusive	30271	30271	31.8	58.1
μ-stopping in MRD	21711	20604	21.3	55.9
Muon track multiplicity	20920	19774	21.0	57.6
1-SciBar track	**13585**	13351	**16.3**	**66.2**
2-SciBar tracks	5744	4922	4.5	49.8
cuts in 2-track sample				
Vertex Connection	4543	4107	4.3	56.2
dE/dx (p-like)	**2915**	2713	**3.4**	**68.5**
dE/dx (π-like)	1628	1394	0.8	32.3

Table 8.2: Summary table of CCQE selection cut based on event topology. Efficiency calculated with respect to the CCQE events in the SciBar fiducial volume.

8.2.2 Muon track multiplicity

In a CCQE interaction only one muon is produced, then only one muon-track per event is required. Remind that muon-track is defined as a SciBar-MRD matched track. Figure 8.5 shows the muon-track multiplicity per event corresponding to the muon-stop sample. The presence of QE and CCπ events with two SciBar-MRD tracks indicates that, apart from the muon-track candidate, high energy protons or pions reach the MRD detector, even decay in flight pions. The CCQE events with two SciBar-MRD matched tracks has not been considered in the analysis to avoid muon miss-identification.

A data deficit is observed at high muon-track multiplicity, dominated by CC-multi pion and deep inelastic scattering (DIS). The data/MC difference comes from uncertainties in the cross section and final states interactions of CC-multi pion and deep inelastic interactions (represented by blue color in MC).

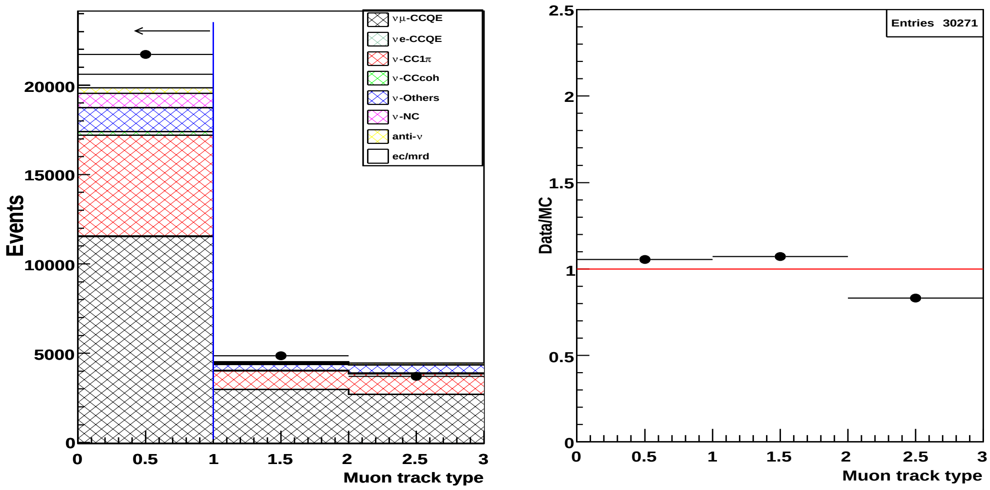

Figure 8.4: Event distributions according to the type of muon. Type 0 indicates muon-stopping, type 1 muon-side escaping and type 2 muons-penetrating. MC is normalized to the CC inclusive sample.

8.2.3 Event track multiplicity

This cut is based on the track multiplicity of the event, searching for two tracks that characterize the CCQE events. Then, two SciBar tracks per event are required, the already mentioned muon-track (a SciBar-MRD track) plus and additional only SciBar track. However, there are many CCQE events in which the second track (proton) is not visible. That occurs when a proton is absorbed inside of the nucleus or if its energy is below of the threshold to be reconstructed. For these reasons, the 1-track events are selected as well. Figure 8.6 shows the distribution of number of tracks per event corresponding to events which already passed the previous CCQE cuts. A data/MC disagreement is observed at high multiplicity tracks. Under-estimation of the CC1π contamination can explain such an effect, as later will be shown.

This cut selects one track and two track events producing the so-called 1-track and 2-track samples. Both samples are treated separately. The CCQE purity for the 1-track sample is 65.1%, but the 2-track sample is only of 49% (see table 8.2). The low 2-track purity comes from the presence of a high fraction of CCπ events. These events have a topology similar to the quasi-elastic events, both producing

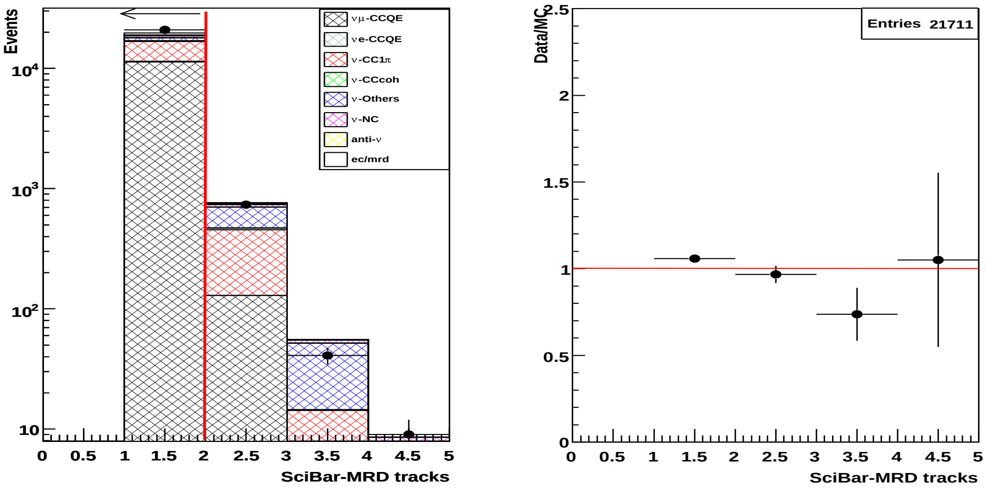

Figure 8.5: Distribution of the number of muon track multiplicity per event. MC is normalized to the CC inclusive sample.

two final states, so they are concentrated at 2-track sample. Two additional cuts has been used in the 2-track sample in order to increase its CCQE purity. The cuts are based on the information extracted from the non-muon track candidate, here referred as the second track.

8.2.4 Vertex connection

The vertex connection cut takes advantage of a topological characteristic of the quasi-elastic events. In a CCQE interaction, the proton is always produced at the interaction vertex. That property is used to reject nonQE events (CCπ^0 and $anti-\nu$ interactions), where the second tracks (gammas and proton coming from neutron interaction) are generated detached from the neutrino interaction vertex.

The connection vertex distance is defined as the three dimensional distance between the neutrino interaction vertex and the upstream edge of the second track. Left hand plot from figure 8.7 shows the connection vertex distribution for the 2-track sample. The cut has been fixed at 10 cm, obtained as a result of maximizing the CCQE efficiency times purity of the cut value (in fig. 8.7, the right hand plot).

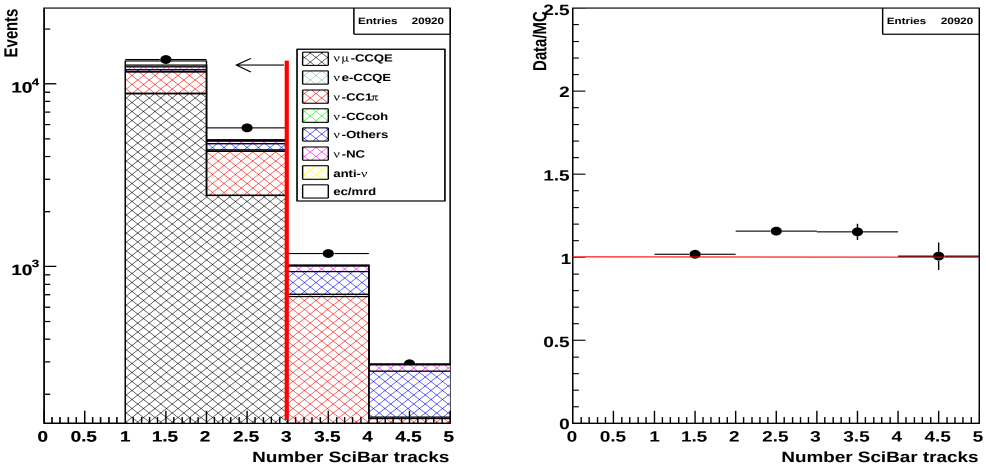

Figure 8.6: The distribution of number of SciBar tracks for the muon-stop sample. MC is normalized to the CC inclusive sample.

8.2.5 Particle identification

Moderatively relativistic charged particles lose energy in matter primarily by ionization and atomic excitation. The deposited energy per unit of length (dE/dx) is different for each kind of particle and momentum and can characterize them in a particular medium.

The dE/dx capabilities in SciBar detector allows to identify muons from protons as well as pions from protons. The figure 8.8 shows the dE/dx distribution for muons, pions and protons in the SciBar detector (extracted from Monte Carlo). Muons usually have large momenta, so they behave as minimum ionization particles (mip). In opposite, protons are characterized by low momenta, depositing large amount of energy (defined as heavy ionization particles). The pion particle in our sample can behaves as a mip or heavy ionization particle, depending of its momentum. The dE/dx technique has been used in this analysis to distinguish protons from pions, assuming protons as heavy ionization particles and pions as mip particles.

The particle identification cut has been performed using the cumulative function of the dE/dx distribution corresponding to a muon (fig. 8.9). The muon cumulative function is itself the muon confidence level (MuCL), representing the probability

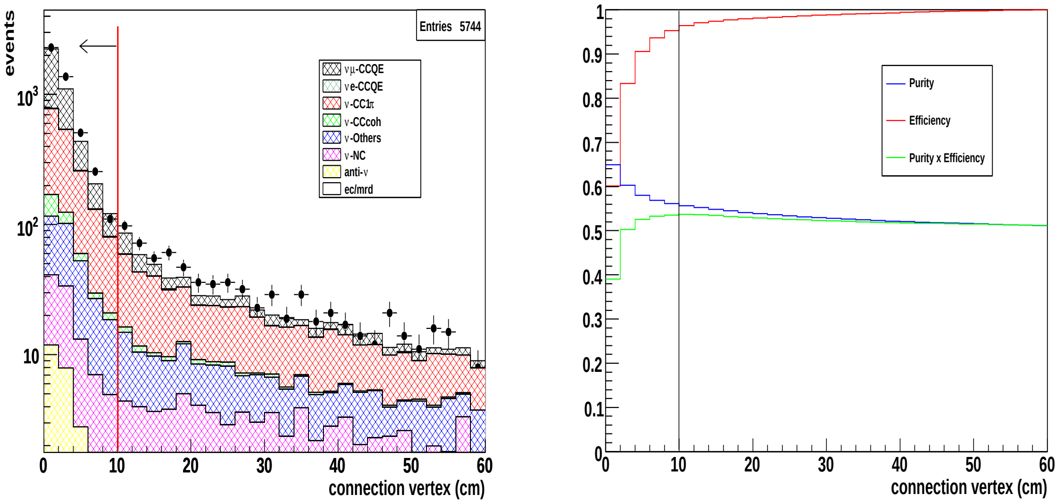

Figure 8.7: On the left, the vertex connection distribution for the 2-track sample. On the right, the efficiency, purity and the product for different connection vertex cuts. MC is normalized to CC-inclusive sample.

of a particle to be a mip based on its dE/dx.

The MuCL variable is then used to evaluate the probability of being a mip particle. Figure 8.10 shows the MuCL distribution of the second track corresponding to the 2-track sample. At the MuCL value of 0.05, one can observe how clearly protons are separated from pions. This MuCL value is the result of maximizing the CCQE efficiency times CCQE purity from several MuCL values (in fig. 8.10, the right hand plot).

Note that, in figure 8.10, apart from pions, electrons and muons are also present. The reason comes from the inefficiency reconstruction of the second track and the way the reconstructed tracks are tagged with a true particle type. The true information is contained in the hits of the reconstructed track. So, a reconstructed track is tagged by looking at the highest fraction of the hits with the same true particle type information. Some reconstruction inefficiencies in the second track can produce the presence of other hits than the true proton ones. Those hits can contribute to mis-identify the reconstructed particle.

In summary, the MuCL cut allows to separate quasi-elastic from non

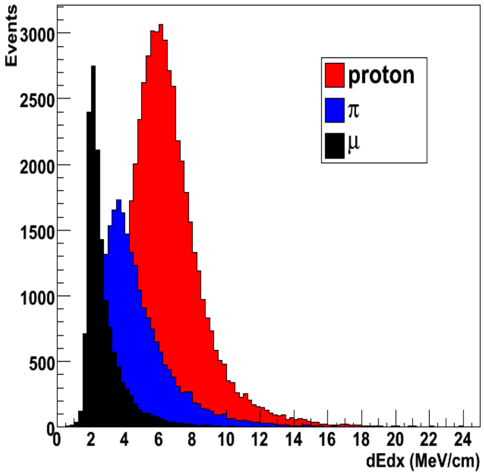

Figure 8.8: Typical dEdx distributions for proton, pion and muon in the SciBar detector, extracted from MC.

quasi-elastic events[1]. The events with MuCL values lower and larger than 0.05 are classified in 2-track enriched QE and nonQE samples, respectively. Table 8.2 shows efficiency and purity numbers for both samples.

8.3 Reconstructed kinematics

8.3.1 Muon kinematics

Two muon kinematic variables has been analyzed in detail, the muon momentum (P_μ) and the muon angle (θ_μ). This information is enough to reconstruct the neutrino energy assuming CCQE kinematics, as later is shown. The muon angle is directly extracted from the information reported by the reconstruction software, calculated as the angle of the muon-track with respect to the z-direction (or beam direction). The muon momentum has been derivated from the muon energy (E_μ). This energy is calculated by the range and the expected energy deposition in each one of the detectors, mathematically expressed as follows:

---

[1] The $\Delta\Theta_p$ cut, used to separate QE from nonQE was studied as well but not considered for the analysis (see details in appendix F)

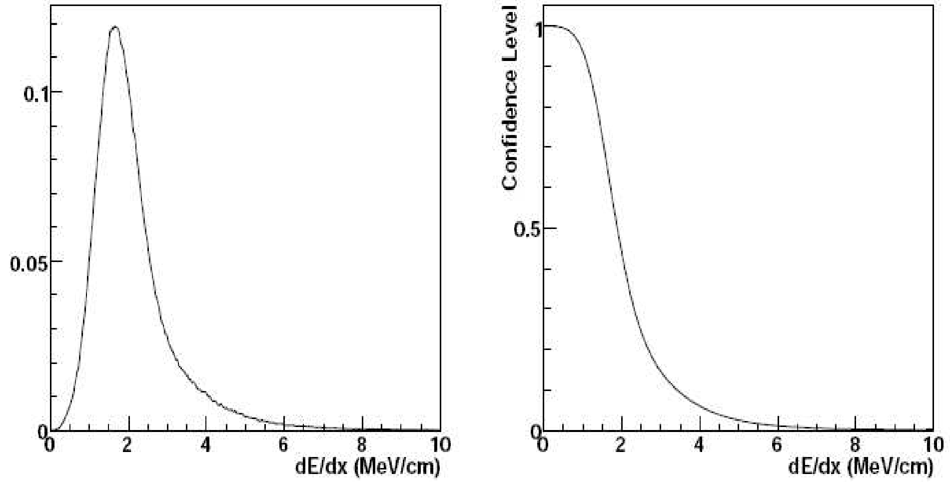

Figure 8.9: dEdx distribution of a typical cosmic muon (left) and the cumulative function or confidence level associated to the muon dEdx distribution (right).

$$E_\mu = \left(\frac{dE}{dx}\right)_{SB} \times L_{SB} + \frac{\Delta E_0^{EC}}{cos\theta} + E^{MRD} \times L_{MRD} \qquad (8.2)$$

where L_{SB} and L_{MRD} correspond to the muon track length within the SciBar and the MRD detectors respectively. The $(dE/dx)_{SB}$ represents the deposition energy per unit of length in SciBar, set to 2 MeV/cm [76]. The ΔE_{EC} is the energy deposited in the EC by a minimum ionizing particle crossing horizontally. This energy is set to 91 MeV, estimated with the GEANT4 simulation. The E_{MRD} is calculated from a range to energy lookup table based on the MC simulation.

The muon momentum and muon angle resolutions (see figure 8.11) are around 50 MeV and 0.9 degrees. The values are calculated as the difference between the reconstructed and the true quantity, both estimated from the MC simulation.

8.3.2 Neutrino kinematics

The neutrino energy can be reconstructed using only the muon momentum and the muon angle information and assuming CCQE kinematics. The expression is written as follows:

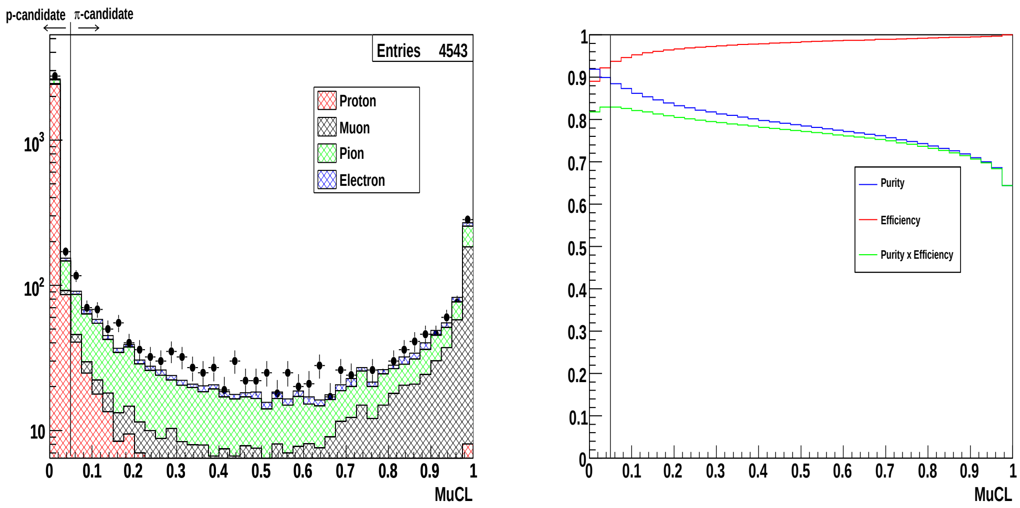

Figure 8.10: On the left, the MuCL distribution for the 2-track sample after passing the connection vertex cut. On the right, the the CCQE efficiency and CCQE purity for different MuCL values. MC is normalized to CC-inclusive sample.

$$E_\nu^{rec} = \frac{1}{2}\frac{(m_p^2 - m_\mu^2) - (m_n^2 - V^2) + 2E_\mu(m_n - V)}{(m_n - V) - E_\mu + p_\mu cos\theta_\mu}, \tag{8.3}$$

where m_p, m_n and m_μ correspond to the proton, neutron and muon mass respectively. V is the nuclear potential set to 27 MeV[62]. In similar way, one can derive the expression of the reconstructed momentum transfer, expressed as follows:

$$Q_{rec}^2 = 2E_\nu^{rec}(E_\mu - p_\mu cos\theta_\mu) - m_\mu^2, \tag{8.4}$$

The figure 8.12 shows the expected resolution for the reconstructed neutrino energy and the momentum transferred for the SciBar-MRD stopped sample. Note that two peaks are present in the energy resolution distribution. The smallest peak, shifted from cero, corresponds to CC nonQE interactions whose energies has been reconstructed assuming CCQE kinematics. The largest peak is slightly shifted from cero, the reason leads on the fact that the Fermi momentum has not been considered for reconstruction energy calculations. Just to mention that, for the cross section measurement, the neutrino energy information does not come from the reconstruction variable but from MC true energy templates.

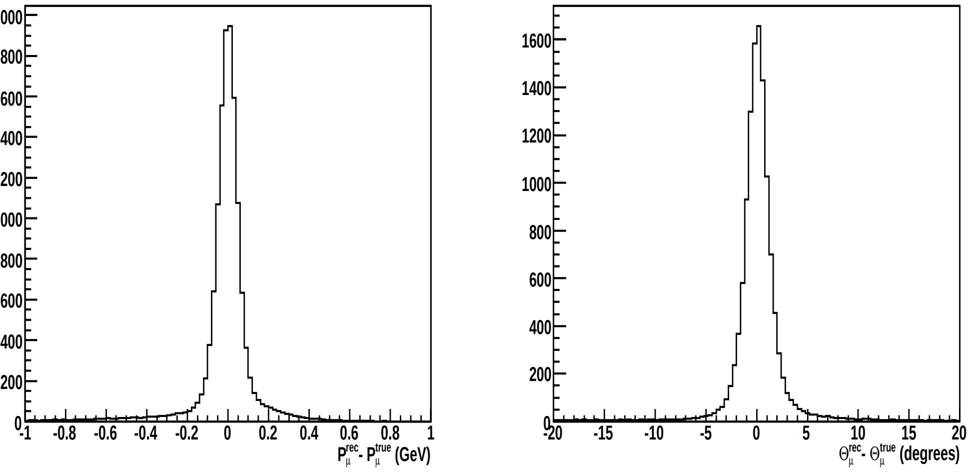

Figure 8.11: From left to right, the muon momentum and muon angle resolution distributions for the SciBar-MRD stopped sample, extracted from MC.

8.4 1 track sample

A typical 1-track event in the SciBooNE display is shown in figure 8.13. The muon momentum (P_μ), muon angle (Θ_μ), reconstructed neutrino energy (E_ν^{rec}) and the momentum transfer (Q^2_{rec}) for the 1-track sample are shown in figure 8.15. The MC is broken up in different neutrino interaction channels (see color code in figure 8.14). The P_μ and E_ν^{rec} variables present good data and MC agreement, however the Θ_μ and Q^2_{rec} shows a data/MC disagreement, large at high muon angles. Alignment problems has been discarded because of the alignment resolution is around few millimeters (see alignment section 4.5). A detailed study of muon angle discrepancies is presented later on, in section 10.7

8.5 The 2-track QE/nonQE enriched samples

A typical event display of a 2-track QE enriched sample is shown in Figure 8.16. The muon kinematics (P_μ, Θ_μ), the neutrino energy and momentum transfer (E_ν^{rec} and Q^2_{rec}) have been analyzed for both, the QE and nonQE enriched samples (see figures 8.17 and 8.18). In the case of the 2-track QE enriched sample, a significant data/MC disagreement is observed at low Q^2 region, not observed in the 2-track

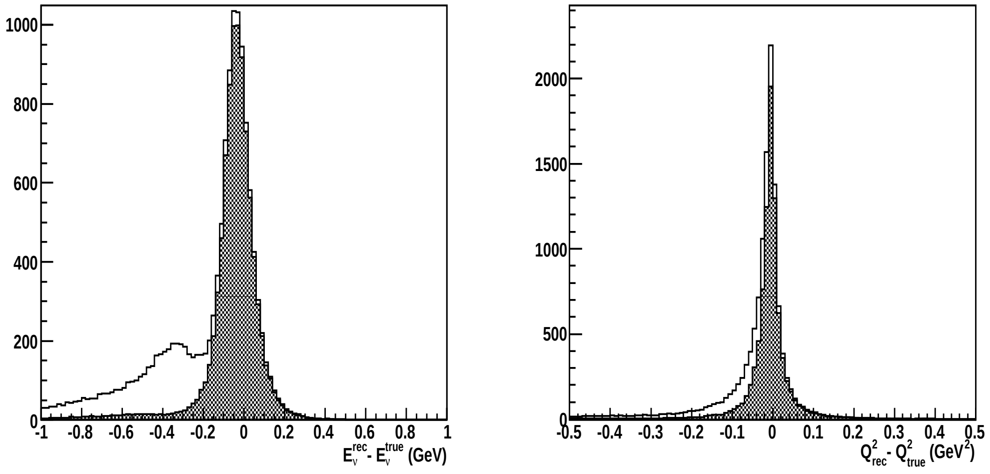

Figure 8.12: Reconstructed neutrino energy and momentum transfer resolution for the MRD stopped sample. The black histogram represents the fraction of CCQE events.

nonQE sample. The data excess is observed below 0.15 GeV^2, where the MC predicts no CCQE events due to the minimum energy transfered to the proton. The section 8.6 is dedicated to the study and explanation of such an effect.

The kinematic distributions for the 2-track nonQE sample present a good data/MC agreement except for the total amount that, as later will be shown, is due to the MC under-estimation of the CCπ interactions.

8.5.1 Second track kinematics

The kinematics associated to the second track has been analyzed as well, in particular the following variables:

1. **Length**: The length of the second track corresponds to the three dimensional distance between the track edges.
2. **Beam angle ($\theta_{p/\pi}$)**: Angle between the second track and the beam direction (z-direction).
3. **Opening angle ($\Delta\phi_{p\mu}$)**: Angle between the second track and the muon-track.

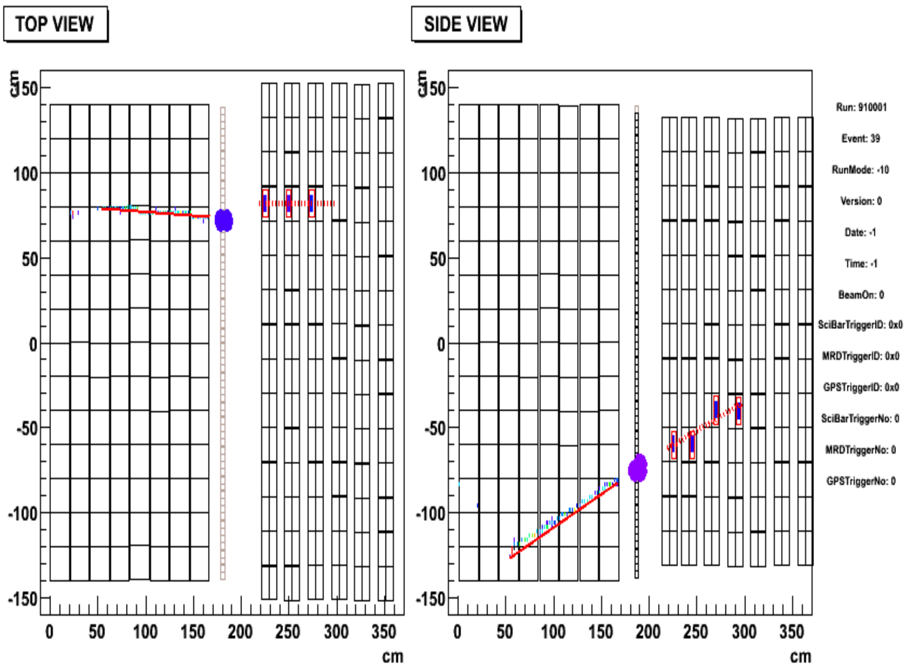

Figure 8.13: Typical SciBooNE display with the top and side view of a selected 1-track event.

4. **dEdx**: Energy deposited in SciBar per unit of length.

The second track kinematics for the 2-track QE and nonQE enriched samples are shown in figures 8.19 and 8.20. In the case of the 2-track QE sample, the data/MC disagreement observed at the at opening angles less than 60 degrees and at high energy deposition (dE/dx) is clearly related to the data-excess observed at low Q^2_{rec} region.

8.6 The low Q^2_{rec} data excess

The Q^2_{rec} distribution for the 2-track QE enriched sample shows a data excess below 0.15 GeV^2. The data excess region has been isolated to investigate the problem, selecting only 2-track QE-enriched events with momentum transfer $Q^2_{rec} \leq 0.15$ GeV. This sample has been called data-excess sample.

The kinematic distributions for the data-excess sample are shown in figure 8.21. In all the distribution, the expected data/MC disagreement is flat, hence no

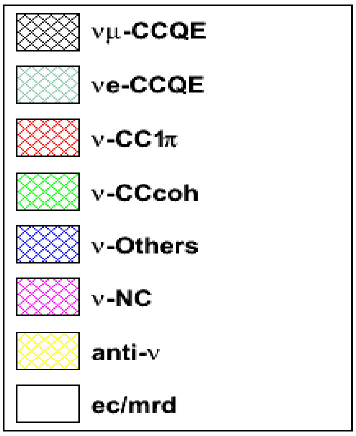

Figure 8.14: Color code for MC interaction channels using NEUT. The ν-Other category includes the CC-multi pions and the deep inelastic interactions.

information can be extracted. Similar behavior has been observed in the kinematics of the second track (see figure 8.22). That is not the case of the vertex activity distribution, defined as the the maximum deposited energy in a strip around the vertex, see fig.8.23. The distribution shows a good data/MC agreement at low vertex activity but a disagreement at high vertex activity region. That fact evidences that the events from the data excess are characterized by high vertex activity.

The vertex activity data/MC differences could be related to the CC resonant pion production. In this reaction, when the pion is absorbed by the nucleus, two or more additional nucleons (like protons) could be emitted after the pion absorption, however these nucleons are not simulated in NEUT, see sketch 8.24. Then, these MC events would be reconstructed as 1-track events, producing the data excess observed in the 2-track QE enriched sample. This effect, called track migration effect, would not have an impact on the 1-track kinematic distributions because of the low statistics in comparison with 1-track sample. Several proofs are presented below to confirm such an argument.

8.6.1 A cross-check using NUANCE

The NUANCE neutrino generator has been used in the MiniBooNE collaboration[36]. Although the NUANCE models and settings are different from the NEUT ones (see table 8.3), it will be particularly useful to check the kinematics of the 2-track QE enriched sample with other neutrino generator. In the NUANCE generator the nucleons emitted after pion absorption (in CCπ interactions) are simulated.

ν-generator	M_A^{QE} (GeV)	kappa	$M_A^{1\pi}$ (GeV)	E_B (MeV)	P_{Fermi} (MeV)
NEUT	1.21	1.022	1.2	27	217
NUANCE	1.23	1.000	1.1	34	220

Table 8.3: Nuclear model settings for NEUT and NUANCE neutrino generators.M_A^{QE} and $M_A^{1\pi}$ correspond with the axial-vector mass for CCQE and CC resonant interactions respectively. The E_B represents the binding energy andP_{Fermi} the Fermi momentum. Kappa is a Pauli suppression parameter added to the RFG (see ref. MiniBooNE).

A Monte Carlo sample has been produced applying NUANCE instead of the default SciBooNE generator (NEUT). Then, a 2-track QE enriched sample has been selected by applying the same CCQE cuts than in the NEUT MC case (see section 8.2). The event kinematic of this sample is shown at the figure 8.25. As one expected, the data/mc comparison is completely different working with other neutrino generator. In this case, the momentum transfer distribution at low region presents a data deficit, just the opposite of what was observed using NEUT MC (see fig. 8.17 for comparison). The same data deficit is shown in the vertex activity distribution (fig. 8.26) when the low Q^2_{rec} region is analyzed.

A filter has been applied to the 2-track QE enriched sample in order to check that the data excess observed in NEUT MC can be reproduced with NUANCE. The filter removes CC1π candidates where the π's generate at least one proton (like the ones of the sketch 8.24). The filter is very simple and of course not rigorous but is enough to reproduce the similar effect than the one observed in NEUT. Figure 8.27 shows the kinematics of the 2-track QE enriched sample after applying this filter and the Q^2_{rec} distribution presents similar data/MC discrepancies than using

NEUT MC.

The NUANCE checks suggest that the data excess observed at low Q^2_{rec} region in the 2-track QE enriched sample is a problem derivated from the NEUT simulation. Nowadays several modifications are being carried out over the NEUT code in order to correct the CCπ candidate related effect. Although it is still very preliminary and needs careful checks, the modified NEUT code would confirm our arguments as figure 8.28 shows.

In summary, the non-simulated NEUT effect produces a migration effect in the MC. Some 2-track nonQE MC events would migrate to 1-track sample, generating a data excess observed in the 2-track QE enriched sample. This migration effect will be taken into account and hence evaluated for the the final measurement of the cross section.

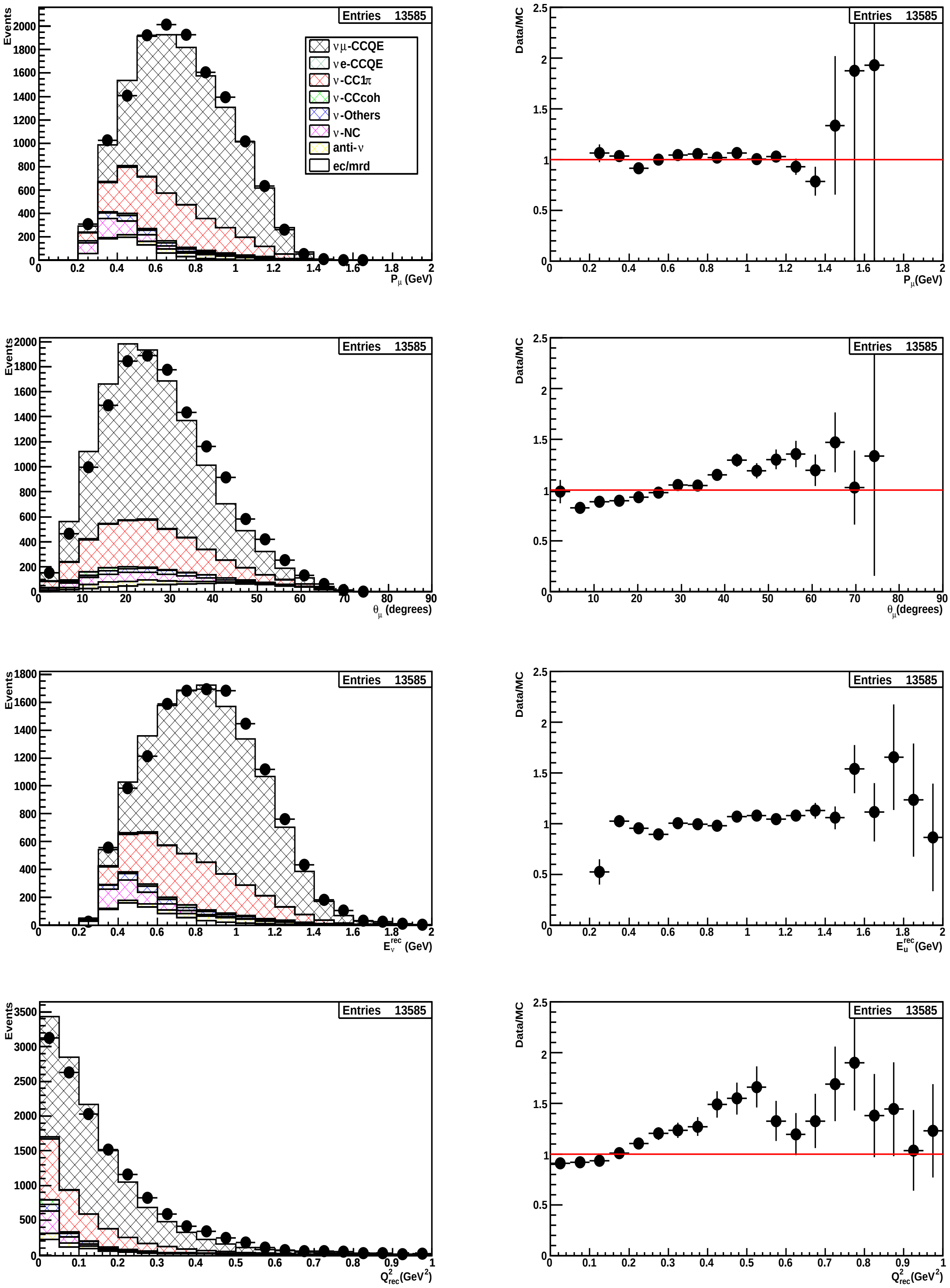

Figure 8.15: Muon (P_μ, θ_μ) and event (E_ν, Q^2) kinematic distributions for 1-track sample. Right hand plots shows data/MC ratio of each distribution. MC is normalized to the CC-inclusive sample.

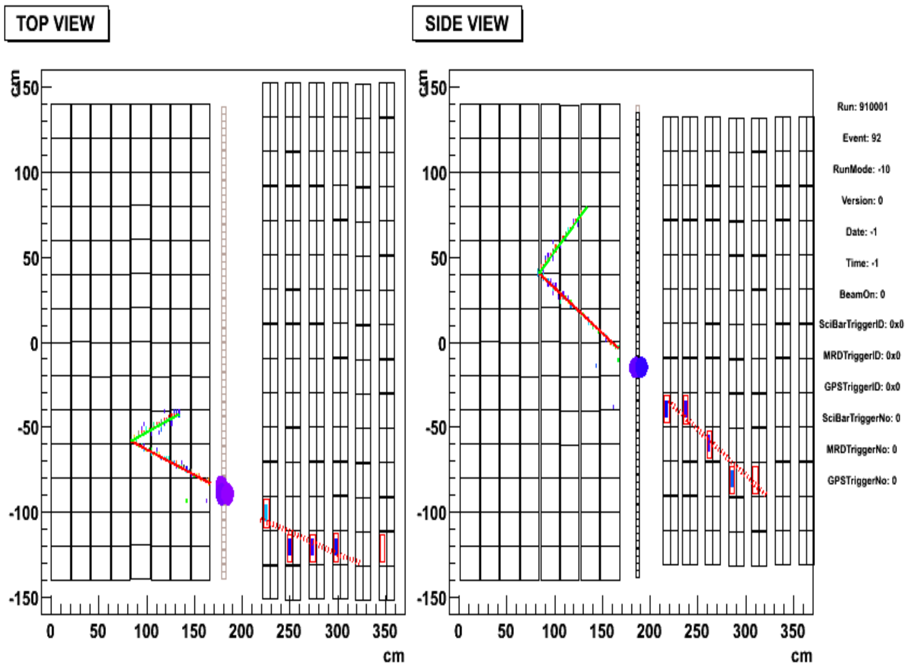

Figure 8.16: Typical SciBooNE display with the top and side views of a selected 2-track QE event.

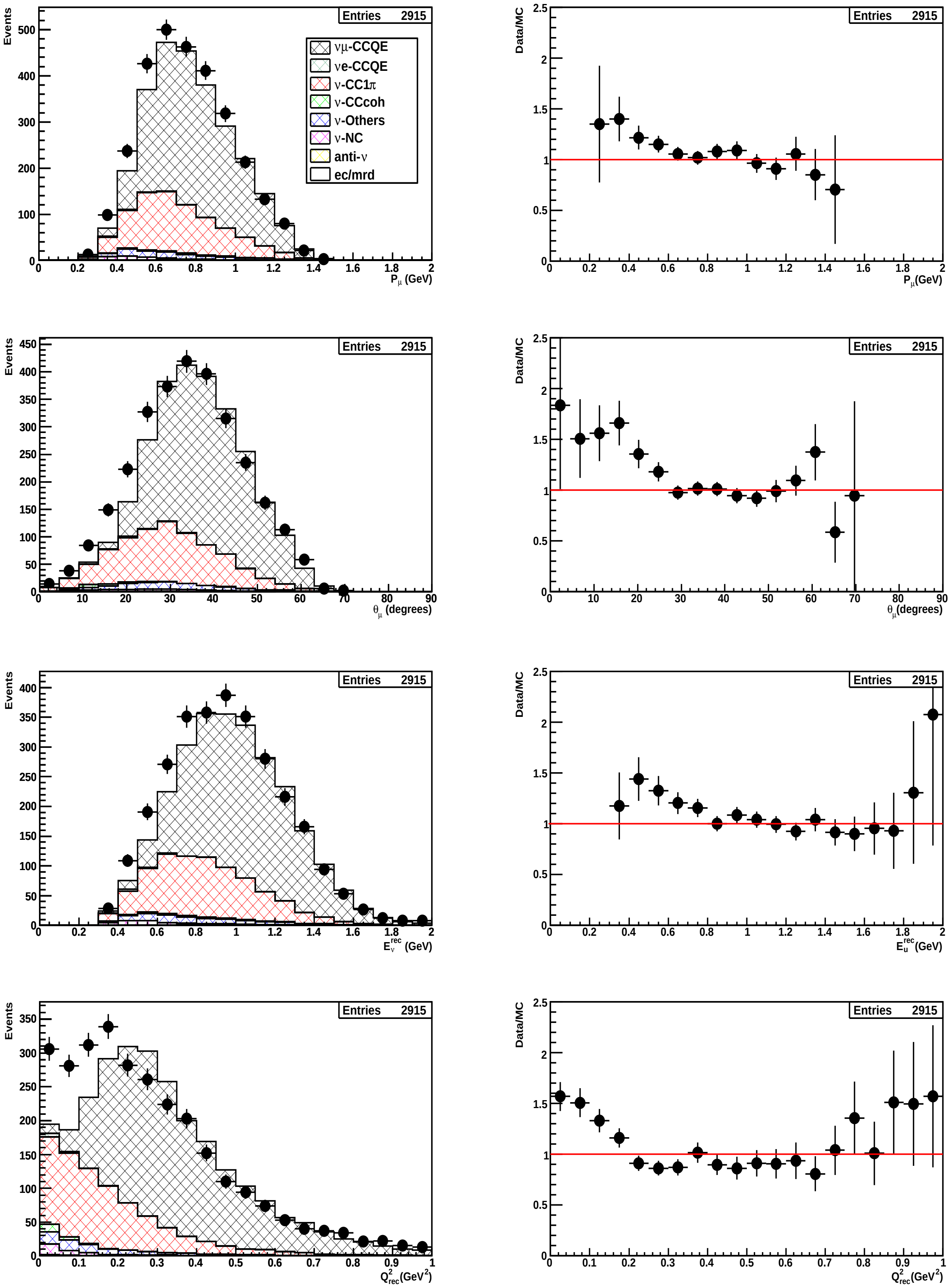

Figure 8.17: Muon (P_μ, θ_μ) and event (E_ν, Q^2) kinematic distributions for 2-track QE enriched sample. Right hand plots shows data/MC ratio of each distribution. MC is normalized to the CC-inclusive sample.

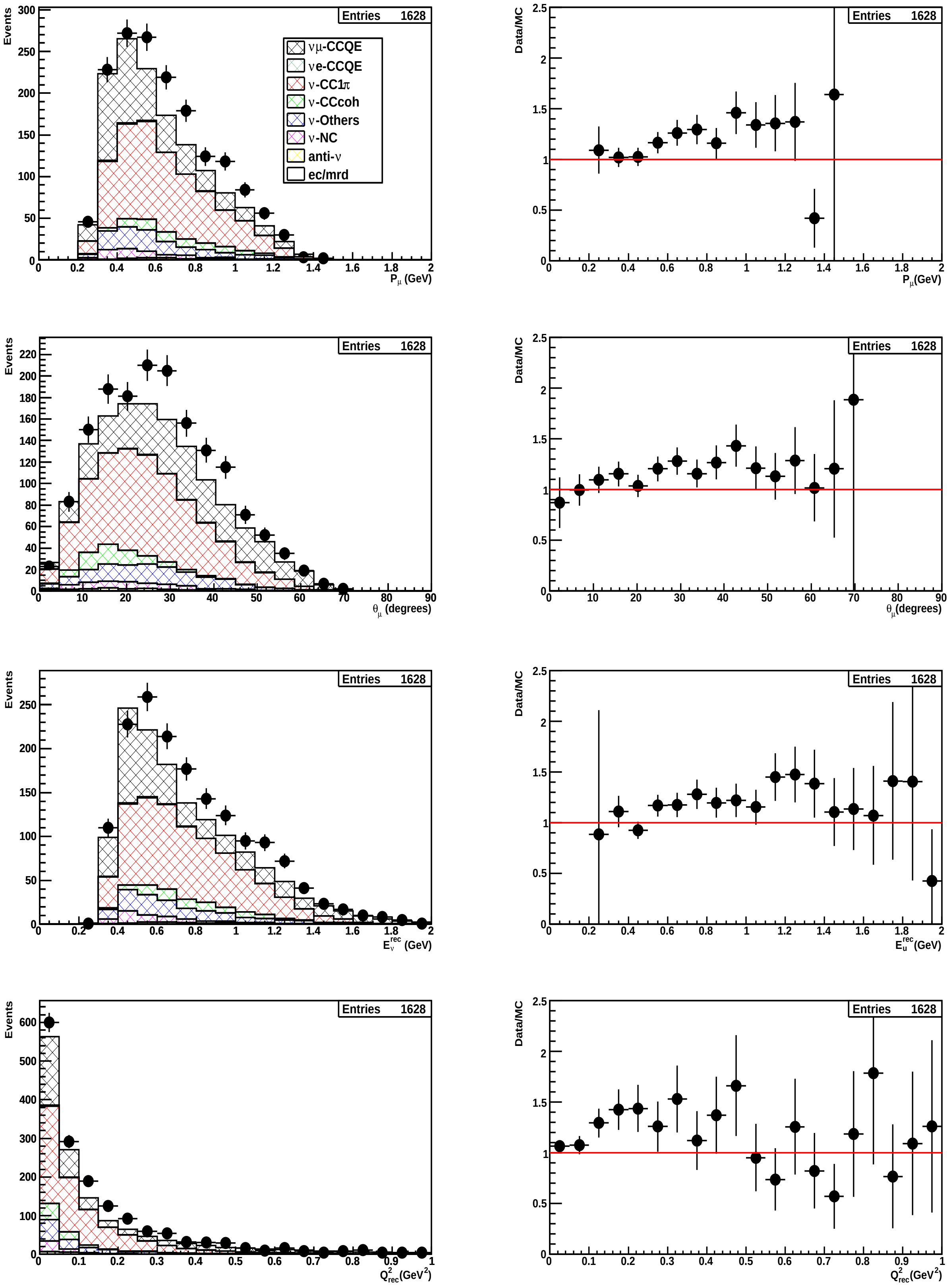

Figure 8.18: Kinematic distributions for the 2-track nonQE-enriched sample. MC is normalized to CC-inclusive sample.

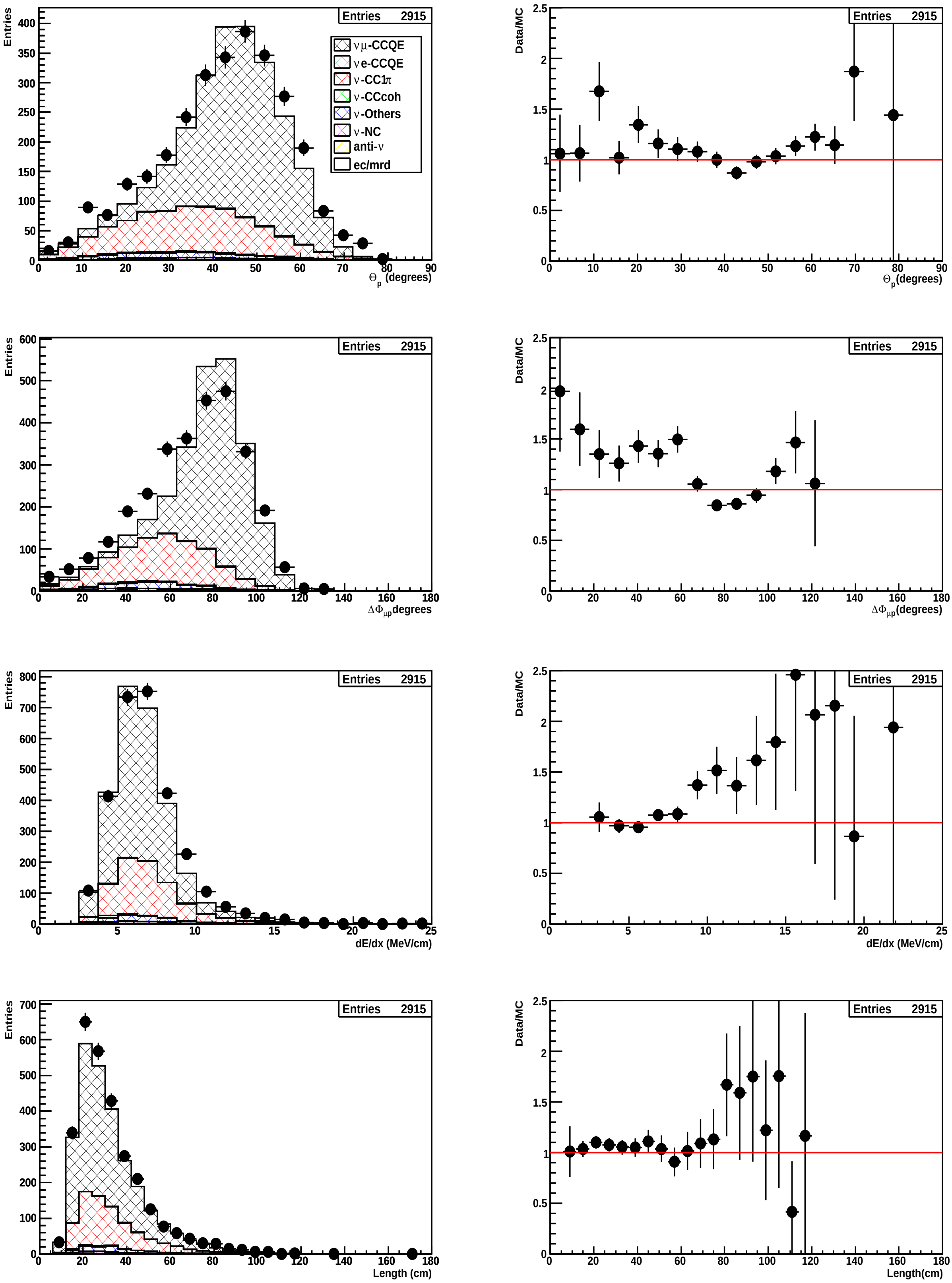

Figure 8.19: Second track kinematics distributions (dEdx,length,$\phi_{p\mu}$, θ_p) for the 2-track QE enriched sample. Right hand plots shows data/MC ratio of each distribution. MC is normalized to the CC-inclusive sample.

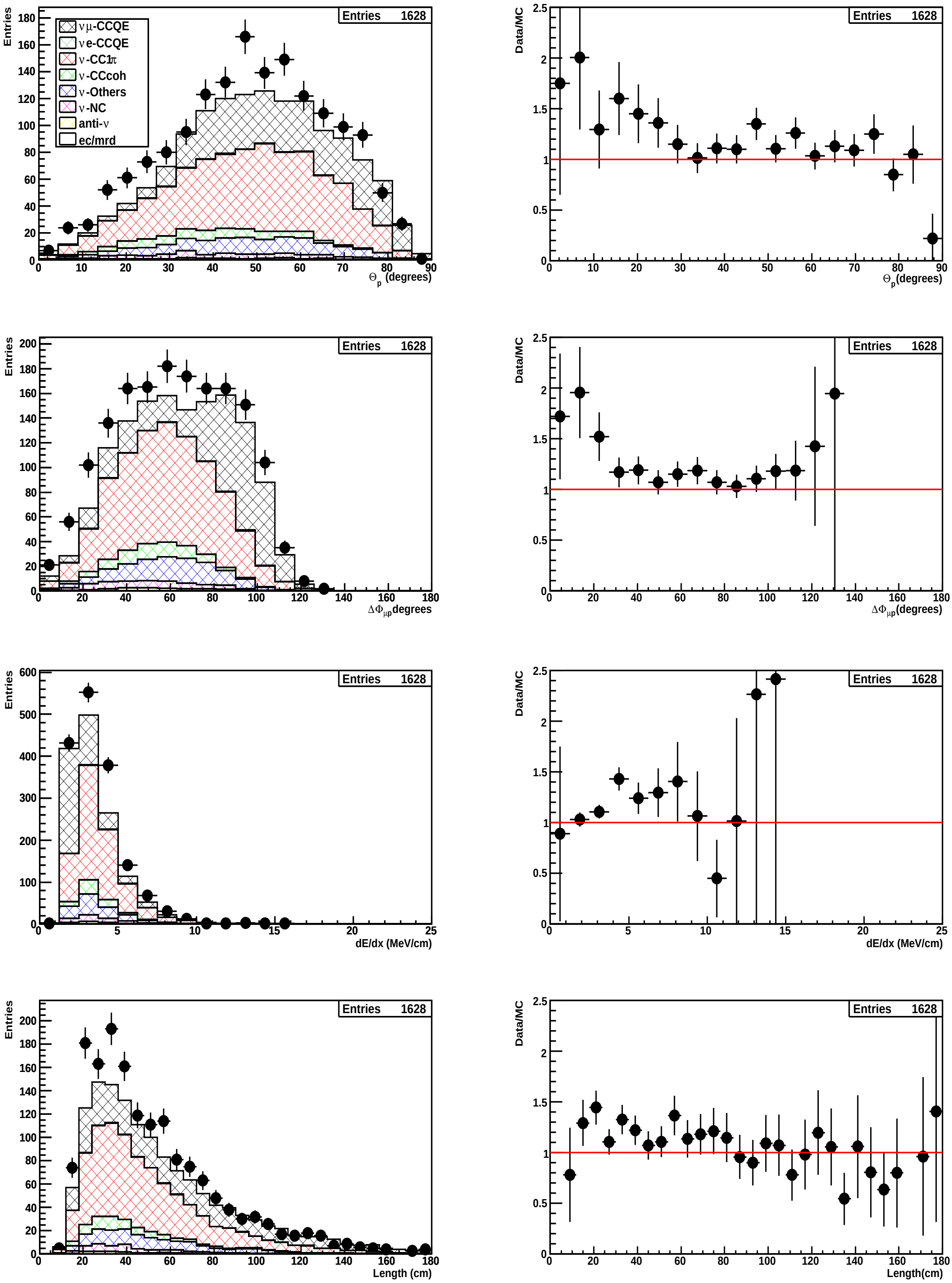

Figure 8.20: Second track distributions for the 2-track nonQE-enriched sample. Right hand plots shows data/MC ratios. MC is normalized to CC-inclusive sample.

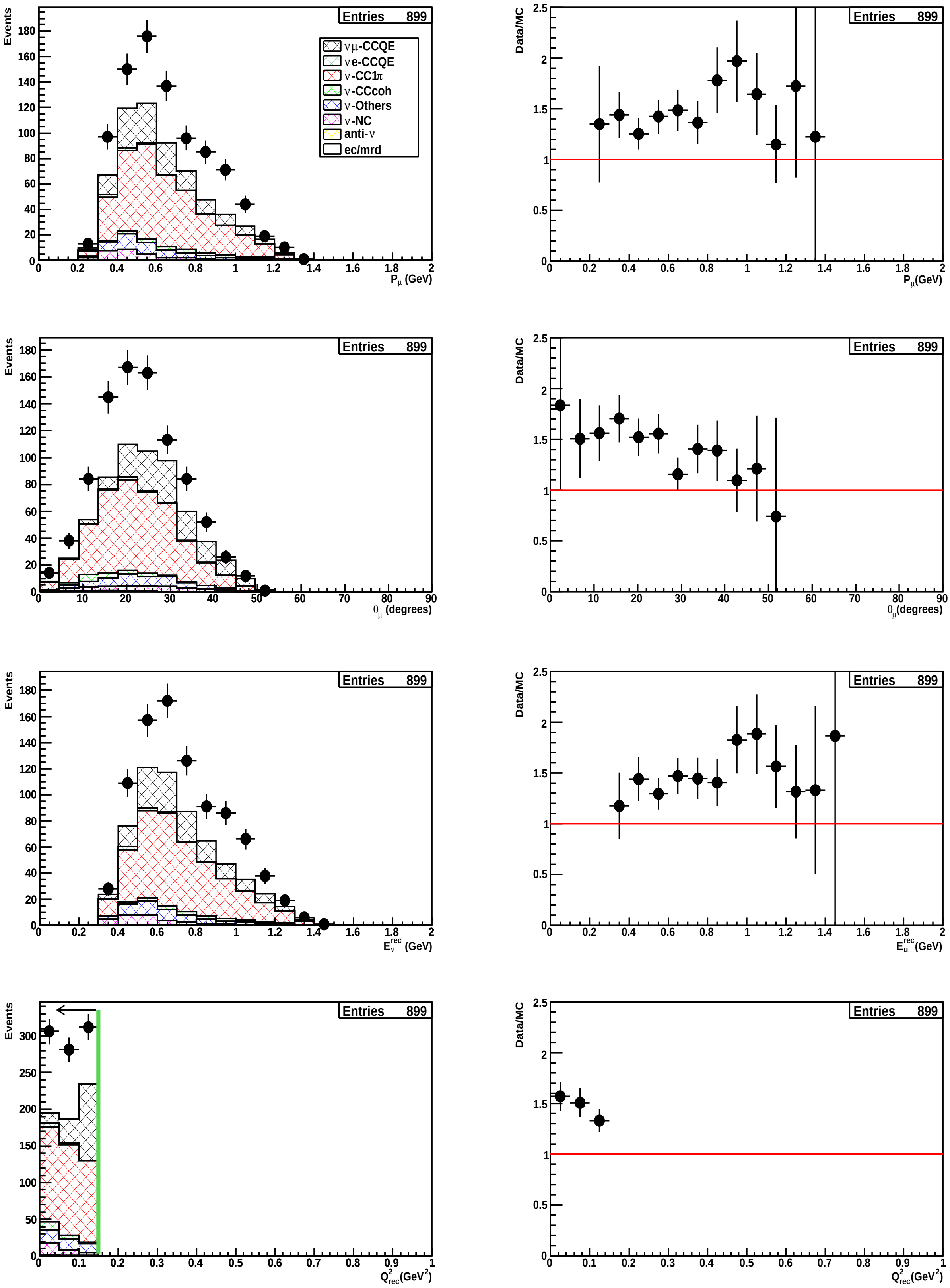

Figure 8.21: Muon and neutrino kinematic distributions corresponding to the data excess sample (see text for details). MC is normalized to CC-inclusive.

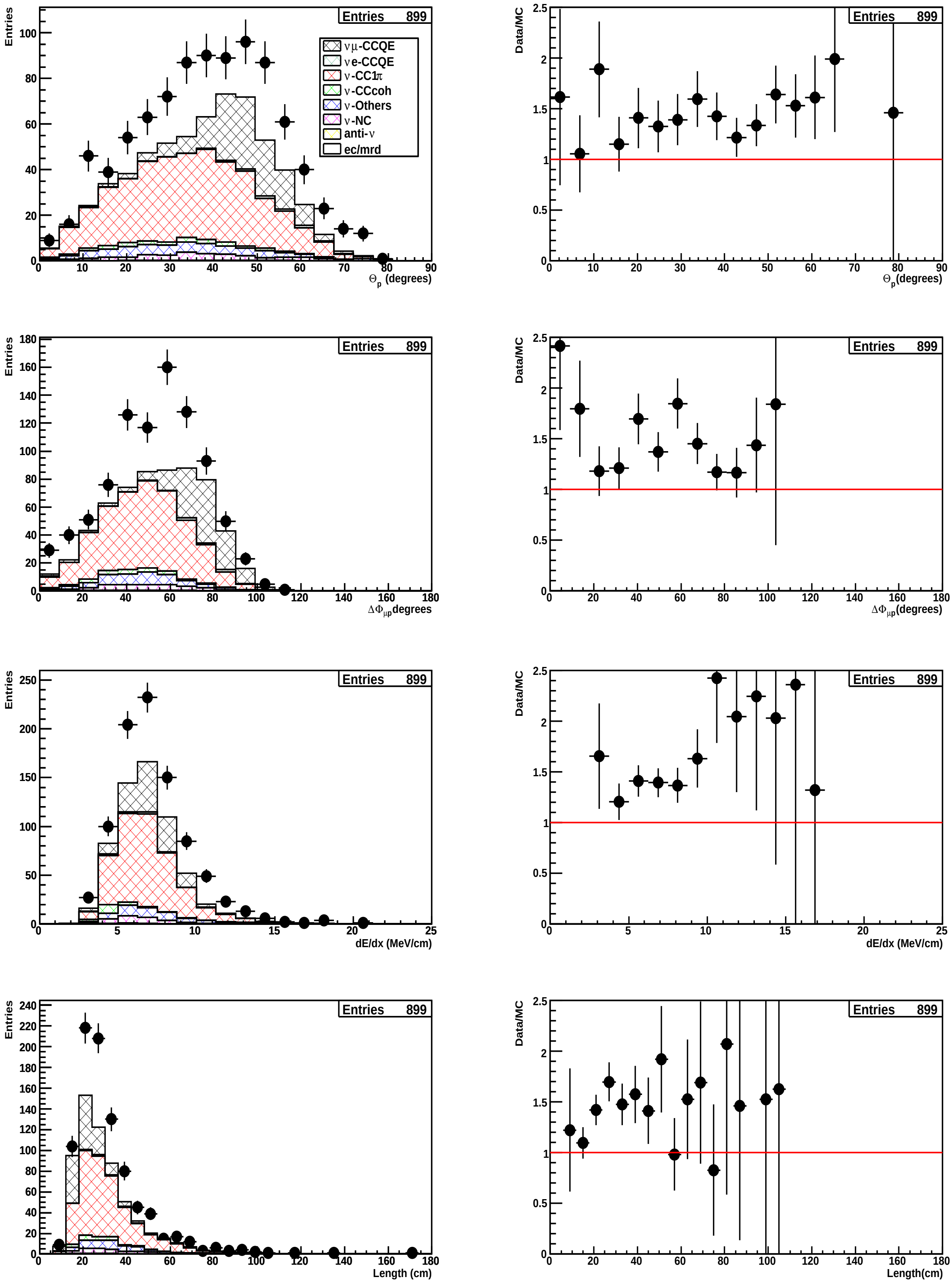

Figure 8.22: Second track kinematics distributions corresponding to the data excess sample (see text for details). MC is normalized to CC-inclusive.

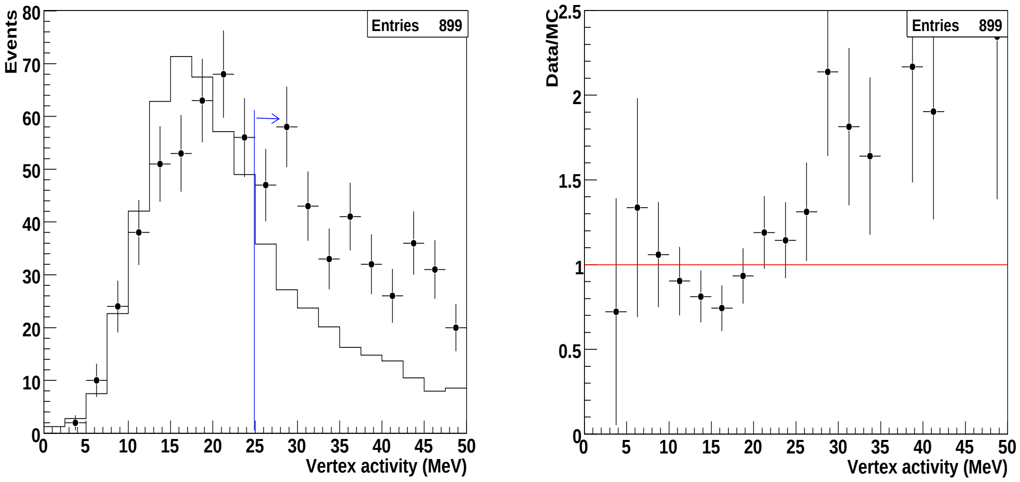

Figure 8.23: Vertex activity corresponding to the data excess sample (see text for details). MC is normalized to CC-inclusive sample.

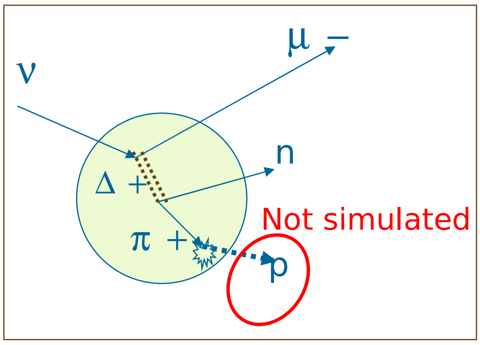

Figure 8.24: Picture of a CC resonance interaction with the pion re-interacting inside of the nucleus. The secondary produced particles are not simulated in NEUT.

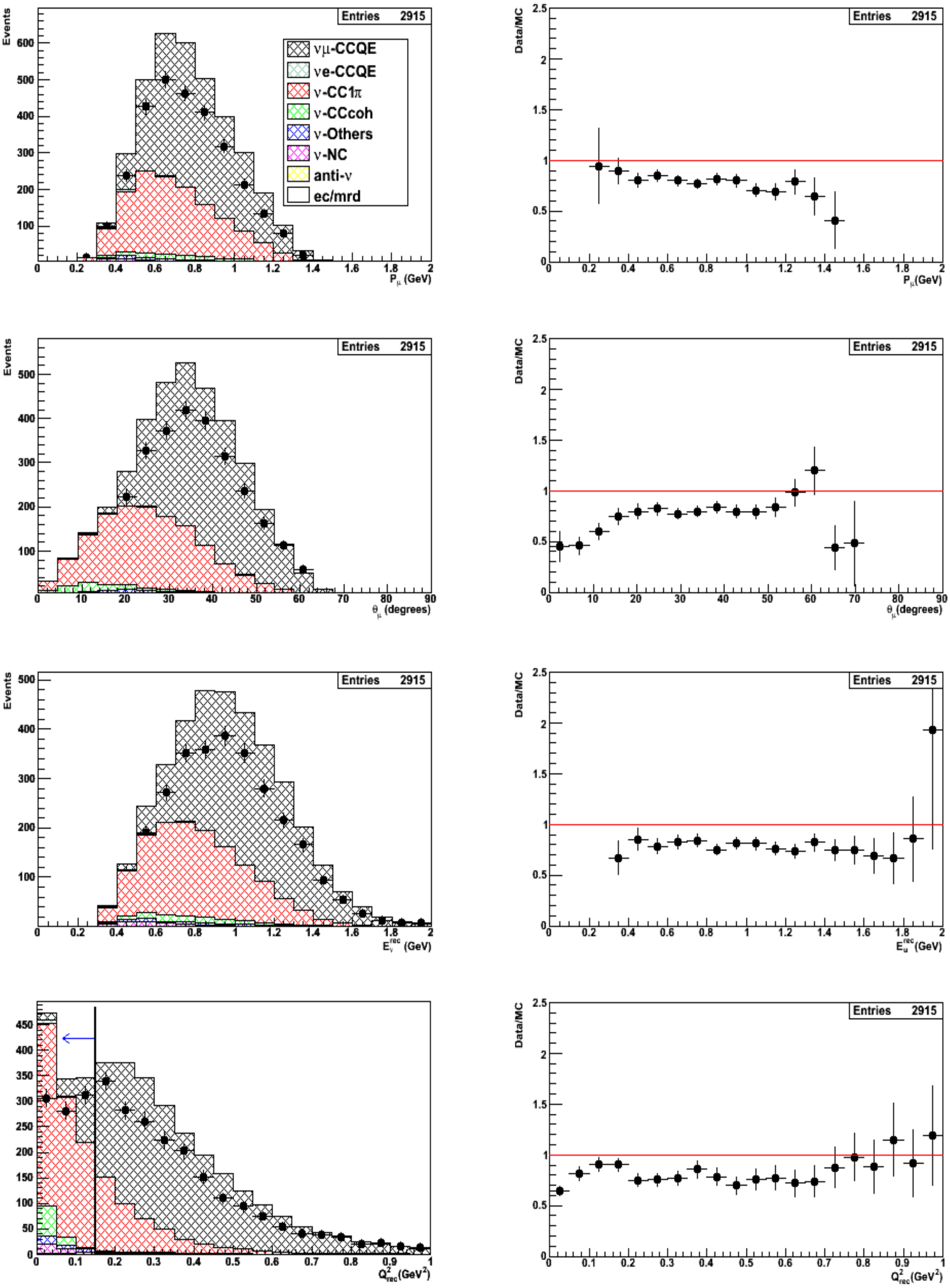

Figure 8.25: The 2-track QE enriched sample kinematic distributions with MC generated using NUANCE. MC is normalized to CC-inclusive sample.

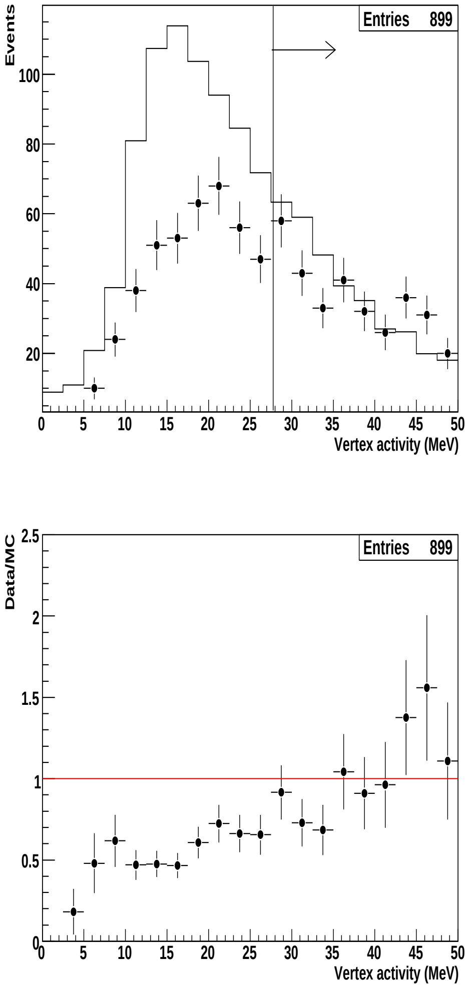

Figure 8.26: Vertex activity distribution for the 2-track QE enriched sample for events with $Q^2 < 0.15 GeV^2$. Data is compared with the NUANCE MC, normalized to CC-inclusive sample.

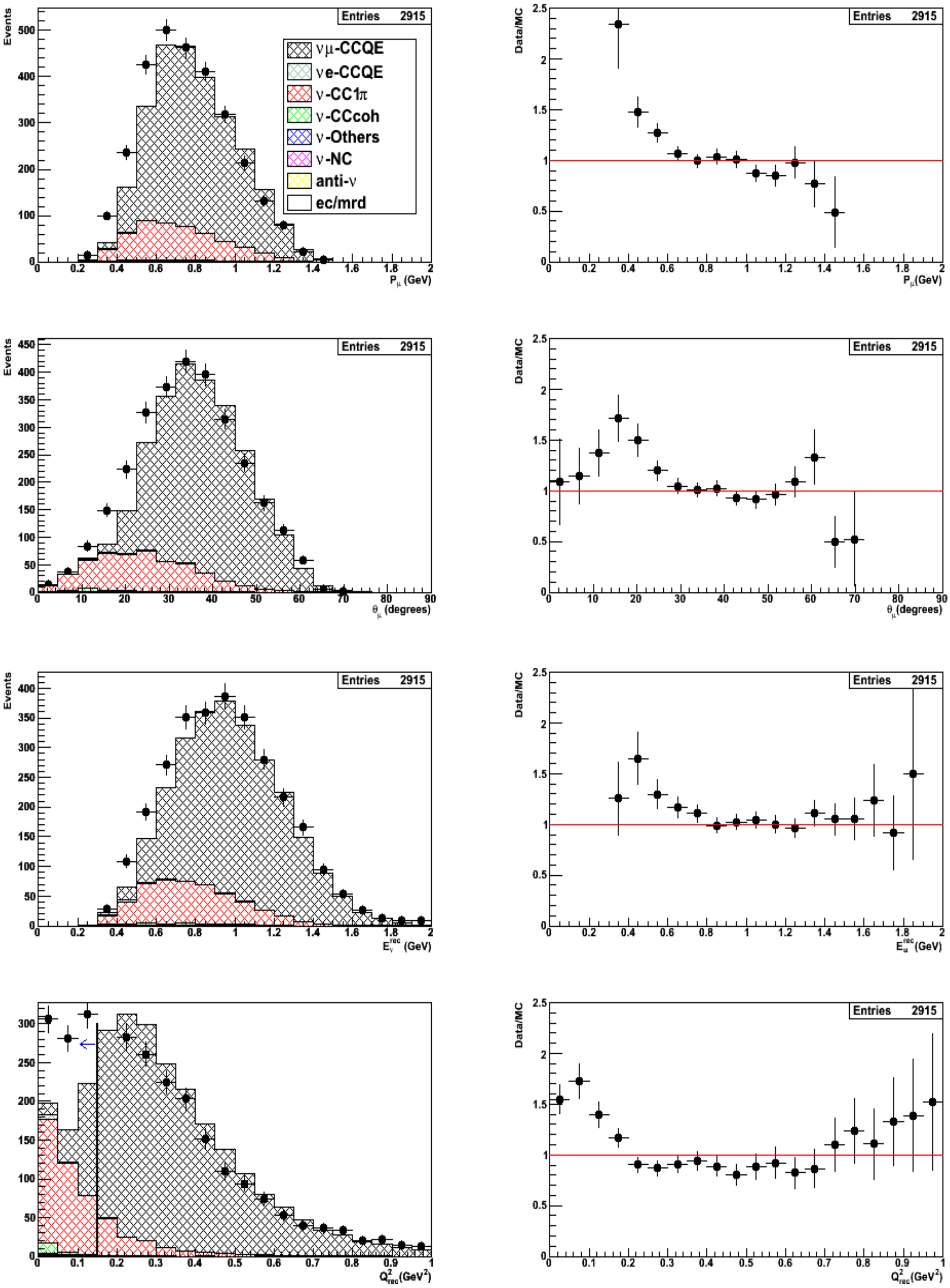

Figure 8.27: 2-track QE enriched sample kinematic distributions using NUANCE generator after subtracting the events described in the missing MC effect. MC is normalized to CC-inclusive sample.

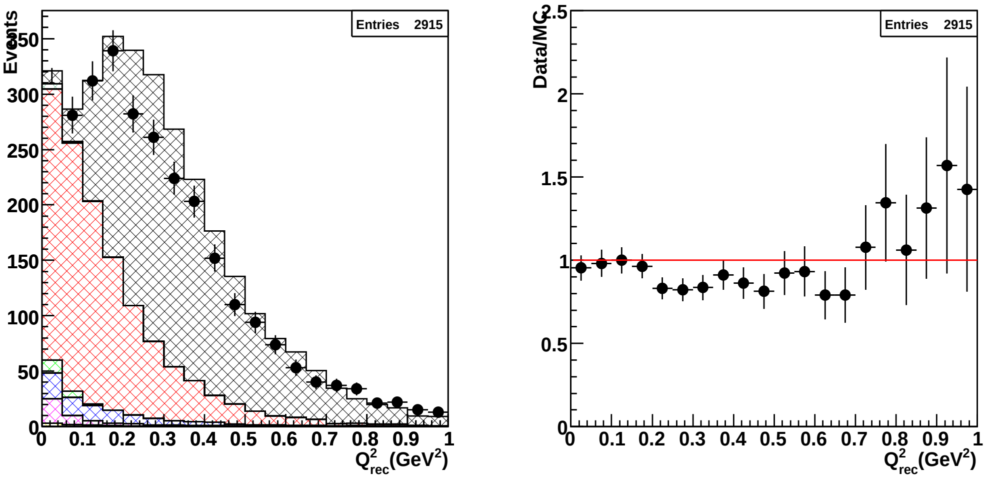

Figure 8.28: Q^2 distribution for the 2-track QE enriched sample using the modified NEUT. MC is normalized to the CC-inclusive sample.

Chapter 9

Measurement of the absolute CCQE cross section ($\sigma_{\nu_\mu}(E_\nu)$)

This chapter presents a fit technique developed to determine the CCQE absolute cross section as a function of the neutrino energy. Different fit checks to evaluate the robustness of the fit are described in this chapter.

9.1 Introduction

The absolute CCQE cross section has been determined by extracting the information from a data/MC comparison,

$$N_{DATA} = \mathbf{a} \times N_{MC} \times \left(\frac{POT_{data}}{POT_{MC}} \right), \tag{9.1}$$

where **a** represents the difference between data and MC. Here the MC has been normalized to the number of proton on target from data, expressed in the normalization factor (POT_{data}/POT_{MC}). The main interest of data/MC comparison is to extract the true neutrino energy variations. For such a reason, the parameter **a** becomes a function of the E_ν^{true}, $\mathbf{a} = \mathbf{a}(E_\nu^{true})$. A data/MC fit has been designed to obtain the information contained in the **a** parameters(explained in the next section).

The equation (9.1) can be expressed in terms of the flux (ϕ) and the cross section (σ) as follows:

$$\phi^{DATA} \times \sigma^{DATA}(E_\nu^{true}) = \mathbf{a}(E_\nu^{true}) \times \phi^{MC} \times \sigma^{MC}(E_\nu^{true}), \tag{9.2}$$

where the normalization factor has been absorbed in the parameter **a**. Since the flux is assumed to be well predicted[59], although flux variations will be treated as systematic errors, the equation (9.2) can be simplified as follows:

$$\sigma^{DATA}(E_\nu^{true}) = \mathbf{a}(E_\nu^{true}) \times \sigma^{MC}(E_\nu^{true}), \tag{9.3}$$

where **a** represents basically the variations on the cross section. Therefore, the cross section from data can be expressed, in each neutrino energy bin, as the predicted cross section modified by a factor **a**.

9.2 Fit Method

A fit method has been implemented to extract the true neutrino energy data/MC variations from the quasi-elastic events. The fit uses three samples, the 1-track and the 2-track QE and nonQE samples. Although the CCQE signal is concentrated in the first two samples, the last one is included to provide additional background information to the fit. These three samples are treated independently within the fit, such that, the total minimization function, described later, is built up as the sum of the minimization functions of each sample. In that way, the 1-track sample provides the largest statistics and the QE and nonQE enriched samples allow a better control of the signal and the background during the fit process.

9.2.1 MC templates

To perform the fit, the MC is divided in several templates which contain the variables to be fitted. The MC template is built up with observable variables corresponding to the reconstructed muon momentum (p^μ) and reconstructed muon angle (θ^μ). The MC is broken up in QE (signal) and nonQE (background) components. The QE component is divided, at the same time, in true energy bins. Mathematically, the MC can be written as follows:

$$N_{ij}^{MC} = \sum_k N^{QE}(p_i^\mu, \theta_j^\mu; E_{\nu,k}^{true}) + N^{nonQE}(p_i^\mu, \theta_j^\mu). \tag{9.4}$$

The figures 9.2, 9.3 and 9.4 show the (p^{μ}, θ^{μ}) MC templates corresponding to the QE components for the 1-track and 2-track QE and nonQE samples, respectively. The true neutrino energy has been divided in 10 bins, from 0 to 2 GeV.

The (p^{μ}, θ^{μ}) MC templates for the nonQE component are shown in the figure 9.5. In all the cases, the Monte Carlo templates are normalized to the number of protons on target (POT) generated in data. This normalization is necessary to evaluate an absolute neutrino cross section. The appendix E shows the kinematic distributions for the sample selection with POT normalization.

Since the fit compares MC templates with data, the data is represented by (p^{μ}, θ^{μ}) structures as well, see figure 9.1.

9.2.2 Minimization function

The data/MC fit works with a binned likelihood function, assuming that observed events N_{ij}^{obs}, with expected values N_{ij}^{exp}, follows a Poisson distribution. The likelihood function is maximized based on the contents of the bins (i and j label bins). This is equivalent to maximize the likelihood ratio[76]:

$$\lambda = \frac{P\left(N_{i,j}^{obs}, N_{i,j}^{exp}\right)}{P\left(N_{i,j}^{obs}, N_{i,j}^{obs}\right)}, \tag{9.5}$$

where P(n,ν) represents the Poisson probability to find n events with expected value ν,

$$P(n, \nu) = \frac{\nu^{n} e^{-\nu}}{n!}. \tag{9.6}$$

The maximization of the equation (9.5) is equivalent to the minimization of the following quantity:

$$F_{min} = -2ln\lambda = 2 \times \sum_{ij} \left[N_{ij}^{exp} - N_{ij}^{obs} + N_{ij}^{obs} \times ln\left(\frac{N_{ij}^{exp}}{N_{ij}^{obs}}\right)\right], \tag{9.7}$$

where the Poisson probability equation (9.6) has been included and N_{ij}^{exp} and N_{ij}^{obs} correspond to the number of MC and data events represented in bins of reconstructed muon momentum (p_{i}^{μ}) and reconstructed muon angle (θ_{j}^{μ}).

9.2.3 Fit parameters definition

The fit method introduces free parameters to extract the data/MC differences. The free parameters have been added to the MC, using the equation (9.4), in the following way:

$$N_{ij}^{exp} = F_N \left[\sum_{k}^{n=10} a_k N_{ij}^{QE,k}, + a_{bck} N_{ij}^{nonQE} \right] \tag{9.8}$$

A total of twelve free parameters defines the equation (9.8). The a_{bck} is a global parameter which delivers information about the non-QE contamination. Ten of them are neutrino energy dependent parameters ($a_1, a_2....., a_{10}$). Each of a_k is associated to a different true neutrino energy bin and returns the true neutrino energy data/MC variation for the QE components. These parameters contain the essential information to evaluate the CCQE absolute cross section (see eq. (9.3)).

The a_k corresponding to the energy bin [0.8,1] GeV has been fixed to the unity. Such a constraint allows that a_k's report neutrino energy shape only variations. The F_N times each a_k gives us the absolute variation between data and MC at the energy bin.

The a_0 parameter is fixed to the unity as well because no data nor MC information are present at the energy region below 0.2 GeV, see figure 9.6.

An additional parameter (α) is included to correct the migration effect present in the MC, as was described in section 8.6. This parameter evaluates the fraction of 1-track nonQE events that should be reconstructed as 2-track nonQE events in the 2-track QE enriched sample. Therefore, α is inserted on the following way:

$$N_{ij,1-track}^{nonQE} = (1. - \alpha) \times N_{ij,1-track}^{nonQE}, \tag{9.9}$$

$$N_{ij,2-track\ QE}^{nonQE} = N_{ij,2-track\ QE}^{nonQE} + \alpha \times N_{ij,1-track}^{nonQE}. \tag{9.10}$$

Finally, only eleven parameters are free within the fit (eight a_k's and the a_{bck}, F_N and α) and all of them are initially set to the unity except α that is set to zero.

The absolute CCQE cross section determined by the data can then be written, using equation (9.3), in the following way:

$$\boxed{\sigma_{\nu_\mu}(E_\nu^k) = F_N \times a_k \times \sigma_{\nu_\mu}^{pred}(E_\nu^k)} \tag{9.11}$$

where the index k represents the true neutrino energy bin and $\sigma_{\nu_\mu}^{pred}(E_\nu^k)$ is the value of the absolute cross section predicted by NEUT. Once again, one can observe the role of the a_k parameters, re-weighting the predicted cross section for each neutrino energy bin.

9.3 Goodness of the fit

When the fit process is running, the free parameters varies to achieve a value which minimizes the likelihood function (F_{min}). Figures 9.7 and 9.8 show the scanning of the convergence process for each fit parameter. In all the cases, a smooth variation around the minimum value is observed, without additional local minima. The F_{min}/dof quantity takes values of 2.47 and 1.7 before and after the fit, respectively, with an improvement of around 30%.

Another check was implemented to evaluate the robustness of the fit method. The check is based on running the fit using MC instead of data (”fake data”). The results show a convergence of the fit parameters around the unity (see figure 9.9), except at high energies due to low statistics. Details of the calculations can be found in appendix D.

9.4 Results

The table 9.1 shows the values of the free parameters after the fit. The α factor takes a value of 0.03, which indicates that a fraction around 3% of the nonQE 1-track events should migrate to the 2-track QE enriched sample. The a_{bck} value points out that the background in MC is under-estimated in around 37%. However, one must be careful because of the strong anti-correlation of this parameter with the Fn factor (around 88%), as figure 9.10 shows and in general the correlation of each parameter with respect to the rest of them (the global correlation), shown in table 9.2.

The absolute ν_μ-CCQE cross section per nucleon is then extracted using fit parameters values in the equation (9.11). Figure 9.11 shows the absolute ν_μ-CCQE cross section per nucleon, with only statistic errors, as a function of the neutrino energy (tabulated values in 9.3). The agreement between data and the NEUT predictions, just based on statistical errors, is pretty good on the energy region

fit parameter	value	stat. error
a_0	1.0	fixed
a_1	1.	2.0
a_2	2.73	0.12
a_3	1.01	0.06
a_4	1.	fixed
a_5	1.09	0.07
a_6	1.01	0.07
a_7	1.04	0.14
a_8	0.6	0.3
a_9	2.6	0.6
a_{bck}	1.37	0.07
F_N	1.02	0.04
α	0.030	0.007

Table 9.1: Values of the free parameters after the fit.

between 0.6 and 1.6 GeV. In others energy regions, the data is compatible with predictions at only one sigma variation. The exception is present in the energy interval from 0.4 to 0.6 GeV. The evaluation of systematic errors will supply better understanding on this energy region.

9.5 Monte Carlo re-weighted

The robustness of the fit results can be checked again by comparing the kinematic distributions with the MC before and after the fit. The MC after the fit correspond to the MC where the events have been re-weighted with the fit parameters according to the equations (9.8) and (9.10). Figure 9.12 shows the kinematic distributions for the 1-track sample. The figure compares data with MC before and after the fit. The χ^2/ndf values are shown in table 9.4. In this case, the data/MC agreement has improved after the fit but not significatively, as shows χ^2/ndf values in table 9.4. The reason comes from the discrepancy in the muon angles, which is still present after weighting the events with the fit parameters. This effect will be analyzed and evaluated as a systematic in the following chapter.

A very good data/MC agreement is observed in the kinematics of the 2-track

fit parameter	E_ν-bin (GeV)	global correlation (%)
a_0	0.1	fixed
a_1	0.3	51.1
a_2	0.5	66.8
a_3	0.7	85.7
a_4	0.9	fixed
a_5	1.1	87.9
a_6	1.3	71.6
a_7	1.5	69.4
a_8	1.7	60.2
a_9	1.9	60.8
a_{bck}	-	96.4
F_N	-	98.2
α	-	52.4

Table 9.2: Global parameter correlation.

QE enriched sample, even the data excess problem at low Q2 region has been resolved using the MC after the fit. See χ^2/ndf values as well in table 9.4. Good agreement is observed in kinematics for the 2-track nonQE enriched sample (see 9.14), where the total amount of events is now compatible with the MC after the fit.

E_ν^{true} (GeV)	σ_ν^{CCQE} $10^{-38} cm^2/nucleon$	stat. err. $10^{-38} cm^2/nucleon$	rel. err. (%)
0.3	0.3	0.5	166
0.5	0.11	0.05	45
0.7	0.48	0.02	4.2
0.9	0.52	0.02	3.8
1.1	0.58	0.02	3.4
1.3	0.55	0.03	5.5
1.5	0.57	0.07	12.3
1.7	0.33	0.17	51.5
1.9	1.4	0.4	28.6

Table 9.3: Cross section values with statistical errors.

1-track sample

variable	ndf	χ^2_{before}	χ^2_{after}
P_μ	15	172.15	21.97
Θ_μ	17	317.40	264.37
E_ν^{rec}	18	212.14	101.39
Q^2_{rec}	20	356.94	280.08

2-track QE sample

variable	ndf	χ^2_{before}	χ^2_{after}
P_μ	13	82.25	13.38
Θ_μ	16	118.38	27.70
E_ν^{rec}	17	94.43	18.49
Q^2_{rec}	20	161.15	48.53

2-track nonQE sample

variable	ndf	χ^2_{before}	χ^2_{after}
P_μ	13	96.97	28.23
Θ_μ	16	88.28	21.40
E_ν^{rec}	18	94.28	23.63
Q^2_{rec}	20	96.15	35.48

Table 9.4: Table comparison of the χ^2 value before and after the fit.

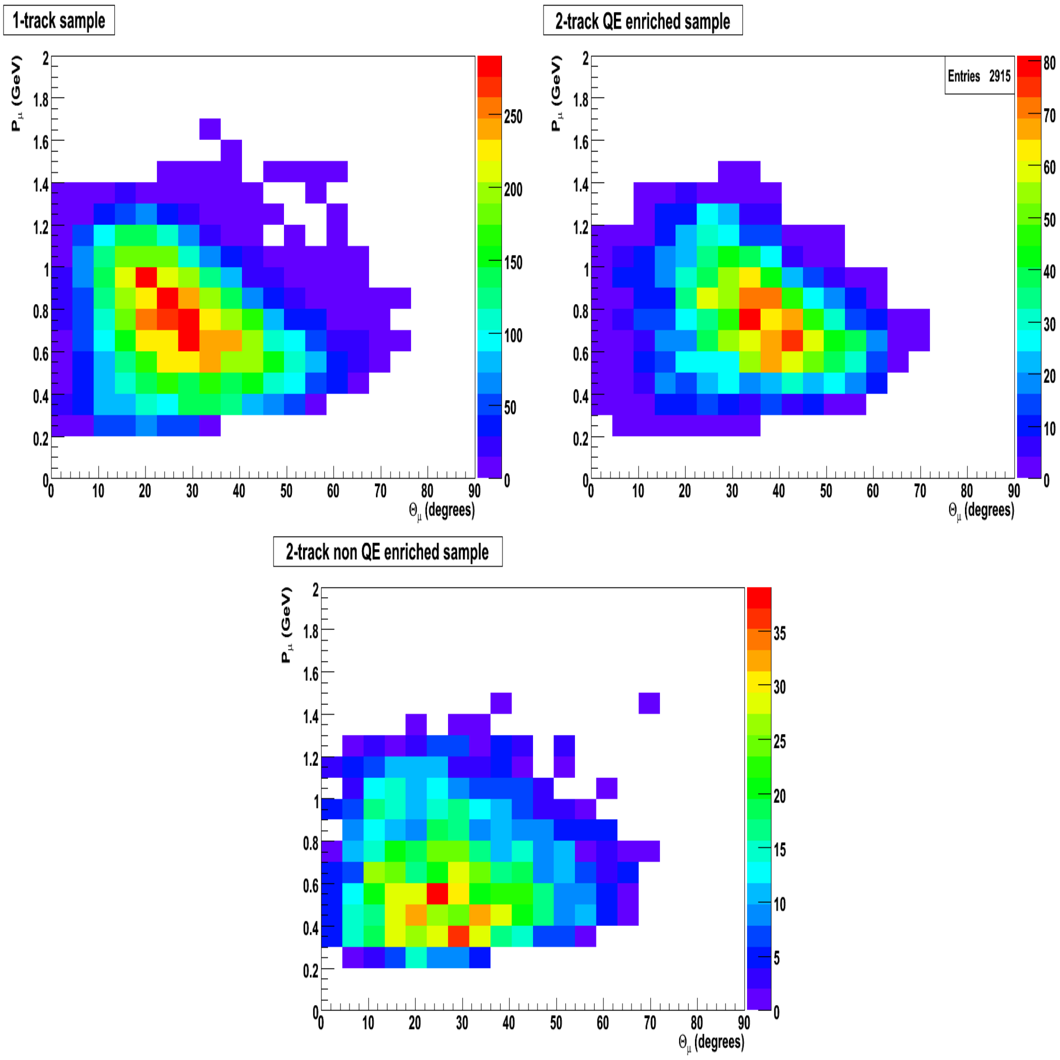

Figure 9.1: Data (P_μ, θ_μ) distributions for the 1 track and 2-track QE and nonQE samples.

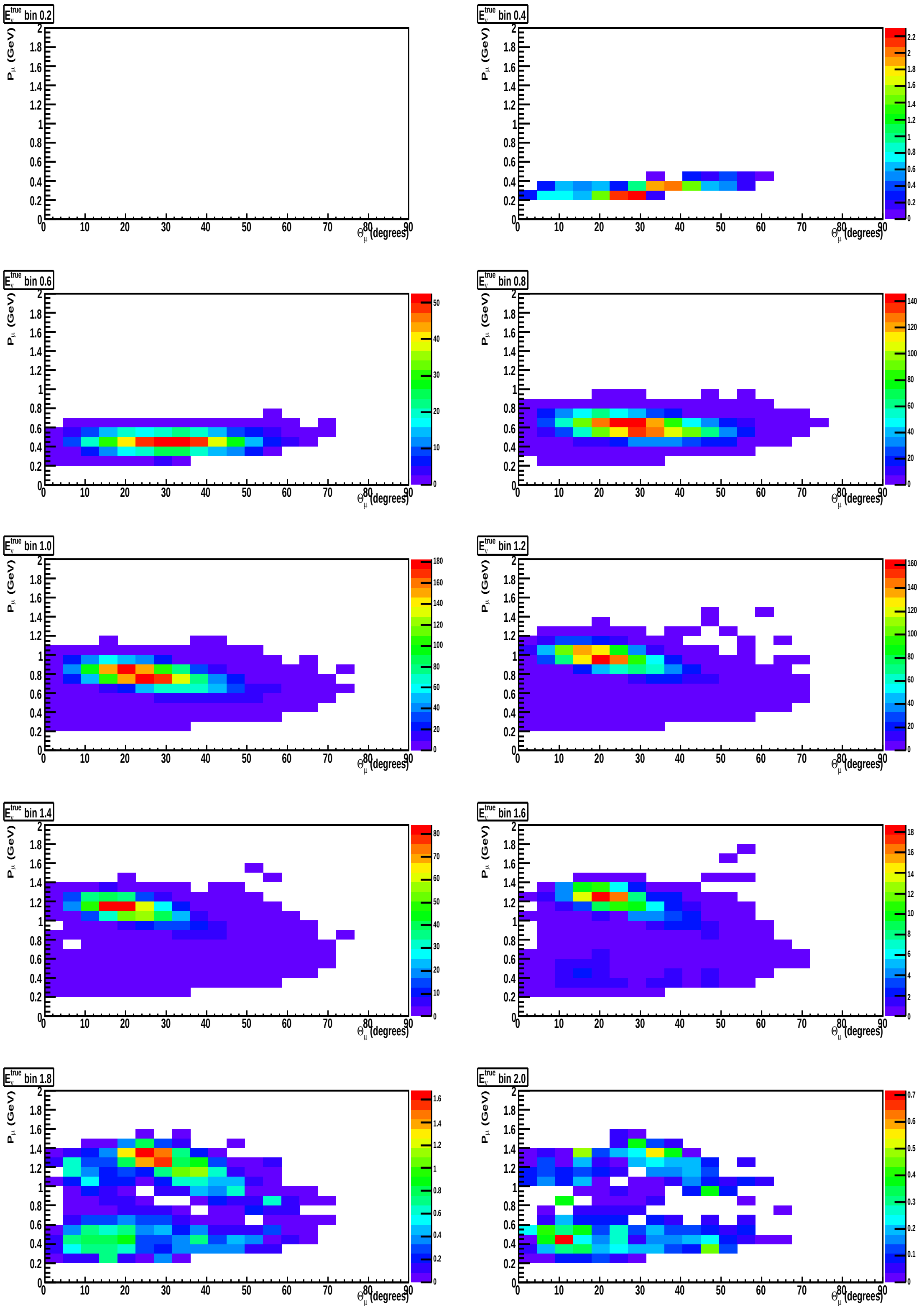

Figure 9.2: Monte Carlo (P_μ, θ_μ) distributions for the quasi-elastic component of the 1-track sample, divided in true neutrino energy bins, from 0-2 GeV. MC is normalized to POT.

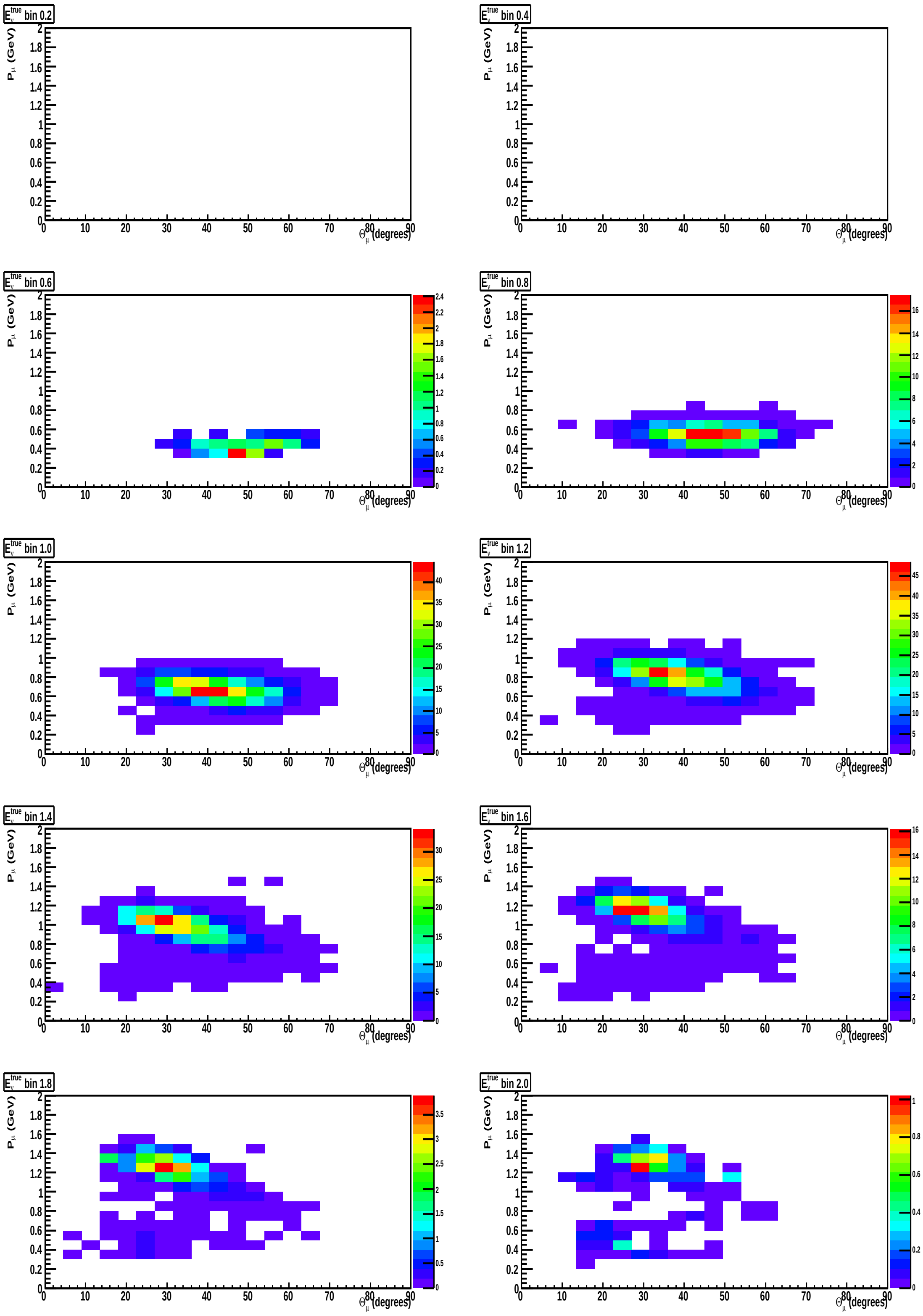

Figure 9.3: Monte Carlo (P_μ, θ_μ) distributions for the quasi-elastic component, divided in true neutrino energy bins and corresponding to the 2-track QE sample. MC normalized to POT.

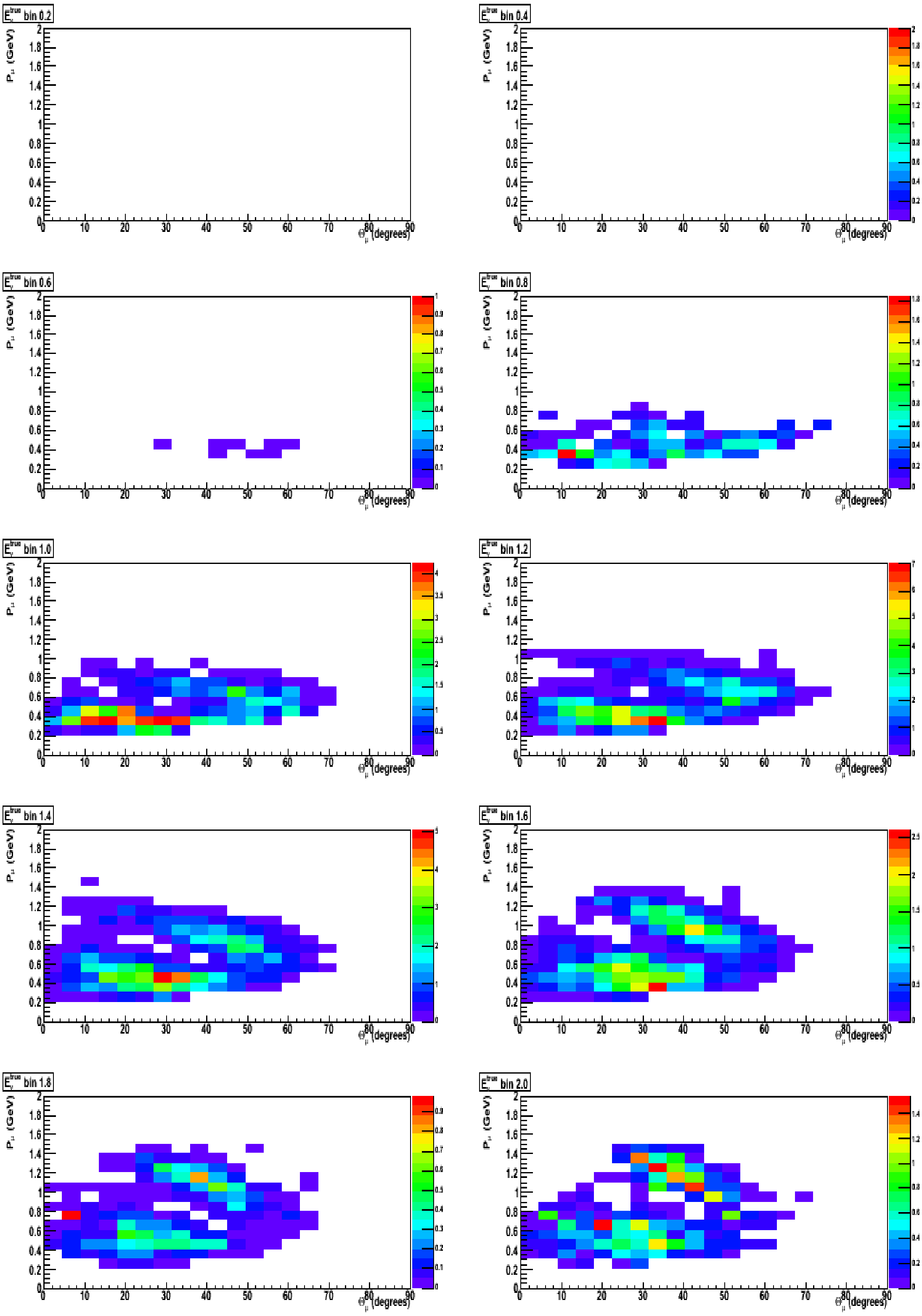

Figure 9.4: Monte Carlo (P_μ, θ_μ) distributions for the quasi-elastic component, divided in true neutrino energy bins and corresponding to the 2-track nonQE sample. MC normalized to POT.

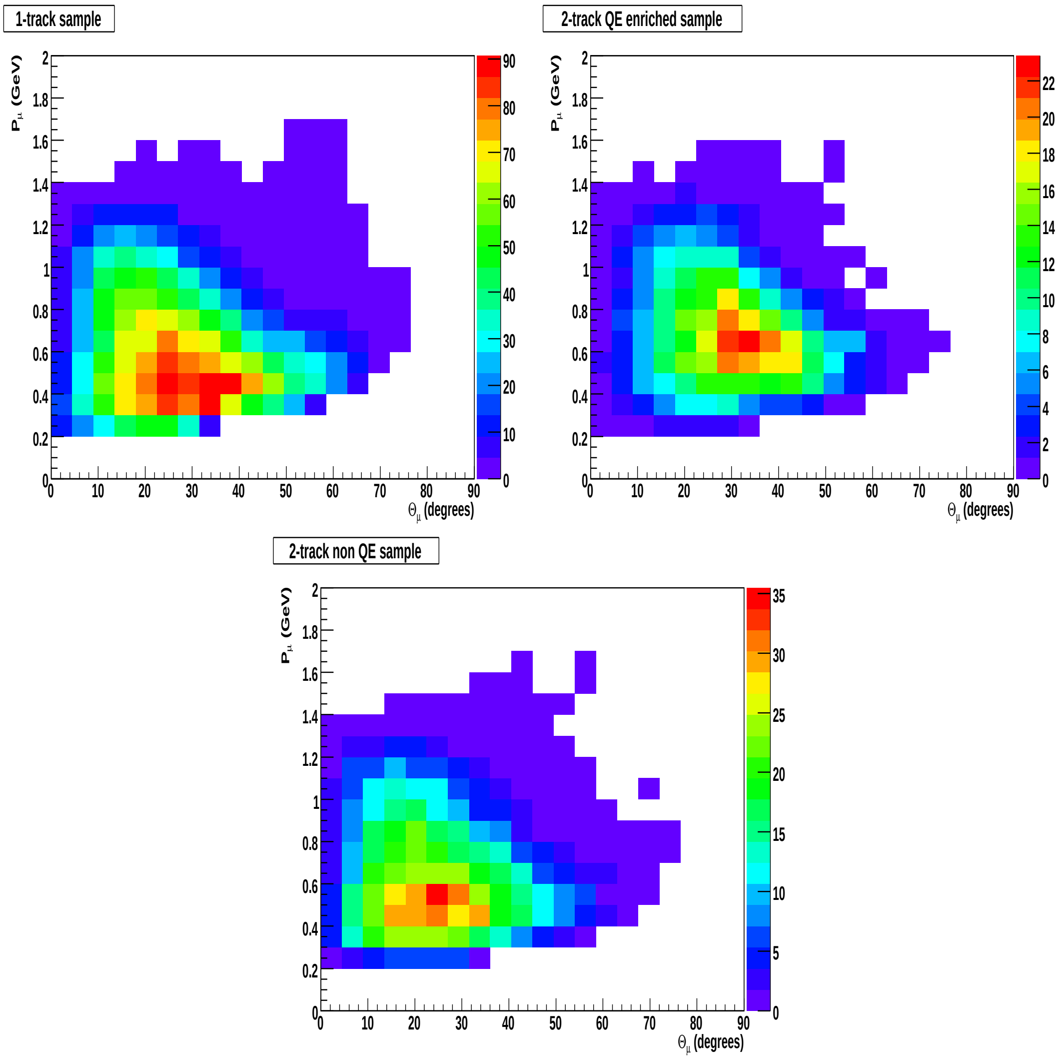

Figure 9.5: Monte Carlo (P_μ, θ_μ) distributions corresponding to non quasi-elastic events. From left to right, the 1 track, the 2 track QE and 2 track nonQE samples. MC is normalized to POT.

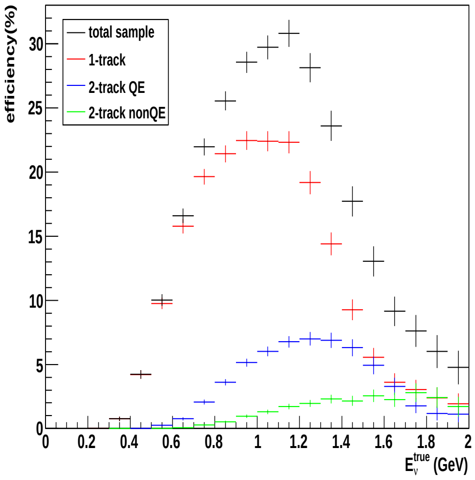

Figure 9.6: CCQE efficiency as a function of the true neutrino energy for the 1-track, 2-track QE and nonQE samples.

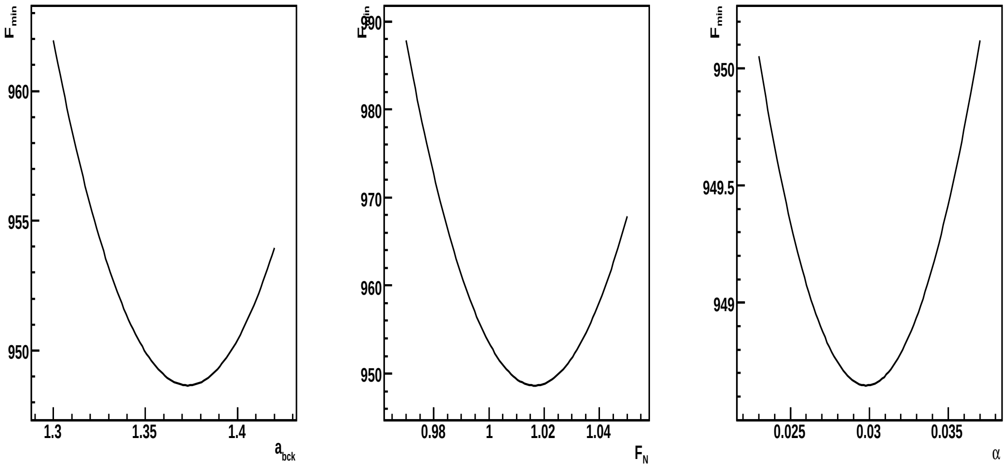

Figure 9.7: Scan of fit parameter values, within one sigma variation, versus the minimization function.

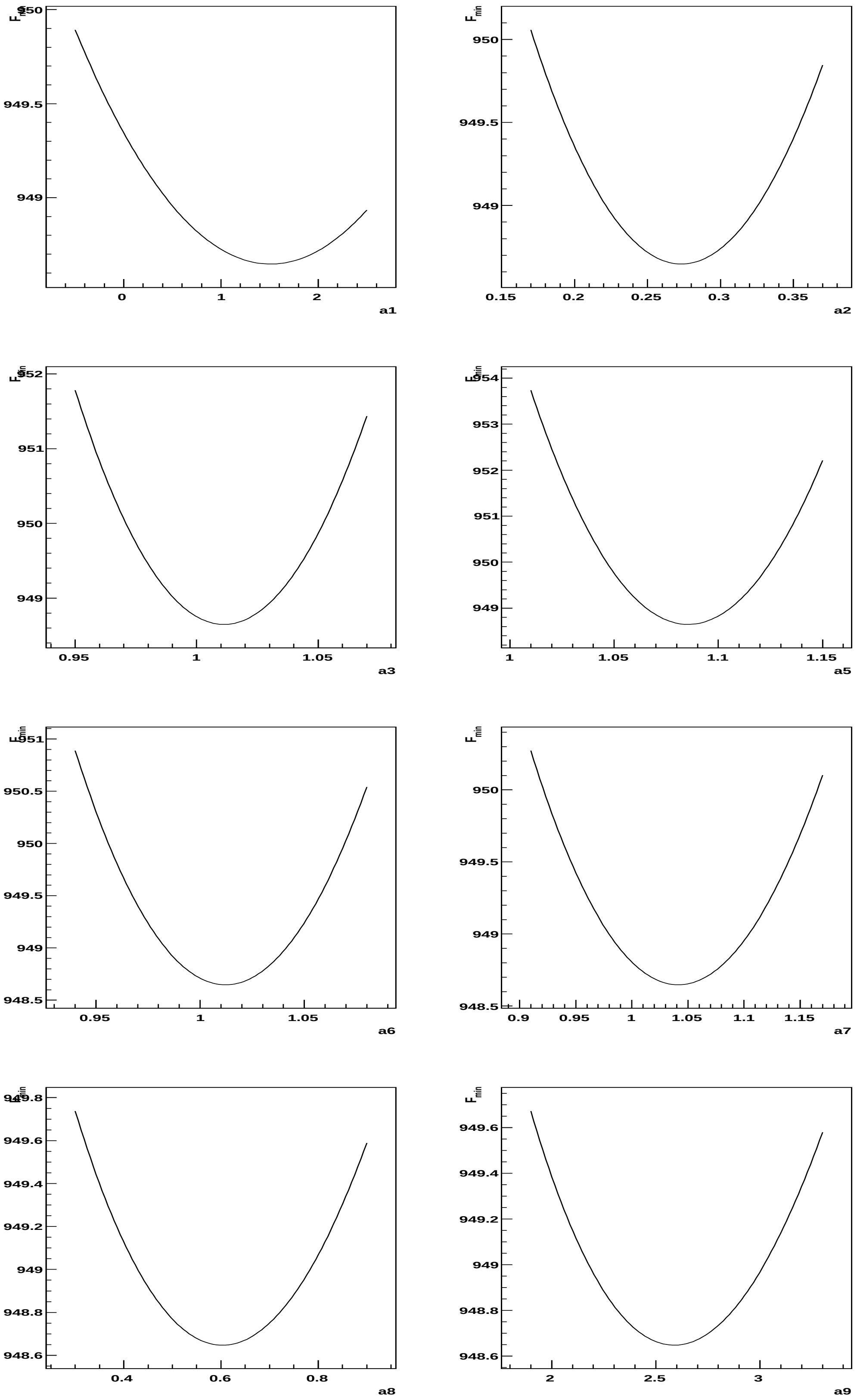

Figure 9.8: Scan of the energy dependent fit parameter values, within one sigma variation, versus the minimization function.

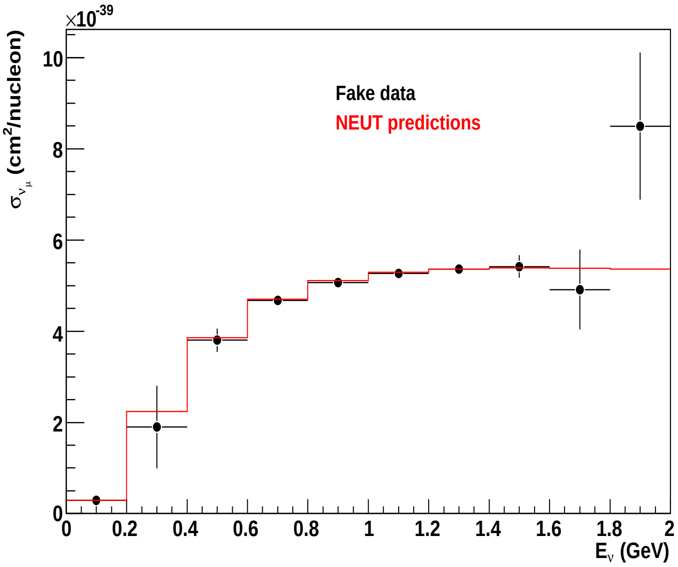

Figure 9.9: ν_μ-CCQE absolute cross section per nucleon as a function of the neutrino energy using fake data. Red line corresponds to the NEUT predictions and black dots to fake data with statistic errors added.

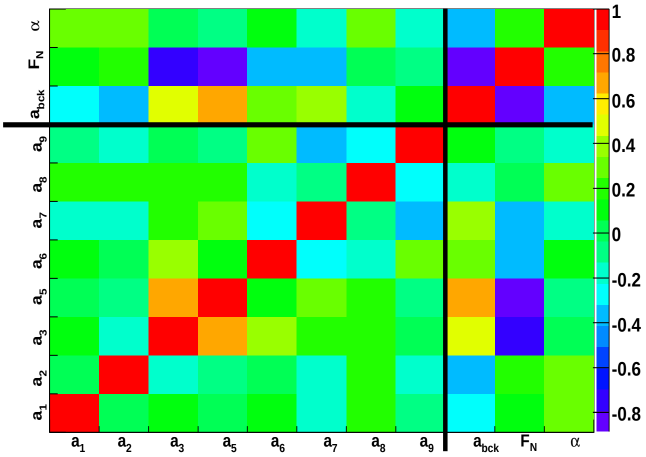

Figure 9.10: Correlation matrix for fit parameters.

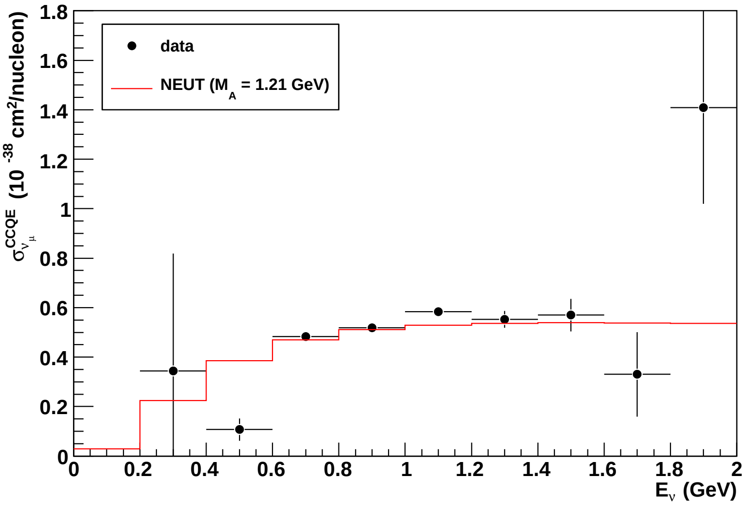

Figure 9.11: CCQE absolute neutrino cross section per nucleon as function of the neutrino energy. Only statistical errors shown.

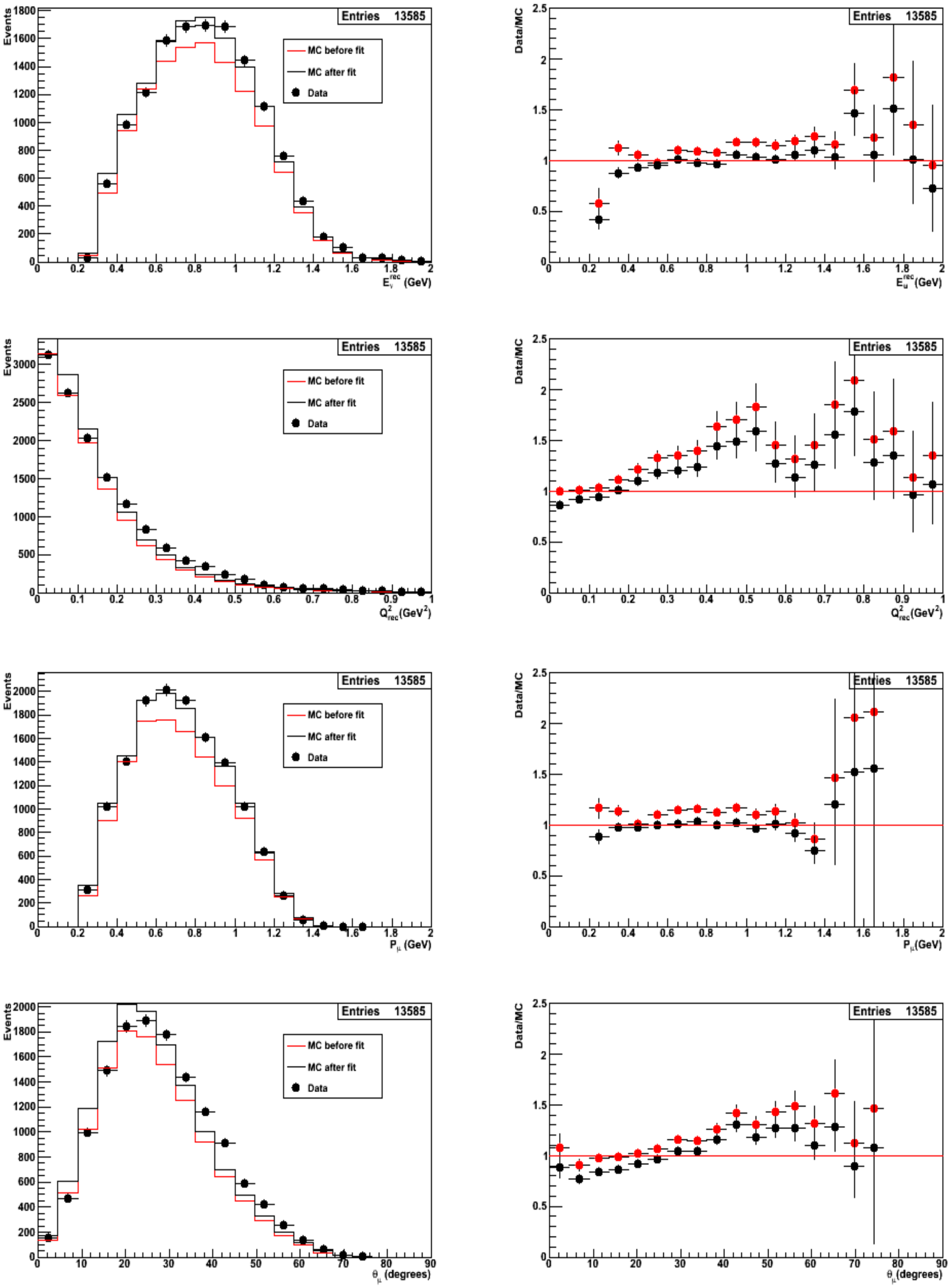

Figure 9.12: 1-track kinematic distributions with the MC before (red line) and after (black line) the re-weighting. MC is POT normalized.

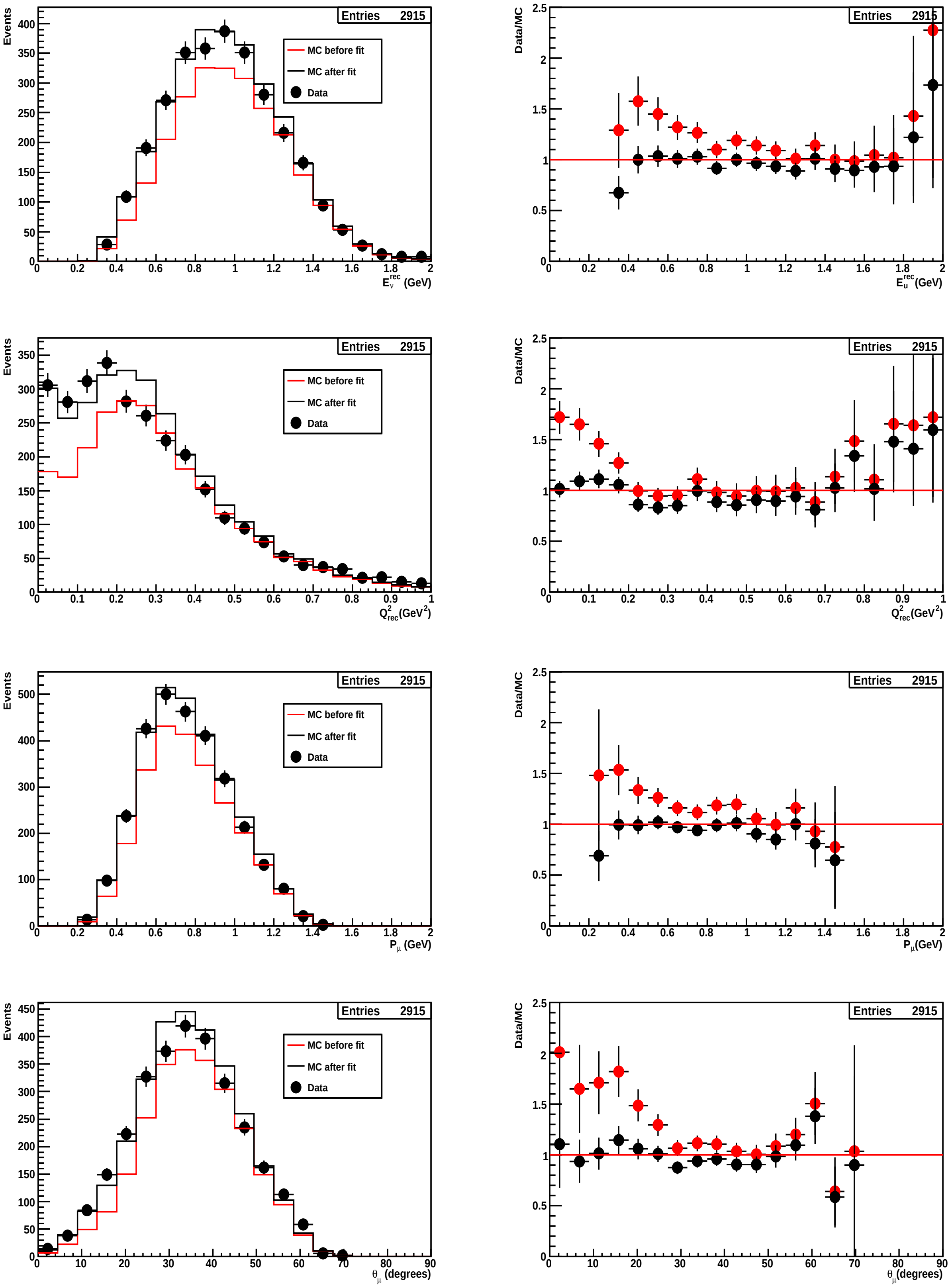

Figure 9.13: 2-track QE kinematic distributions with the MC before (red line) and after (black line) the re-weighting. MC is POT normalized.

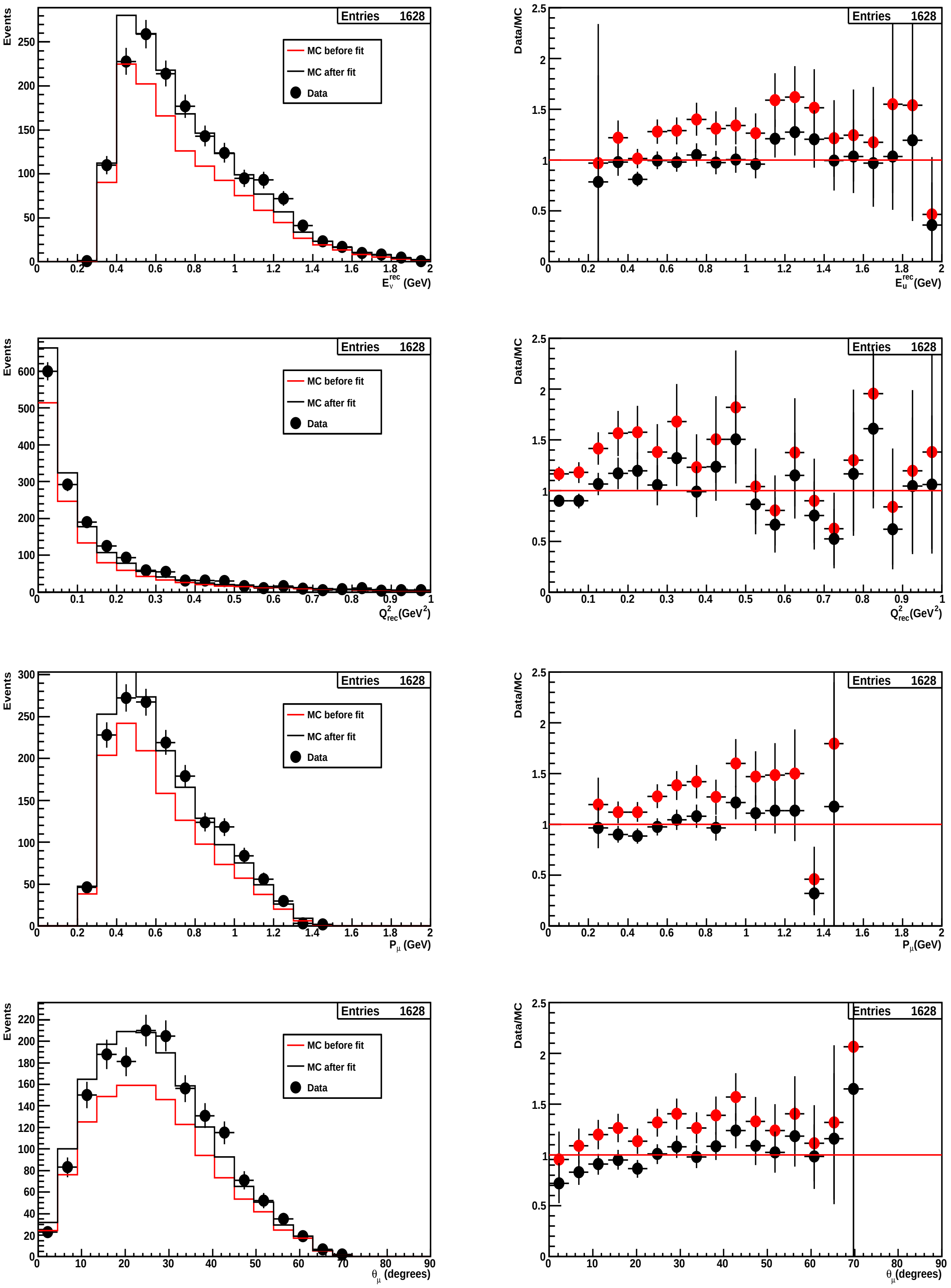

Figure 9.14: 2-track nonQE kinematic distributions with the MC before (red line) and after (black line) re-weighting. MC is POT normalized.

Chapter 10

Systematic Errors

This chapter describes the systematic sources affecting the measurement of the absolute CCQE neutrino cross section. The sources are divided in five categories: the neutrino beam, the detector response, the neutrino interaction model, the nuclear effects and the muon angle discrepancies. This chapter analyze each one of these systematic sources.

10.1 Technical description

The systematic errors have been evaluated through of Monte Carlo systematic variations. Two different techniques have been adopted to reproduce those variations. The first one is based on the MC event re-weighting and the second is just the MC production with the corresponding parameter variation. Uncertainties associated to detector response have been evaluated with the late technique.

The weight is a factor associated to each event and represents the interaction probability for a neutrino passing through the SciBar detector. This probability is evaluated taken into account different factors like the neutrino mean path, the detector density and the cross section. Technically, this weight is used when histograms has to be fill up, like the (p_μ, θ_μ) MC templates. In the MC weighting technique, an additional factor is added to the nominal event weight in order to get the MC systematic variation.

The factor that introduces the systematic variation is calculated in a different way depending of the systematic source. However, the most general form is to assign an event weight that corresponds with the ratio between the varied quantity and the quantity at nominal values. The flux uncertainties, for instance, have been evaluated using this technique. Here, cross section ratios ($\sigma^{varied}/\sigma^{nominal}$) determine the event weight associated to the uncertainties in the π-production, one of the uncertainty sources of the neutrino beam. Systematic uncertainties related to neutrino interaction model and nuclear model have been evaluated with this technique.

After applying the systematic variation to the MC, via event re-weighting or via MC generation, (p_μ, θ_μ) templates with the MC variation are re-generated. The new MC templates are fitted to the data, such that, the resulting cross section contains the systematic variation (σ^{var}). Therefore, the systematic error is evaluated as the difference between the σ^{var} and the cross section obtained using nominal values (σ^{Nom}). The systematics associated to the a_{bck}, F_N and α parameters are calculated in the same way.

10.2 The Monte Carlo statistics

The MC statistics has been included as a systematic uncertainty because of the effect in the fit technique. The systematic associated to MC statistics is evaluated using the fit technique. Here, the fit does not compare data/MC but MC/MC. The statistical errors of the resultant cross section represents the systematics associated to the MC statistics (see figure 10.1).

The table 10.1 shows the relative errors associated to the MC statistics. Large errors are present at low and high energies, as expected.

Small variations of the MC templates, i.e. variations of the (p_μ, θ_μ) bin content, can affect the data/MC fit. When the (p_μ, θ_μ) template is modified, the fit parameters fluctuates to a different value, as one expects. However, the fluctuation takes large values when the fit works with low MC statistics, as figure 10.2 shows. This effect is in part due to the correlation between parameters, small variations in parameters with high statistics can be translated in large variations to fit parameters with low statistics.

The evaluation of a systematic uncertainty is based on modifications of the (p_μ, θ_μ) templates. Therefore, large parameter fluctuations around low and high neutrino energies are expected because of the low MC statistics and parameter

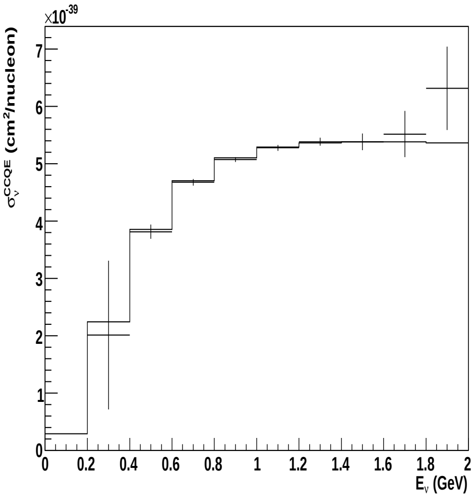

Figure 10.1: CCQE absolute cross section obtained from a MC versus MC fit, instead of a data/MC fit. The errors shown represent the systematic associated to the MC statistics.

correlation at these energy regions.

10.3 Neutrino beam

The prediction of the neutrino flux has uncertainties derivated from the hadronic interactions of the protons with the Beryllium target, the prediction of $\pi^\pm/K^\pm$ production in p-Be interactions and the horn magnetic field model, see details in section 5.1.

Uncertainties in the p-Be interactions have been considered by varying the components of the hadronic cross sections (elastic and quasi-elastic scattering). This uncertainties produces a flux variation of $\sim 2.8\%$.

The prediction of $\pi^\pm/K^\pm$ production is based on the Sanford-Wang and the Feynman scaling models (see section 5.1). The uncertainties in the prediction are extracted from the covariance matrix produced by fitted parameters (HARP results[45]) used in the parameterization models. This process represents the dominant uncertainty source in the neutrino beam, producing a variation in the flux of $\sim 14.7\%$. Much of the uncertainty arises not from the accuracy of the

E_{ν}^{bin} (GeV)	absolute err. ($cm^2/nucleon$) ($\times 10^{-38}$)	relative err. (%)
0.3	0.13	43.3
0.5	0.012	10.9
0.7	0.005	1.3
0.9	0.004	0.8
1.1	0.005	0.9
1.3	0.007	1.3
1.5	0.014	2.5
1.7	0.04	12.1
1.9	0.07	5.0
a_{bck}	0.011	0.8
F_N	0.0010	0.9
α	<0.0001	<0.0001

Table 10.1: Systematic uncertainties associated to the Monte Carlo statistics.

measurements but from the parameterization models used to predict the cross sections.

The electric current supplied to the horn corresponds to 170 kA. This current flows through the horn surface, yielding a strong magnetic field which focuses the meson production. However, some other charge can penetrates into the inner conductor, modifying the magnetic field. This effect, so-called "skin effect", together with the horn current resolution ($\pm 1kA$) have been evaluated as beam systematic sources. The horn magnetic field model uncertainties produce a variation in the neutrino flux of $\sim$ 2.2%. Technical details of uncertainty calculations can be found in ref. [59].

Figure 10.3 shows the ν_{μ} flux for the SciBooNE detector. The filled squares represents the uncertainties from beam systematics. The triangle points indicates the default MC used in this analysis. The observed error asymmetry is consequence of the complex parameterization of the Sanford-Wang and the Feynman scaling models. The high energy flux errors comes from uncertainties in the Kaon decays. The beam systematics represents around 15% of the flux variation, dominated by the π-production uncertainties.

Table 10.2 shows the systematic errors of the cross section associated to flux

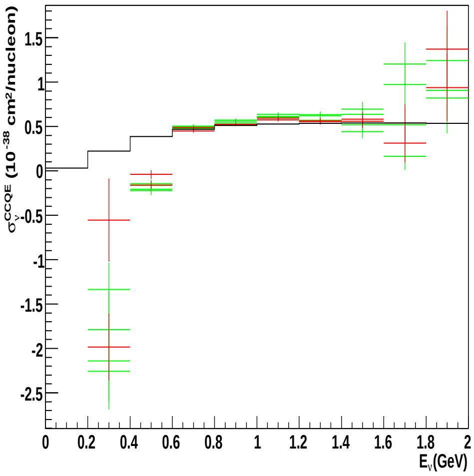

Figure 10.2: CCQE absolute cross section using MC's with different statistics. Green dots use MC with 1/4 the nominal MC statistics. Red dots use MC with 1/2 the nominal MC statistics. Line corresponds with the NEUT predictions.

variations. Errors for a_{bck}, F_N and α are also shown. The intermediate energies (0.6 to 1.6 GeV) present a mean error around 12.4%. The low statistics at low energies and the high flux systematic errors at high energies explain the large errors observed in these energy regions.

Figure 10.4 shows the correlation error matrix associated to the cross section for flux variations. A high anti-correlation is observed between high and low energies. This effect is related to the CC resonant interactions. At high true energies, the CCπ events have associated low reconstructed muon momentum and high scatter angle, populating the (p_μ, θ_μ) regions characteristic from CCQE interactions at low energies. This effect relates the low and high energies.

10.4 Detector response

Uncertainties related to the detector response have been considered. For the SciBar detector, the following uncertainties have been estimated: PMT resolution, cross-talk simulation, scintillation quenching effect and hit threshold resolution. Different Monte Carlos have been generated to reproduce each effect. Detector

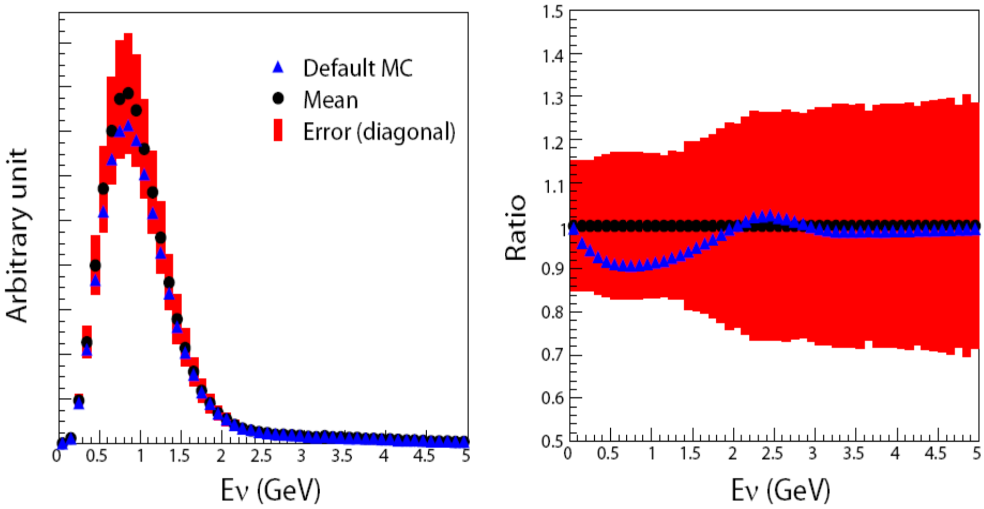

Figure 10.3: Monte Carlo predictions for the ν_μ flux in the SciBooNE detector. The filled bands represents the uncertainties from beam systematics.

response variations affect directly to the track reconstruction efficiency, modifying the track length and even the particle identification values (MuCL).

Uncertainties related to the energy deposition in the different detectors (SciBar, MRD and EC) can modify the muon momentum scale. This uncertainty has been considered as well.

1. **PMT resolution**

   The resolution of a single photo-electron (p.e.) in a MA-PMT is set to 50% in the simulation. This resolution has been selected by reproducing dEdx distributions of cosmic-ray muons. In the laboratory, the measured PMT resolution was around 70% at our operation gain. Therefore, the a variation of ±20% has been considered.

2. **Crosstalk of the MA-PMT**

   The amount of crosstalk in a MA-PMT was measured in the laboratory. The results shown that a 3.15% of the light was going to the adjacent channels, with an absolute error of 0.4%. So one sigma variation has been considered in the simulation to evaluate that systematic uncertainty.

3. **Scintillator quenching**

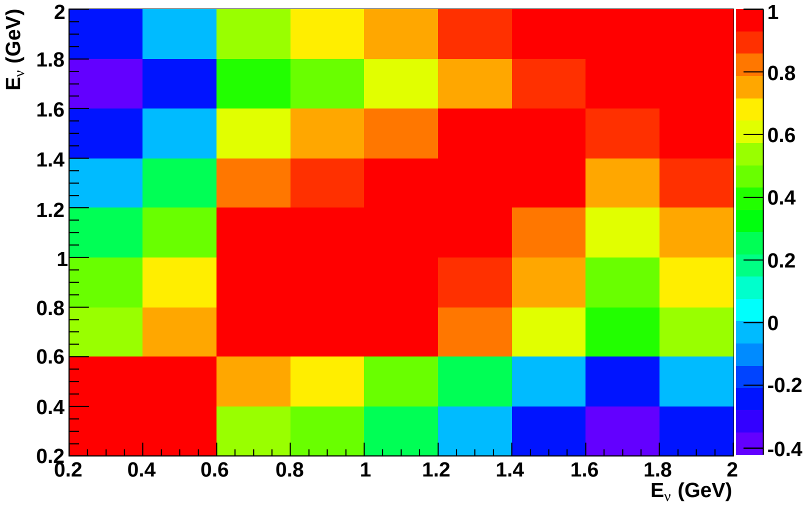

Figure 10.4: Cross section correlation error matrix associated to flux variations.

The simulation of the scintillator quenching effect, already described in section 4.1.1, has a systematic uncertainty associated to the error in the Birk constant (0.0208±0.0023 cm/MeV) (see equation (4.1)). One sigma variation has been applied to the simulation in order to evaluate this systematic.

4. **Hit threshold for track reconstruction**

   The track reconstruction software set the hit threshold in 2 photo-electrons. The photo-electrons quantity is converted to energy using conversion factors (determined channel by channel with cosmic muons). The channel-by-channel variation is approximately of 20%. Then, a variation of ±0.4 p.e. in the hit threshold has been applied to simulate the non-uniformity of this threshold.

5. **Muon momentum scale**

   The muon momentum is calculated, as mentioned the section 8.3.1, by the range and the energy deposition per unit of length (dEdx) at SciBar, EC and the MRD detectors. Uncertainties in the range or dEdx produce different muon momentum values. This uncertainty, called muon momentum scale, has been evaluated.

   In the SciBar detector, laboratory measurements of the scintillator strip

> density were done. Such measurents obtained an accuracy of 1%. For the MRD detector, the thickness of each steel plate was measured with uncertainty estimated of 1%. The density of a steel plate was also measured at several positions, obtaining an uncertainty less than 0.1%. In the EC detector, the stopping power was estimated to be 10%. However, the largest uncertainty comes from the difference in the calculation of the mean energy loss between the GEANT4 simulation and the pdg values[76], around 2%. The final muon momentum scale variation is of ±2%.

Table 10.3 shows the cross section systematic errors associated to detector response variations. The errors at low and high energies are specially large because in this case, each systematic uncertainty has been evaluated by generating new MC templates (not just by re-weighting the nominal MC). That effect introduces large errors at high and low energies (see section 10.2).

10.5 Neutrino interaction model

In the neutrino interaction model (based on NEUT), the axial-vector mass for both CCQE and resonant π production are set to 1.2 GeV. The uncertainty in this value is estimated to be ±0.1 GeV, extracted from recent measurements [36],[34]. Hence, a ±0.1 GeV variation is considered for systematic evaluation.

The CCQE cross section depends directly on the CCQE axial-vector mass (M_A^{QE}) such that, variations on M_A^{QE} can produce distortions of the own CCQE cross section measurement. So in this case, shape only variations have been considered. The procedure consists on normalizing the events of the new MC templates, where systematic variation has been added, to the events of the MC templates with nominal values.

Systematic effects associated to the $M_A^{CC\pi}$ and CC resonant cross section variations are considered. Both systematics sources produces variations of the CCQE background. So both have been treated in different way to avoid duplication of the same effect. Uncertainties in the $M_A^{CC\pi}$, with ±0.1 GeV variation, look for shape only variations in the cross section meanwhile uncertainties in CCπ cross section (±20%) measures absolute variations. In the last case, the a_{bck} has absorbed much of the variation (see table 10.4), successfully testing the role of this parameter within the fit.

Table 10.4 shows systematic errors of the CCQE cross section measurement corresponding to variations of the neutrino interaction model parameters (M_A^{QE}, $M_A^{CC\pi}$ and $\sigma_\nu^{CC\pi}$). The low energies (0.3 and 0.5 energy bins) are characterized by large errors, dominanted by the systematic variation of the CC resonant cross section.

10.6 Nuclear model effects

The hadrons produced in neutrino interactions can rescatter inside of the target nucleus. This nuclear effect can modify the final hadron kinematics. The nuclear effects simulated in the MC have been systematically varied to evaluate the influcen in the cross section measurement.

The MC simulates nuclear effects coming from pion absorption, inelastic interactions and charge exchange, where the charge of the pion final state differs from the initial. The proton scattering inside the nucleus and the Fermi momentum (P_{Fermi}) has been simulated. These effects have been systematically varied to evaluate the influence over the cross section measurement.

The table 10.5 shows the systematic errors associated to nuclear model effects. As expected, low neutrino energies are affected significantly by nuclear effects variations. At low energies, small variations of the kinematics of the outgoing pion and proton, can increase or decrease the number of reconstructed tracks.

10.7 Muon angle discrepancies

A particular data/MC discrepancy has been observed in the muon angle only for the 1-track sample (see 8.15). The muon angle discrepancy is still present even using the MC after the fit (introducing the fit parameters) and adding the systematics errors (see figure 10.5).

The muon angle discrepancy tends to be higher at higher angles, like following a linear dependency. Similar discrepancies are observed in muon momentum when the distribution is plotted for different muon angle cuts, as figure 10.6 shows. Since the dominant statistics in the muon momentum distribution are concentrated at low muon angles (see 10.6), the muon momentum discrepancy is apparently hidden.

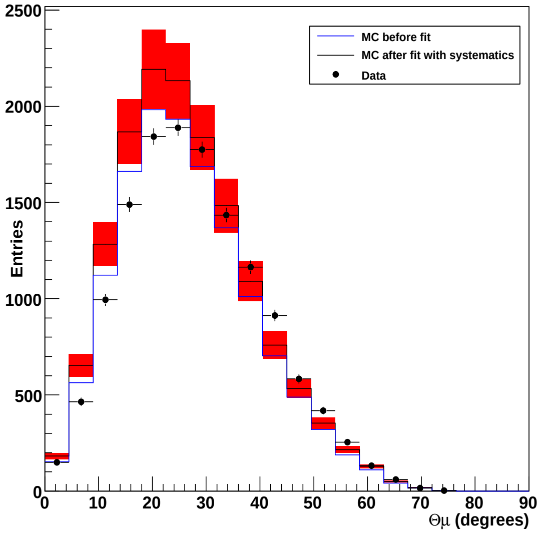

Figure 10.5: Muon angle distribution for 1-track sample. The data is compared with MC before and after the fit. Systemtic errors are included in MC after the fit.

With muon momentum and muon angle, one can reconstruct the neutrino energy and the momentum transfer of the event. Figure 10.7 shows the data/MC ratio in the phase space of Q^2_{rec} versus E^{rec}_ν. The obsereved discrepancy is more visible along the Q^2_{rec} than the E^{rec}_ν. Therefore, instead of analyzing the muon angle discrepancy, one should be focused on the Q^2_{rec} discrepancy. Since the 1-track sample dominates statistically at low Q^2_{rec} regions (below 0.2 GeV^2), we could relate this effect to the data defficit observed at low momentum transfer in other neutrino experiments like K2K[35] and MiniBooNE[36]. Note that, in our sample, data defficit is observed at low momentum transfer for 1-track sample as well (see figure 8.15).

The low Q^2_{rec} region has been historically an area of great model uncertainty, where nuclear effects become dominant. The relativistic Fermi gas model, used in K2K, MiniBooNE and SciBooNE, has demonstrated limitations to explain data at low Q^2_{rec} regions. In the case of the K2K experiment, the low Q^2_{rec} region was excluded for the M_A-analysis[35]. However, since MiniBooNE and SciBooNE works at lower neutrino energies, the low Q^2_{rec} region is highly populated. The MiniBooNE M_A-analysis[36] introduced a modification in the relativistic Fermi gas model, parametrizing the Pauli blocking suppression. Nowdays, several efforts are underway to incorporate better models beyond the Fermi gas model, like spectral functions[38, 40] and related models which take into account correlations between nuclei in the nuclear target.

Sicne the low Q^2_{rec} is not well represented in the MC, a modification in the Q^2_{rec} produces a change in efficiencies through detector acceptance that affects the measurement. For such a reason, the Q^2_{rec} discrepancy has been treated as a systematic associated to the cross section measurement. The systematic has been evaluated in the following way:

1. *Fit method:* The data/MC differences has been extracted through a linear fit in the Q^2_{rec} data/MC ratio (MC is POT normalized):

   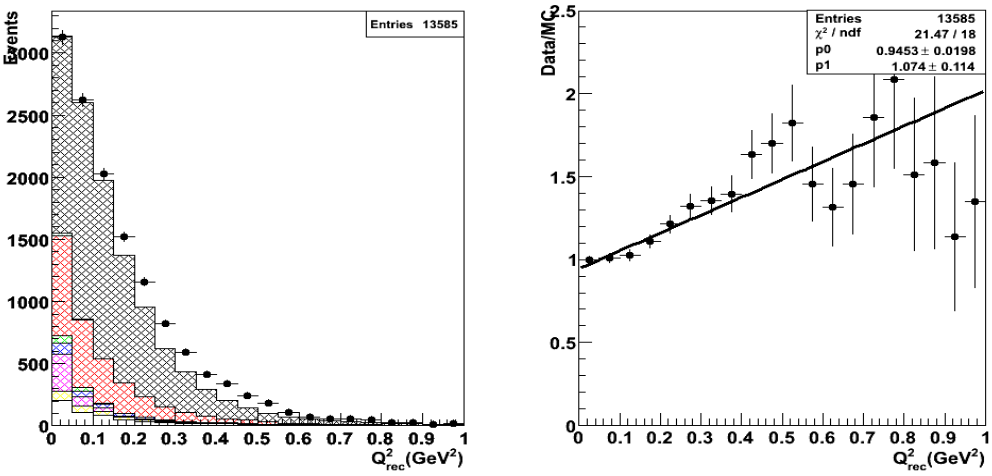

   with extracted linear parameters $p0 = 0.95 \pm 0.02$ and $p1 = 1.07 \pm 0.11$.

2. *Data/MC comparison:* The MC events have been re-weighted using extracted linear parameters. The same MC has been normalized to MC with nominal values in order to reflect only MC shape differences. Figure 10.8 shows the kinematic distributions for 1-track sample before and after the MC re-weighting. All the kinematic distributions present better data/MC agreement after the linear fit.

3. *Goodness of the fit:* Assuming Poisson statistics, likelihood values for the kinematic distributions before and after the MC tunning have been calculated:

variable	L_{before}	L_{after}
P_μ	94.03	42.25
Θ_μ	189.88	28.09
E_ν^{rec}	117.56	28.84
Q^2_{rec}	231.37	24.56

4. *Systematic evaluation:* the cross section using the MC re-weighted is extracted and compared with cross section using nominal values. The differences correspond with the systematic errors.

The table 10.6 shows the systematic errors associated to Q^2_{rec} discrepancies. Large systematic errors appear at low energies (below 0.6 GeV), as expected because low neutrino energies cover low Q^2 regions (see figure 10.9) where nuclear effects are dominant. The α parameter has a 30% relative error because the parameter itself measures migration events at low Q^2 region.

10.8 Summary

Figure 10.10 shows the contribution (relative errors) of the different systematic uncertainties within the different energy bins (for the tabulated form see 10.7). The low and high energies have large systematic errors in part, due to the already mentioned effect related with large fluctuations around low MC statistics (see section 10.2). In some sense, the evaluation of systematics at these energies could be over-estimated. This effect can be reduced by increasing the MC statistics in the energy tails, as later is shown. At intermediate energies, the flux systematic errors become dominant, with around 12% of mean relative error.

E_ν^{bin} (GeV)	absolute err. $(cm^2/nucleon)$ $(\times 10^{-38})$	relative err. (%)
0.3	0.2	66.7
	-0.19	63.3
0.5	0.04	36.4
	-0.03	27.3
0.7	0.05	10.4
	-0.04	8.3
0.9	0.05	9.6
	-0.04	7.7
1.1	0.05	8.6
	-0.05	8.6
1.3	0.06	10.9
	-0.07	12.7
1.5	0.12	21.1
	-0.11	19.3
1.7	0.14	42.4
	-0.11	33.3
1.9	0.4	28.6
	-0.3	21.4

E_ν^{bin} (GeV)	absolute err.	relative err. (%)
a_{bck}	0.11	8.0
	-0.11	8.0
F_N	0.09	8.9
	-0.08	7.9
α	0.0009	3.1
	-0.0008	2.8

Table 10.2: Flux systematic variations associated to the CCQE cross section (top table) and to other fit parameters (bottom table).

E_ν^{bin}(GeV)	Birk	PMT-res.	xtalk	Hit thres.	P_{scale}	subtotal
0.3	0.12	0.02	0.3	0.11	0.006	0.3
0.5	0.008	0.010	0.009	0.018	0.002	0.02
0.7	0.009	0.006	0.00013	10^{-6}	0.009	0.014
0.9	0.001	0.008	0.00005	0.002	0.010	0.013
1.1	0.012	0.012	0.008	0.001	0.011	0.02
1.3	0.016	0.004	0.02	0.001	0.011	0.03
1.5	0.05	0.02	0.07	0.003	0.011	0.09
1.7	0.1	0.07	0.3	0.02	0.007	0.3
1.9	0.19	0.12	0.4	0.2	0.03	0.5
a_{bck}	0.013	0.02	0.018	0.04	-0.00010	0.05
F_N	0.002	0.015	0.0001	0.005	0.020	0.03
α	0.005	0.003	0.0010	0.003	-0.000	0.006

Table 10.3: Detector response systematic errors. Dimensions for errors associated to cross sections are $(10^{-38} cm^2/nucleon)$. The a_{bck},F_N and α are dimensionless.

E_ν^{bin}(GeV)	M_A^{QE}	$M_A^{CC\pi}$	$\sigma_\nu^{CC\pi}$	subtotal	relative err.(%)
0.3	-0.08	-0.09	0.4	0.5	171.4
	0.06	0.09	-0.4	-0.6	203.2
0.5	-0.0019	-0.011	0.02	0.03	29.1
	-0.0004	0.012	-0.018	-0.04	38
0.7	0.004	-0.005	-0.009	-0.005	1.7
	-0.005	0.006	0.011	0.008	2.3
0.9	0.003	-0.006	-0.008	-0.006	1.7
	-0.004	0.007	0.010	0.008	2.2
1.1	0.004	-0.005	-0.006	-0.005	1.4
	-0.005	0.006	0.008	0.007	1.8
1.3	0.007	-0.006	-0.005	-0.004	1.8
	-0.008	0.006	0.006	0.005	2.0
1.5	-0.0003	-0.011	-0.004	-0.003	2.
	0.0011	0.013	0.005	0.007	2.6
1.7	-0.008	-0.02	0.0019	-0.005	6.7
	0.004	0.016	0.003	0.002	5.03
1.9	0.05	-0.05	-0.010	-0.002	5.05
	-0.05	0.06	0.014	0.02	5.8
a_{bck}	-0.019	0.04	0.03	0.15	10.7
	0.02	-0.06	-0.04	0.19	13.9
F_N	0.006	-0.013	-0.015	0.018	1.8
	-0.007	0.015	0.019	0.023	2.27
α	0.0011	-0.0005	0.0011	0.002	8.06
	-0.0014	0.0006	-0.0011	0.003	11.6

Table 10.4: Systematic errors associated to neutrino interaction model parameters. The errors dimensions are $(10^{-38} cm^2/nucleon)$. The a_{bck}, F_N and α are dimensionless.

E_ν^{bin}(GeV)	π-absorp.	π-inel.	charge exch.	P_{Fermi}	p-scat	subtotal	rel. err(%)
0.3	-0.07	-0.04	-0.03	0.06	0.04	0.11	37.4
	0.08	0.02	0.03	-0.06	-0.05	0.12	39.2
0.5	-0.02	-0.005	-0.002	0.004	0.005	0.03	19.7
	0.03	0.003	0.0019	-0.004	-0.005	0.03	28.07
0.7	-0.014	-0.002	-0.0013	0.008	-0.0015	0.016	3.4
	0.014	0.002	0.0013	-0.008	0.0013	0.016	3.4
0.9	-0.012	-0.0019	-0.0006	0.006	-0.002	0.013	2.6
	0.012	0.0017	0.0006	-0.006	0.002	0.013	2.6
1.1	-0.008	-0.001	-0.0009	0.006	-0.002	0.010	1.8
	0.008	0.0007	0.0009	-0.006	0.0018	0.010	1.8
1.3	-0.009	-0.0019	-0.0004	0.005	-0.0016	0.010	1.9
	0.009	0.0019	0.0004	-0.004	0.0014	0.010	1.8
1.5	-0.002	0.0008	-0.0008	-0.008	-0.007	0.011	1.9
	0.0018	-0.0002	0.0010	0.010	0.007	0.012	2.2
1.7	0.00004	-0.009	0.004	0.03	-0.0004	0.04	9.6
	0.006	0.008	-0.004	-0.04	0.0005	0.04	12.6
1.9	-0.007	0.03	0.0005	-0.03	-0.03	0.06	3.8
	0.002	-0.03	-0.00013	0.04	0.03	0.06	4.2
a_{bck}	0.05	0.017	0.009	-0.02	-0.0018	0.06	4.2
	-0.05	-0.008	-0.008	0.02	0.004	0.06	4.03
F_N	-0.02	-0.004	-0.0012	0.012	-0.004	0.03	2.4
	0.02	0.003	0.0012	-0.011	0.004	0.03	2.3
α	-0.0019	-0.0003	-0.0001	-0.0005	0.002	0.003	12.4
	0.002	0.0004	0.0002	0.0005	-0.002	0.003	12.7

Table 10.5: Systematic errors associated to nuclear model effects. The errors dimensions are $(10^{-38} cm^2/nucleon)$. The a_{bck}, F_N and α are dimensionless.

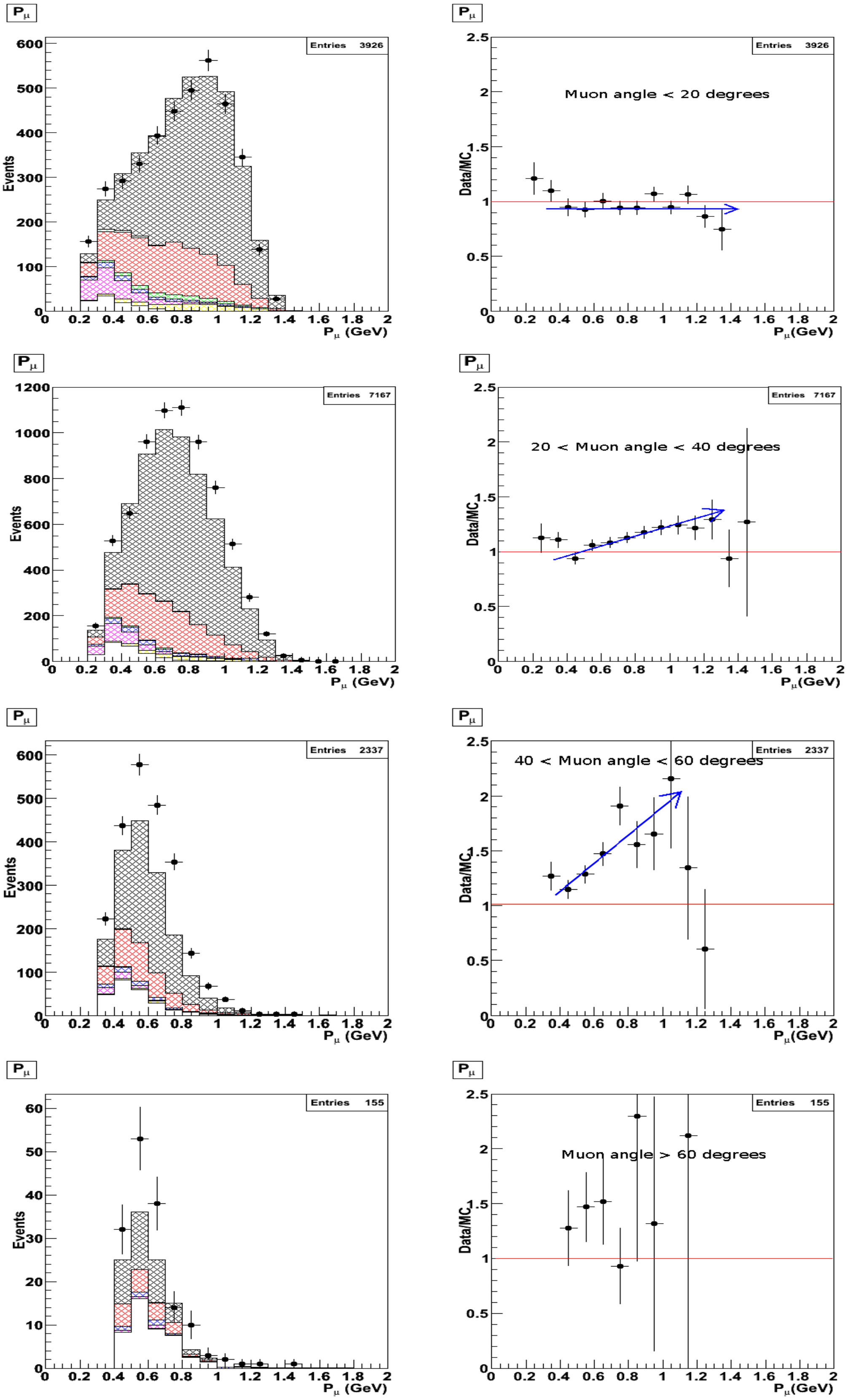

Figure 10.6: 1-track P_μ distribution for different cuts in the muon angle. Right hand plots shows data/MC ratio of distributions.

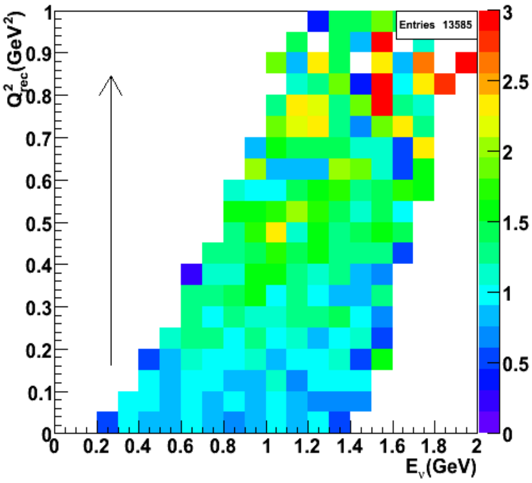

Figure 10.7: Data/MC ratio for 1-track events in the Q^2_{rec}, E_ν^{rec} phase space. The arrow indicates that the Q^2_{rec} variable contains the data/MC discrepancy.

E_ν^{bin} (GeV)	Q^2-discrep. err. ($10^{-38} cm^2/nucleon$)	relative err. (%)
0.3	1.2	400
0.5	0.11	100
0.7	0.013	2.7
0.9	0.002	0.4
1.1	0.002	0.3
1.3	0.011	2.
1.5	0.08	14.
1.7	0.07	21.2
1.9	0.09	6.4
a_{bck}	0.06	4.4
F_N	0.004	0.4
α	0.009	31.

Table 10.6: Cross section errors associated to the Q^2 discrepancies. The a_{bck}, F_N and α are dimensionless variables.

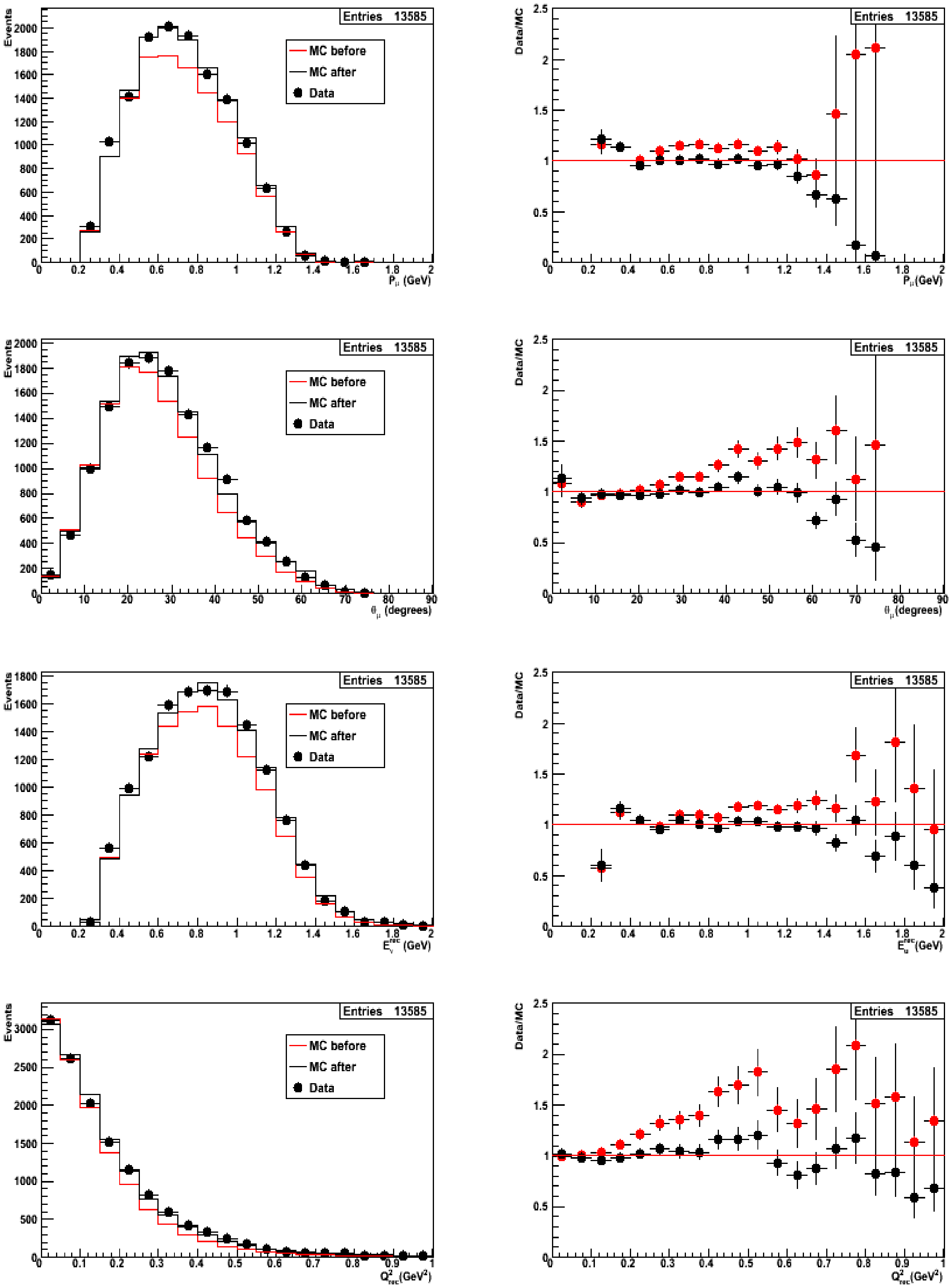

Figure 10.8: 1-track kinematic distributions comparing data and the MC before (red) after (black) the tunning, using parameters obtained in linear fit. See text for details.

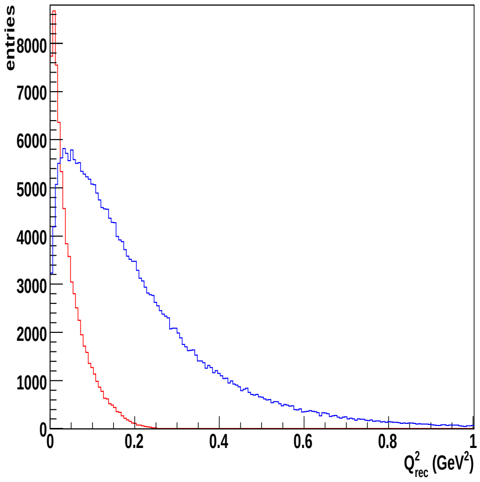

Figure 10.9: Monte Carlo Q^2_{rec} distributions for the total sample selection (1-track, 2-track QE and 2-track nonQE). Red and blue distributions represent Q^2_{rec} quantity for events with reconstructed energy lower and larger than 0.6 GeV, respectively.

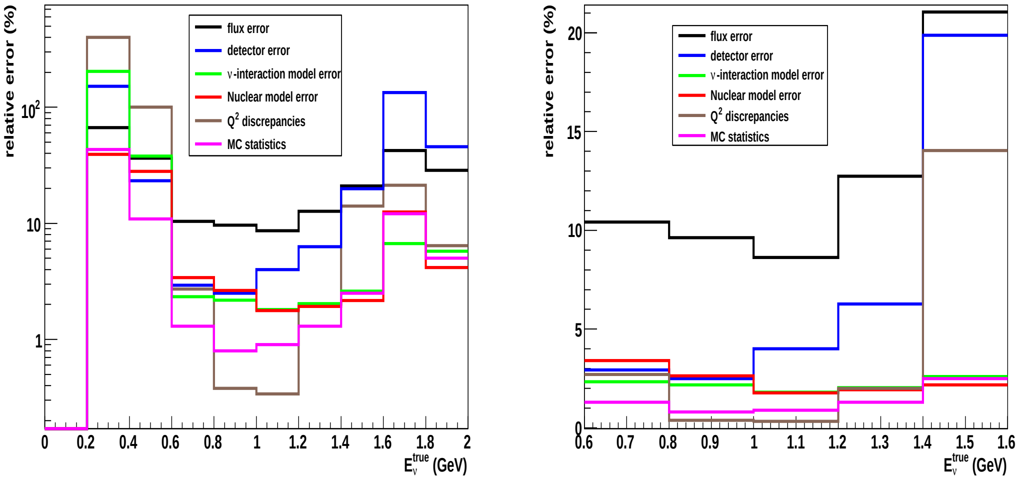

Figure 10.10: Maximum relative errors for the different systematic contributions for the total energy range (left hand plot) and for the intermediate energies (right hand plot).

E_ν^{bin} (GeV)	MC statistics(%)	Flux(%)	Detector respesponse(%)	Interaction Model(%)	Nuclear Model(%)	Q^2 discrepancy(%)
0.3	43.3	66.67	113.9	203.22	39.16	400
0.5	10.9	36.36	21.8	37.97	28.07	100
0.7	1.3	10.42	2.9	2.33	3.41	2.71
0.9	0.8	9.62	2.5	2.18	2.64	0.38
1.1	0.9	8.62	3.6	1.81	1.77	0.34
1.3	1.3	12.73	5.1	2.03	1.93	2
1.5	2.5	21.05	15.6	2.6	2.17	14.04
1.7	12.1	42.42	98.4	6.7	12.55	21.21
1.9	5.0	28.57	35.8	5.76	4.17	6.43
a_{bck}	0.8	8.03	3.6	13.93	4.18	4.38
F_N	0.9	8.86	2.5	2.27	2.37	0.39
α	>0.0001	3.1	22.9	11.6	12.65	31.03

Table 10.7: Summary table with the relative errors for all the systematic variations. The relative error corresponds to the higher relative error between positive and negative variation. In black, the dominant sytematic error.

Chapter 11

Results and discussion

11.1 Results

In the ν_μ-CCQE reaction ($\nu_\mu + n \rightarrow \mu^- + p$), the neutrino interacts with a neutron. Since our target is mainly Carbon (CH), a factor 13/6 transforms the values to cross section per neutron. Figure 11.2 shows the SciBooNE results of the absolute ν_μ-CCQE cross section as a function of the neutrino energy (for tabulated numbers see 11.2). Data include statistics plus systematic errors. The SciBooNE results are in agreement with the NEUT predictions.

The cross section values at intermediate energies (from 0.6 to 1.6 GeV) are dominated by the flux systematic errors. At low and high energies, the cross section values are characterized by large errors in comparison with intermediate energy values. These errors are in part dominated by large systematics uncertainties produced because of the low statistics associated to the high error correlation (see section 10.2).

The cross section measurement is integrated over the whole Q^2 region. However, our event selection covers low Q^2 regions (see fig 11.1), consequence of the detector geometry and the way in which the muon has been tagged (see section 8.1). The SciBooNE Q^2 area shown in figure 11.1 is defined by the maximum Q^2 value at each neutrino energy. This value is obtained when taking the 90% of the area in a Q^2_{true} distribution for each neutrino true energy bin and using our CCQE sample selection.

At low Q^2 region, the MC does not predict correctly the data, observing a data

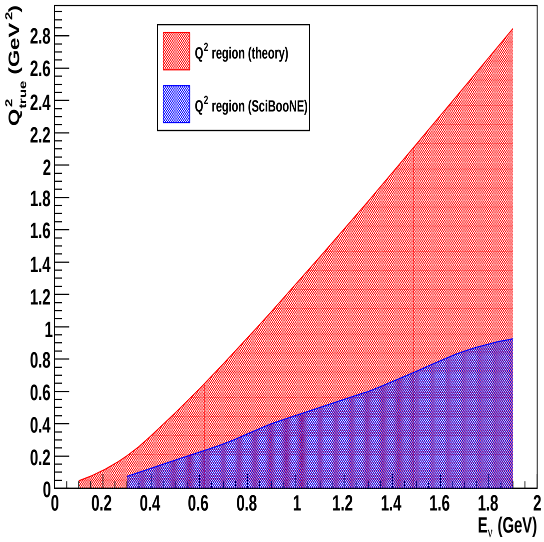

Figure 11.1: Range of Q^2_{true} values as function of the neutrino energy in our sample (blue area) compared with the theoretical predictions (blue area).

deficit for Q^2 values below 0.2 GeV^2. This observation is specially evident in our data and has required a systematic evaluation (see section 10.7). This is a well known problem[77] related to modeling the nuclear effects.

The Fermi gas model (FG) is the nuclear model used to describe nuclear effects in neutrino-nucleon interactions. However, this model is simplistic and then limited to describe more realistic effects. Nowadays, several theoretical nuclear models include more sophisticated nuclear effects[1](see latest discussions from NuInt09[78]). When more realistic nuclear effects are included, the predicted cross section takes smaller values compared with the FG. This may explain the low cross section value observed at the energy bin 0.5 GeV (see appendix G for additional check). At this energy, the associated Q^2 range is less than 0.2 GeV^2 (see fig. 11.1), where nuclear effects get special relevance. Even though, this value is still compatible with theoretical predictions in 2σ.

Since the total cross section may behaves different at integrated low Q^2 regions, where the measurement can be more sensitive to nuclear structure, the most

---

[1] Sophisticated nuclear models consider bound nucleons, with discrete energies in a many-body interaction framework.

appropiate way is to express the results as the cross section value per neutrino energy bin and associated with a Q^2 range, denoted by the maximum Q^2 value[2], as table 11.1 shows.

$< E_\nu >$ GeV	σ_{CCQE}^{DATA} $10^{-38} cm^2/neutron$	Q^2_{max} (GeV^2)
0.3	0.7	0.075
0.5	0.23	0.175
0.7	1.05	0.275
0.9	1.12	0.4
1.1	1.26	0.5
1.3	1.20	0.6
1.5	1.23	0.725
1.7	0.7	0.85
1.9	3.1	0.925

Table 11.1: Cross section values at different neutrino energies and associated with its a Q^2 range, denoted by the maximum Q^2 value (see text for details).

11.2 Comparison with other experiments

The SciBooNE results have been compared with the recent cross section measurement obtained at the MiniBooNE experiment[79]. Both experiments use the same nuclear target and share the neutrino flux, although the angular acceptance is different. MiniBooNE is placed at 500 meters from the nuclear target and measures muons in all directions due to the detector geometry. SciBooNE is at only 100 meters from the nuclear target and mainly measures forward muons.

The MiniBooNE experiment have measured the double differential CCQE cross section ($d\sigma/dT_\mu dcos\theta_\mu$) but single differential and absolute cross section are also reported. The absolute cross section has been calculated by an "unfolding" process[80] to associate reconstructed and true neutrino energies. Figure 11.3 shows the SciBooNE results in comparison with the MiniBooNE measurement. Note that, at intermediate energies, the SciBooNE results are systematically around 8% lower

---

[2] This value is obtained when taking the 90% of the area in a Q^2_{true} distribution for each neutrino true energy bin and using our CCQE sample selection.

$< E_\nu >$ GeV	σ_{CCQE}^{DATA} $10^{-38} cm^2/neutron$	stat.	sys.upper	sys. lower
0.3	0.7	1.1	+3.	-3.
0.5	0.23	0.11	+0.3	-0.3
0.7	1.05	0.04	+0.13	-0.11
0.9	1.12	0.04	+0.11	-0.11
1.1	1.26	0.04	+0.13	-0.13
1.3	1.20	0.07	+0.15	-0.17
1.5	1.23	0.15	+0.4	-0.3
1.7	0.7	0.4	+0.9	-0.9
1.9	3.1	0.9	+1.5	-1.3

Fit param.	value	stat.	sys.upper	sys. lower
a_{bck}	1.37	0.07	+0.16	-0.16
F_N	1.016	0.004	+0.10	-0.09
α	0.029	0.007	+0.012	-0.012

Table 11.2: Values of the absolute CCQE cross section per neutron with statistics and systematic errors (upper table). Values of other fit parameters with statistics and systematic errors (lower table).

than the MiniBooNE cross section but still compatible within the errors. Several reasons could explain such differences:

1. The CCπ prediction and detection. The π production and absorption is differently simulated using NEUT or NUANCE, neutrino generators for SciBooNE and MiniBooNE, respectively. The π detection is different in both experiments. SciBooNE distinguish $(\mu + p)$ from $(\mu + \pi)$ events, although both are taken for the fit. MiniBooNE detects directly the Cherenkov light produced by the π.

2. The nuclear effects, dominant at low Q^2 regions, can modify the reconstructed quantities affecting the measurement of the cross section. Although both experiments are affected by these effects, the SciBooNE data populates mainly low Q^2 regions (see fig. 11.1) in comparison with MiniBooNE (see ref.[79]), due to its forward acceptance.

The SciBooNE data have been compared with the NOMAD results published in 2009[81]. Both experiments scatter off neutrinos with Carbon, although the NOMAD neutrino energy spectrum is much higher than the SciBooNE one, see figure 11.4. The SciBooNE results seems to be slightly higher than the ones obtained in the NOMAD experiment. At high energies, the nuclear effects are negligible, so differences between experiments could be due to those effects.

The SciBooNE measurement has been compared with deuterium target experiments as an additional cross check. Figure 11.5 shows the SciBooNE results compared with BNL[42] and ANL[43] deuterium experiments. The SciBooNE results are compatible with both the ANL and BNL experiments. Note that the ANL and BNL measurements are free of nuclear effects. The fact that the SciBooNE results are compatible with deuterium cross section indicates that neutrino cross section in bound nucleons targets can be expressed as cross section per free nucleon times a conversion factor. This statement is only valid with current systematic errors (a 12% level at intermediate energies).

11.3 Future prospects

The precision of the measurement of the absolute CCQE cross section is limited by the systematic uncertainties. The dominant systematic source is different at different neutrino energies. At intermediate energies (0.6 to 1.6 GeV), the errors associated to neutrino flux predictions become dominant, with a relative error around 12% of the measurement. The flux uncertainties mainly come from the prediction of the π^+-production, as described section 10.3. This analysis has used the Sanford-Wang parameterization[61] model combined with HARP[45] results to predict the π^+-production. However, a new method called spline fit[82], together with HARP results, is able to reduce the π^+-production uncertainty from 14% to 5% [83]. This method would improve the cross section precision at intermediate energies.

The low and high neutrino energy regions, below 0.6 GeV and above 1.6 GeV, can be statistically populated using additional samples. At high energies, the muon-penetrating sample could be added, although flux errors at high energies are even higher (see plot 10.3). For such a reason, we would not expect significant improvement in the cross section measurement.

The low energies can be statistically populated using the SciBar-contained analysis. This analysis is based on selecting CCQE events completely contained in SciBar, that is, low neutrino energy events. We have already started to work with the two analyzes together (called combined analysis). The first preliminary results of the absolute neutrino cross section, with the combined analysis, are shown in figure 11.6. As expected, the cross section does not change significantly, with respect to the cross section using only SciBar-MRD analysis, at the energy region above 0.6 GeV. However, at low neutrino energies, the data is in better agreement, at the statistical level, with the predictions. Even though, the value at the energy bin 0.5 GeV is still below the theoretical predictions, supporting the arguments expossed above.

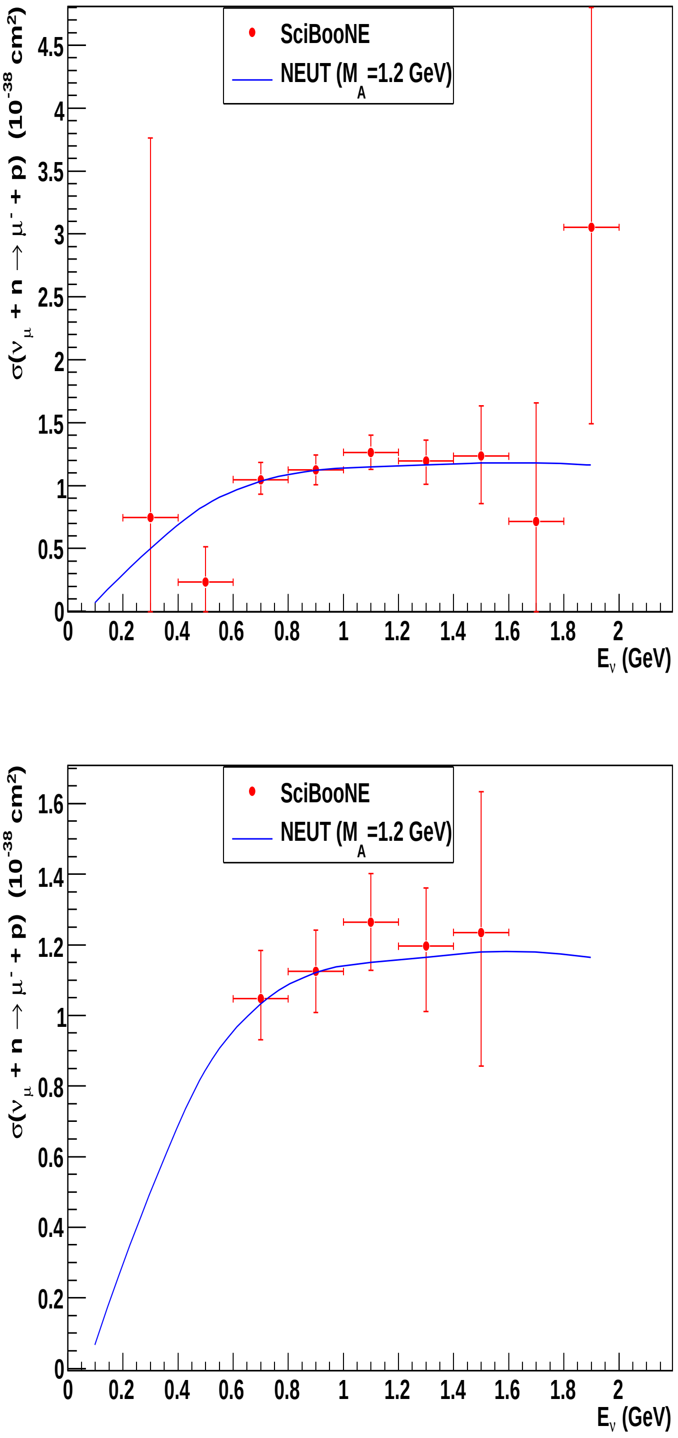

Figure 11.2: SciBooNE ν_μ-CCQE absolute cross section per neutron. Data include statistics plus systematic errors. Top panel shows the whole SciBooNE data, bottom panel only the intermediate energy points.

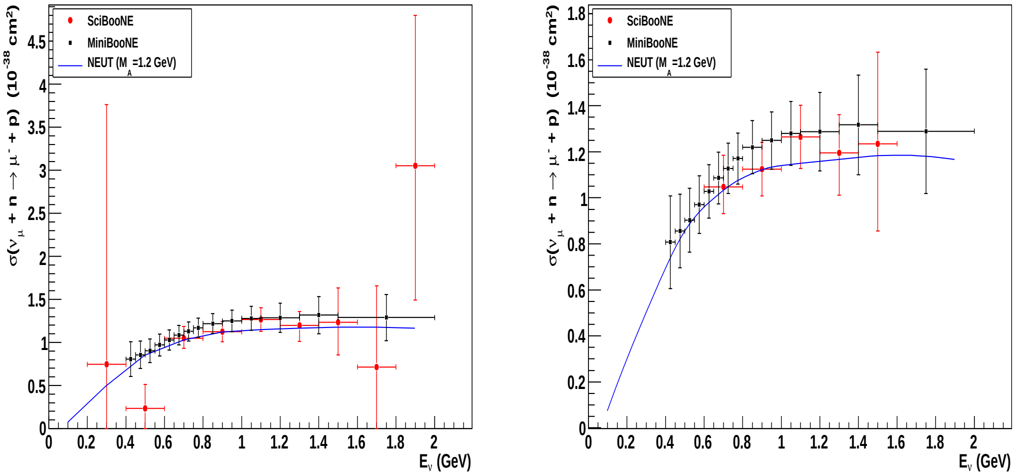

Figure 11.3: SciBooNE ν_μ-CCQE absolute cross section per neutron compared with MiniBooNE results. Left plot shows the whole SciBooNE data, right plot only the intermediate energy points.

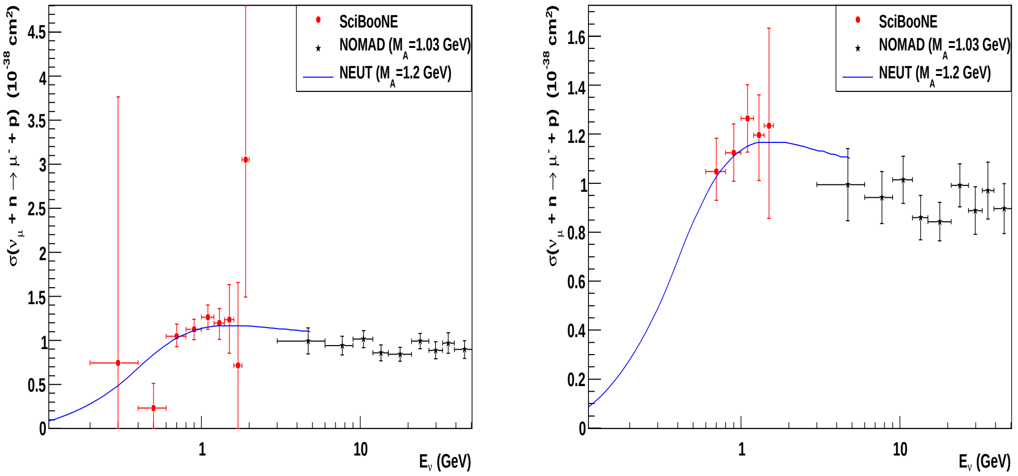

Figure 11.4: SciBooNE ν_μ-CCQE absolute cross section per neutron compared with the NOMAD experiment. Left plot shows the whole SciBooNE data, right plot only the intermediate energy points.

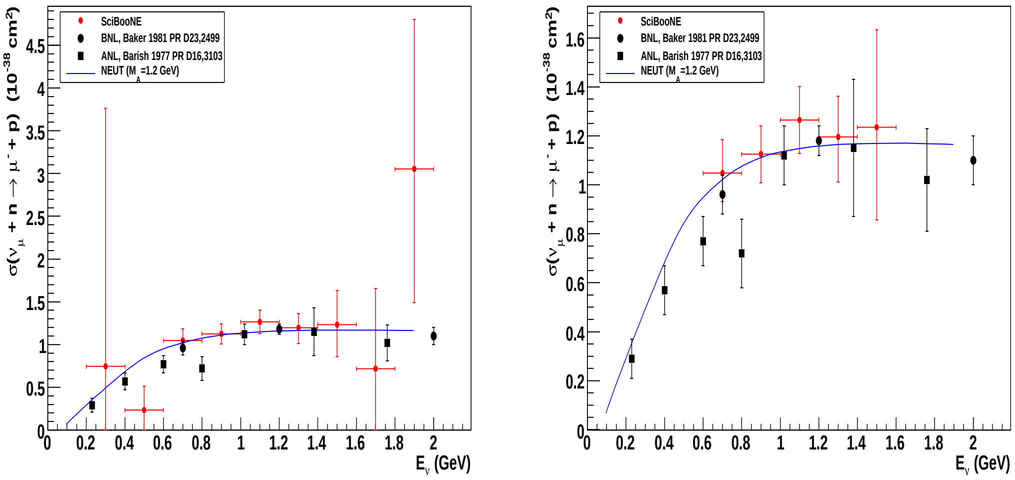

Figure 11.5: SciBooNE ν_μ-CCQE absolute cross section per neutron compared with experiments using deuterium targets (BNL and ANL).Left plot shows the whole SciBooNE data, right plot only the intermediate energy points.

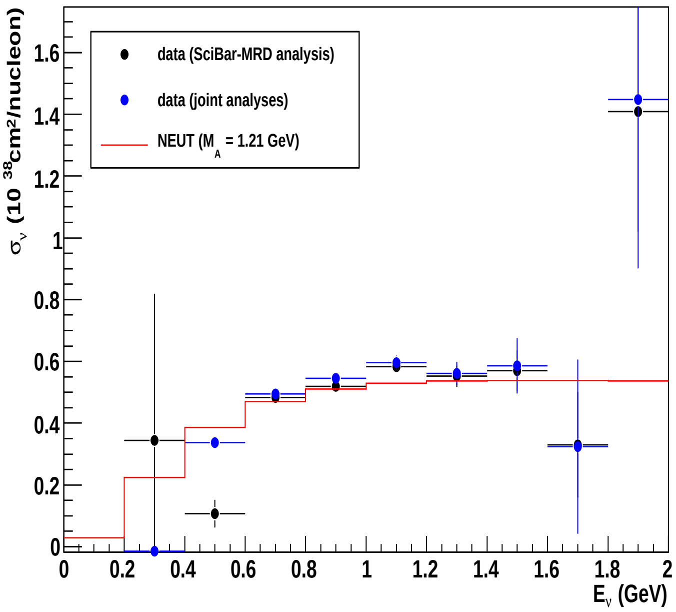

Figure 11.6: Preliminary results of the ν_μ-CCQE absolute cross section per nucleon combining the SciBar-MRD and the SciBar-contained analyses (blue dots) in comparison with results obtained using only the SciBar-MRD analysis (black dots). Only statistical errors are shown.

Chapter 12

Conclusions

A total of 18128 events have been selected from the SciBooNE ν_μ-data collection. The events are classified in one and two track events. The two track events have been separated in $\mu + p$ and $\mu + \pi$ events, producing a 2-track QE and nonQE enriched samples. The three samples, the 1-track and the 2-track QE and nonQE enriched samples, have been used for the extraction of the CCQE absolute cross section.

A fit method has been designed to determine the neutrino-nucleus CCQE absolute cross section. The fit works with MC templates, built up with observable variables (p_μ and θ_μ). The fit procedure evaluates the true neutrino energy shape variations between data and the MC quasi-elastic component. This information allows to determine the data cross section through of the NEUT cross section as reference. The fit also evaluates the background of the CCQE events, produced mainly by CCπ interactions. The results indicate that the CCπ contamination in the MC is under-estimated by approximately 37%.

The absolute neutrino-nucleus cross section at neutrino energies around 1 GeV has been presented. Systematics studies have shown that, at intermediate energies (0.6 and 1.6 GeV), the cross section values are dominated by the flux uncertainties, representing around 12% of variation. We are now working to improve the precision of the measurement at these energies by using the spline parameterization method in order to reduce the flux uncertainties.

The cross section values present large errors at high and low energies. Technical and physical reasons may explain such an errors. The technical reasons, already exposed in section 10.2, associate low statistics with large fluctuations during the fit. The physical reasons are related to the integrated Q^2 region where the cross section has been measured (see fig. 11.1). The SciBooNE data is statistically populated at low Q^2 values, with more than 66% of the total event selection below 0.2 GeV^2. At low Q^2 regions, the nuclear effects play an important role in the cross section measurement. Simple nuclear models like the RFG, used in this analysis, has demonstrated limited to describe the nuclear effects. Alternative theoretical models present more realistic description of the nuclear effects [78]. Realistic treatment of the nuclear effects suggest smaller cross section values. Since total neutrino cross section are then sensitive to nuclear structure, the results are also presented as the cross section value per neutrino energy bin and associated with a Q^2 range, denoted by the maximum Q^2 value (see table 11.1).

The SciBooNE and MiniBooNE measurements report the first absolute cross section data at energies around 1 GeV since the eighties. These measurements provide a mapping of the neutrino-nucleus interactions at low neutrino energies, useful to neutrino oscillation experiments, where usual oscillation peak is around 0.7 GeV.

The SciBooNE cross section data represent an input for testing more sophisticated theoretical nuclear models[84], although double differential cross section ($d\sigma/dP_\mu dcos\theta_\mu$) are preferred because of less model dependence. Neutrino-nucleus interactions with different nuclear targets will also provide additional information of the nuclear structure. This is the case of Minerva experiment[49], which will take data using C, Pb, Fe and He targets.

Large data taking and alternative detector techniques to reduce detector inefficiencies are essential to get more accurate cross section measurements. The T2K experiment[48] satisfies both requisites. The near T2K detector, called ND280, combines segmented detectors with time projection chambers inside of a magnetic field. The muon momentum will be accurately measured within the TPCs, with capabilities of track separation and identification. In addition, the off-axis idea will report a narrow neutrino energy spectrum peaked at 0.7 GeV, with more than 3×10^5 CCQE events expected in the near detector (corresponding to 5×10^{21} POT).

Bibliography

[1] Winter, *Neutrino Physics.* Cambridge University Press, (1991).

[2] C. L. Cowan, F. Reines, F. B. Harrison, H. W. Kruse, and A. D. McGuire, "Detection of the free neutrino: A Confirmation," *Science* **124** (1956) 103–104.

[3] G. Danby *et al.*, "Observation of High-Energy Neutrino Reactions and the Existence of Two Kinds of Neutrinos," *Phys. Rev. Lett.* **9** (1962) 36–44.

[4] J. Davis, Raymond, D. S. Harmer, and K. C. Hoffman, "Search for neutrinos from the sun," *Phys. Rev. Lett.* **20** (1968) 1205–1209.

[5] **SNO** Collaboration, Q. R. Ahmad *et al.*, "Direct evidence for neutrino flavor transformation from neutral-current interactions in the sudbury neutrino observatory," *Phys. Rev. Lett.* **89** (2002) 011301, `nucl-ex/0204008`.

[6] **Super-Kamiokande** Collaboration, Y. Ashie *et al.*, "Evidence for an oscillatory signature in atmospheric neutrino oscillation," *Phys. Rev. Lett.* **93** (2004) 101801, `arXiv:hep-ex/0404034`.

[7] **K2K** Collaboration, E. Aliu *et al.*, "Evidence for muon neutrino oscillation in an accelerator- based experiment," *Phys. Rev. Lett.* **94** (2005) 081802, `arXiv:hep-ex/0411038`.

[8] T. D. Lee and C.-N. Yang, "Question of Parity Conservation in Weak Interactions," *Phys. Rev.* **104** (1956) 254–258.

[9] S. Weinberg, "A Model of Leptons," *Phys. Rev. Lett.* **19** (1967) 1264–1266.

[10] A. Salam, *Elemetray Particle Theroy.* Almquist and Wiksells, Stockholm, (1969).

[11] S. L. Glashow, J. Iliopoulos, and L. Maiani, “Weak Interactions with Lepton-Hadron Symmetry,” *Phys. Rev.* **D2** (1970) 1285–1292.

[12] **KamLAND** Collaboration, K. Eguchi *et al.*, “First results from KamLAND: Evidence for reactor anti- neutrino disappearance,” *Phys. Rev. Lett.* **90** (2003) 021802, `arXiv:hep-ex/0212021`.

[13] C. Kraus *et al.*, “Final Results from phase II of the Mainz Neutrino Mass Search in Tritium β Decay,” *Eur. Phys. J.* **C40** (2005) 447–468, `arXiv:hep-ex/0412056`.

[14] O. Cremonesi, “Neutrinoless double beta decay: Present and future,” *Nucl. Phys. Proc. Suppl.* **118** (2003) 287–296, `arXiv:hep-ex/0210007`.

[15] C. Giunti and A. Studenikin, “Neutrino electromagnetic properties,” `arXiv:0812.3646 [hep-ph]`.

[16] **Gargamelle Neutrino** Collaboration, F. J. Hasert *et al.*, “Observation of neutrino-like interactions without muon or electron in the Gargamelle neutrino experiment,” *Phys. Lett.* **B46** (1973) 138–140.

[17] E. Fermi, “An attempt of a theory of beta radiation. 1,” *Z. Phys.* **88** (1934) 161–177.

[18] D. H. Perkins, *Introduction to High Energy Physics.* Addison-Wesley, (1987).

[19] C. S. Wu, E. Ambler, R. W. Hayward, D. D. Hoppes, and R. P. Hudson, “EXPERIMENTAL TEST OF PARITY CONSERVATION IN BETA DECAY,” *Phys. Rev.* **105** (1957) 1413–1414.

[20] A. Lesov, “The Weak Force: From Fermi to Feynman,” `arXiv:0911.0058 [physics.hist-ph]`.

[21] H. Yukawa, “On the interaction of elementary particles,” *Proc. Phys. Math. Soc. Jap.* **17** (1935) 48–57.

[22] A. D. M. Francis Halzen, *Quarks & Leptons.* John Wiley & Sons, (1984).

[23] T. Leitner, L. Alvarez-Ruso, and U. Mosel, “Charged current neutrino nucleus interactions at intermediate energies,” *Phys. Rev.* **C73** (2006) 065502, `arXiv:nucl-th/0601103`.

[24] M. Nowakowski, E. A. Paschos, and J. M. Rodriguez, "All electromagnetic form factors," *Eur. J. Phys.* **26** (2005) 545–560, `arXiv:physics/0402058`.

[25] N. C. Mukhopadhyay, "Weak form factors of the nucleon," `arXiv:nucl-th/9810039`.

[26] T. Kitagaki *et al.*, "High-Energy Quasielastic Muon-neutrino n → mu- p Scattering in Deuterium," *Phys. Rev.* **D28** (1983) 436–442.

[27] V. Bernard, L. Elouadrhiri, and U. G. Meissner, "Axial structure of the nucleon," *J. Phys.* **G28** (2002) R1–R35, `arXiv:hep-ph/0107088`.

[28] C. H. Llewellyn Smith, "Neutrino Reactions at Accelerator Energies," *Phys. Rept.* **3** (1972) 261–379.

[29] S. K. Singh and E. Oset, "Quasielastic neutrino (anti-neutrino) reactions in nuclei and the axial vector form-factor of the nucleon," *Nucl. Phys.* **A542** (1992) 587–615.

[30] S. Galster *et al.*, "Elastic electron - deuteron scattering and the electric neutron form-factor at four momentum transfers 5-fm**-2 ¡ q**2 ¡ 14-fm**-2," *Nucl. Phys.* **B32** (1971) 221–237.

[31] F. J. Ernst, R. G. Sachs, and K. C. Wali, "Electromagnetic form factors of the nucleon," *Phys. Rev.* **119** (1960) 1105–1114.

[32] R. G. Sachs, "High-Energy Behavior of Nucleon Electromagnetic Form Factors," *Phys. Rev.* **126** (1962) 2256–2260.

[33] H. S. Budd, A. Bodek, and J. Arrington, "Modeling quasi-elastic form factors for electron and neutrino scattering," `arXiv:hep-ex/0308005`.

[34] **K2K** Collaboration, R. Gran *et al.*, "Measurement of the quasi-elastic axial vector mass in neutrino oxygen interactions," *Phys. Rev.* **D74** (2006) 052002, `arXiv:hep-ex/0603034`.

[35] X. Espinal and F. Sanchez, "Measurement of the axial vector mass in neutrino-carbon interactions at K2K," *AIP Conf. Proc.* **967** (2007) 117–122.

[36] **MiniBooNE** Collaboration, A. A. Aguilar-Arevalo *et al.*, "Measurement of muon neutrino quasi-elastic scattering on carbon," *Phys. Rev. Lett.* **100** (2008) 032301, `arXiv:0706.0926 [hep-ex]`.

[37] Povh, B., Rith, K., Scholz, C., Zetsche, F., *Particles and Nuclei.* Springer Berlin Heidelberg, (2002).

[38] O. Benhar, A. Fabrocini, S. Fantoni, and I. Sick, "Spectral function of finite nuclei and scattering of GeV electrons," *Nucl. Phys.* **A579** (1994) 493–517.

[39] O. Benhar, "Nuclear response beyond the Fermi gas model," `arXiv:nucl-th/0307061`.

[40] A. M. Ankowski and J. T. Sobczyk, "Construction of spectral functions for medium nuclei," *Phys. Rev.* **C77** (2008) 044311, `arXiv:0711.2031 [nucl-th]`.

[41] **SciBooNE** Collaboration, A. A. Aguilar-Arevalo *et al.*, "Bringing the SciBar detector to the booster neutrino beam," `arXiv:hep-ex/0601022`.

[42] N. J. Baker *et al.*, "Quasielastic Neutrino Scattering: A Measurement of the Weak Nucleon Axial Vector Form-Factor," *Phys. Rev.* **D23** (1981) 2499–2505.

[43] W. A. Mann *et al.*, "Study of the reaction nu n → mu- p," *Phys. Rev. Lett.* **31** (1973) 844–847.

[44] G. P. Zeller, "Low energy neutrino cross sections: Comparison of various Monte Carlo predictions to experimental data," `arXiv:hep-ex/0312061`.

[45] **HARP** Collaboration, R. Tsenov, "HARP Collaboration results on the proton-nuclei interactions at few GeV energies," `arXiv:0806.3957 [hep-ex]`.

[46] **K2K** Collaboration, S. H. Ahn *et al.*, "Detection of Accelerator-Produced Neutrinos at a Distance of 250 km," *Phys. Lett.* **B511** (2001) 178–184, `arXiv:hep-ex/0103001`.

[47] S. G. Wojcicki, "MINOS experiment,". Prepared for 17th International Conference on Neutrino Physics and Astrophysics (Neutrino 96), Helsinki, Finland, 13-20 Jun 1996.

[48] **The T2K** Collaboration, Y. Itow *et al.*, "The JHF-Kamioka neutrino project," `arXiv:hep-ex/0106019`.

[49] **Minerva** Collaboration, D. Drakoulakos *et al.*, “Proposal to perform a high-statistics neutrino scattering experiment using a fine-grained detector in the NuMI beam,” `arXiv:hep-ex/0405002`.

[50] **NOvA** Collaboration, D. S. Ayres *et al.*, “NOvA proposal to build a 30-kiloton off-axis detector to study neutrino oscillations in the Fermilab NuMI beamline,” `arXiv:hep-ex/0503053`.

[51] T. Katori, “Neutrino Cross Section Measurements for Long-Baseline Accelerator-based Neutrino Oscillation Experiments,” `arXiv:0805.2476 [hep-ex]`.

[52] K. Nitta *et al.*, “The K2K SciBar detector,” *Nucl. Instrum. Meth.* **A535** (2004) 147–151, `arXiv:hep-ex/0406023`.

[53] J.B. Birks., *The theory and practice of scintillation counting.* Oxford [England]:Pergamon Press, (1964).

[54] M. Yoshida *et al.*, “Development of the readout system for the K2K SciBar detector,” *IEEE Trans. Nucl. Sci.* **51** (2004) 3043–3046.

[55] Y. Kurimoto, “The SciBooNE data acquisition system,” *AIP Conf. Proc.* **967** (2007) 313–315.

[56] C. Mariani, “EC detector at SciBooNE,” *J. Phys. Conf. Ser.* **160** (2009) 012035.

[57] S. Buontempo *et al.*, “Construction and test of calorimeter modules for the CHORUS experiment,” *Nucl. Instrum. Meth.* **A349** (1994) 70–80.

[58] J. Walding, “The muon range detector at SciBooNE,” *AIP Conf. Proc.* **967** (2007) 289–291.

[59] **MiniBooNE** Collaboration, A. A. Aguilar-Arevalo *et al.*, “The Neutrino Flux prediction at MiniBooNE,” `arXiv:0806.1449 [hep-ex]`.

[60] **GEANT4** Collaboration, S. Agostinelli *et al.*, “GEANT4: A simulation toolkit,” *Nucl. Instrum. Meth.* **A506** (2003) 250–303.

[61] J. R. Sanford and C. L. Wang. Bnl note no. 11299, (1967).

[62] Y. Hayato, “NEUT,” *Nucl. Phys. Proc. Suppl.* **112** (2002) 171–176.

[63] G. Mitsuka, “NEUT,” *AIP Conf. Proc.* **981** (2008) 262–264.

[64] H. Ikeda *et al.*, “KAMIOKANDE: THE KAMIOKA NUCLEON DECAY EXPERIMENT,”. UTLICEPP-82-04.

[65] A. K. et al., “Precise determination of $sin^2\theta$-w from measurements of the differential cross section for muon- neutrino p → muon-neutrino p and anti-muon-neutrino p → anti-muon-neutrino p,” *Phys. Rev. Lett.* **56** (1986) 1107.

[66] C. H. Albright, C. Quigg, R. E. Shrock, and J. Smith, “Neutrino - Proton Elastic Scattering: Implications for Weak Interaction Models,” *Phys. Rev.* **D14** (1976) 1780.

[67] R. A. Smith and E. J. Moniz, “Neutrino reactions on nuclear targets,” *Nucl. Phys.* **B43** (1972) 605.

[68] D. Rein and L. M. Sehgal, “Neutrino Excitation of Baryon Resonances and Single Pion Production,” *Ann. Phys.* **133** (1981) 79.

[69] R. P. Feynman, M. Kislinger, and F. Ravndal, “Current matrix elements from a relativistic quark model,” *Phys. Rev.* **D3** (1971) 2706–2732.

[70] C. Berger and L. M. Sehgal, “Lepton Mass Effects in Single Pion Production by Neutrinos,” *Phys. Rev.* **D76** (2007) 113004, `arXiv:0709.4378 [hep-ph]`.

[71] D. Rein and L. M. Sehgal, “Coherent pi0 Production in Neutrino Reactions,” *Nucl. Phys.* **B223** (1983) 29.

[72] M. Derrick *et al.*, “Properties of the Hadronic System Resulting from anti-Muon-neutrino p Interactions,” *Phys. Rev.* **D17** (1978) 1.

[73] H. W. Bertini, “Nonelastic interactions of nucleons and pi mesons with complex nuclei at energies below 3 gev,” *Phys. Rev.* **C6** (1972) 631–659.

[74] S. J. Lindenbaum and R. M. Sternheimer, “Isobaric nucleon model for pion production in nucleon- nucleon collisions,” *Phys. Rev.* **105** (1957) 1874–1879.

[75] I. Kisel and G. Ososkov, “An application of cellular automata and neural networks for track reconstruction in high energy physics,”. Prepared for 3rd International Workshop on Software Engineering, Artificial Intelligence and Expert systems for High-energy and Nuclear Physics, Oberammergau, Germany, 4-8 Oct 1993.

[76] **Particle Data Group** Collaboration, C. Amsler *et al.*, “Review of particle physics,” *Phys. Lett.* **B667** (2008) 1.

[77] A. M. Ankowski, O. Benhar, and N. Farina, “Analysis of the Q^2-dependence of charged-current quasielastic processes in neutrino-nucleus interactions,” *Phys. Rev.* **D82** (2010) 013002, `arXiv:1001.0481 [nucl-th]`.

[78] S. Boyd, S. Dytman, E. Hernandez, J. Sobczyk, and R. Tacik, “Comparison of models of neutrino-nucleus interactions,” *AIP Conf. Proc.* **1189** (2009) 60–73.

[79] **MiniBooNE** Collaboration, A. A. Aguilar-Arevalo *et al.*, “First Measurement of the Muon Neutrino Charged Current Quasielastic Double Differential Cross Section,” `arXiv:1002.2680 [hep-ex]`.

[80] G. Cowan, *Statistical data analysis.* Oxford Science Publications, (1998).

[81] **NOMAD** Collaboration, V. Lyubushkin *et al.*, “”A study of quasi-elastic muon neutrino and antineutrino scattering in the NOMAD experiment”,” `arXiv:0812.4543 [hep-ex]`.

[82] W. H. Press, S. A. Teukolsky, W. T. Vetterling, and B. P. Flannery, *Numerical Recipes in C++.* cambridge university press, (2002).

[83] T. Katori, “A Measurement of the muon neutrino charged current quasielastic interaction and a test of Lorentz violation with the MiniBooNE experiment,”. FERMILAB-THESIS-2008-64.

[84] A. V. Butkevich, “Analysis of flux-integrated cross sections for quasi- elastic neutrino charged-current scattering off ^{12}C at MiniBooNE energies,” `arXiv:1006.1595 [nucl-th]`.

[85] A. V. Belitsky, X.-d. Ji, and F. Yuan, “Quark imaging in the proton via quantum phase-space distributions,” *Phys. Rev.* **D69** (2004) 074014, `arXiv:hep-ph/0307383`.

Appendix A

Weak Isospin and hipercharge

In the nuclear interpretation, the isospin quantum number arises because the nucleon may be wiewed as having an internal degree of freedom with two allowed states (proton and neutron), so the nuclear interaction does not distinguish. Such interpretation can be matematically described by the isospin symmetry group SU(2) in which (n,p) form the fundamental representation. Thus, the isospin wavefunction of the nucleon can be expressed as two-component matrix:

$$N = \begin{pmatrix} p \\ n \end{pmatrix}, \tag{A.1}$$

where neutron and proton are the different states of the nucleon, represented as:

$$p = \begin{pmatrix} 1 \\ 0 \end{pmatrix}, n = \begin{pmatrix} 0 \\ 1 \end{pmatrix}. \tag{A.2}$$

In the isospin space, the proton and neutron can be identified as isospin-up and isospin-down states of the nucleon.

Analogous to the nuclear case, the weak interaction does not distinguish between leptons (e,nu) or quarks (q,q'), so a weak isospin can describe the different states of the same wavefuntion:

$$L = \begin{pmatrix} \nu_l \\ l \end{pmatrix}_L, \begin{pmatrix} q \\ q' \end{pmatrix}. \tag{A.3}$$

Here, one can define left-handed fields that transform as $SU(2)_L$ doublets. However, the right-handed partners just transforms as singlets because neutrinos are only left-handed spin polirized.

The weak hypercharge (Y) is a quantum number, associated with the symmetry group U(1), that relates the electric charged (Q, in units of e) and the third component of isospin (I^3):

$$Q = I^3 + \frac{1}{2}Y. \tag{A.4}$$

Appendix B

Deduction of general expression for the cross section

Given the following reaction:

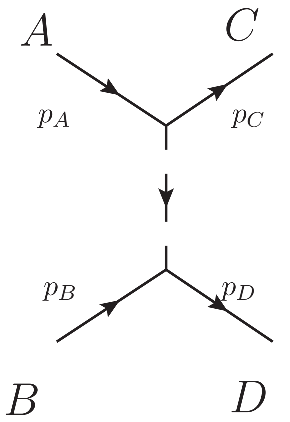

$$A + B \rightarrow C + D$$

, the cross section of $A + B \rightarrow C + D$ scattering is defined as follows:

$$\text{Cross section} = \frac{W_{fi}}{\text{initial flux}}(\text{number of final states}), \tag{B.1}$$

where W_{fi} is the transition rate. Such quantity defines the probability of a particle to change from an initial state i to a final state f. The expression is written as follows[22]:

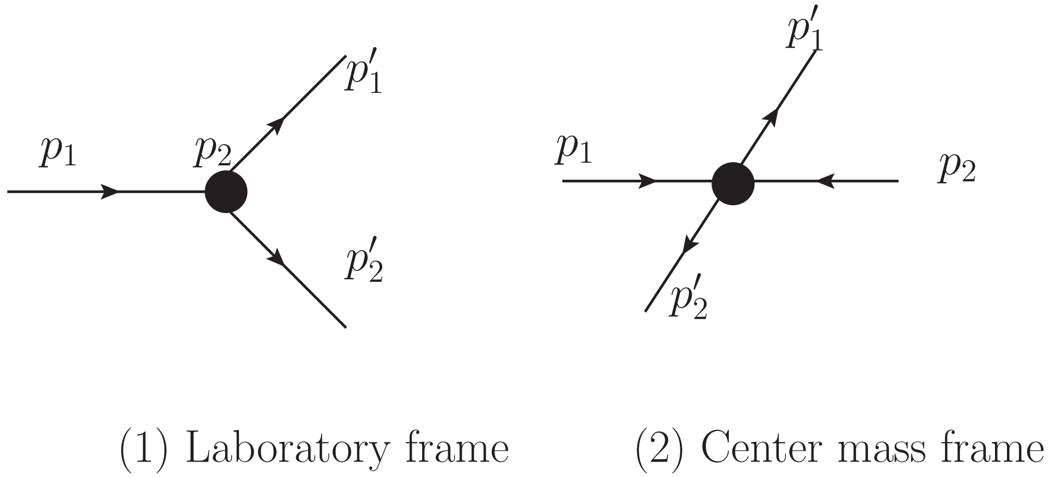

Figure B.1: Laboratory frame collition and center of mass frame collition.

$$W_{fi} = (2\pi)^2 \frac{\delta^4(p_C + p_D - p_A - p_B)|\mathcal{M}|^2}{V^4}, \tag{B.2}$$

where $\mathcal{M}$ is defined as the invariant amplitud and V is the volume occupied by the particles.

The *number of final states* in a volume V with momenta in element d^3p to be $V^3p/(2\pi)^3$. However, one have 2E particles[1] V and then,

$$\text{Number final states/particle} = \frac{Vd^3p}{(2\pi)^3 2E}. \tag{B.3}$$

For C and D particles scattered into the momentum elements d^3p_C, d^3p_D,

$$\text{number of final states} = \frac{Vd^3p_C}{(2\pi)^3 2E_C}\frac{Vd^3p_D}{(2\pi)^3 2E_D}. \tag{B.4}$$

The *initial flux* can be easily calculated by cnsidering the laboratory frame. The number of beam particles passing through unit area per unit time is $v_A 2E_A/V$, and the number of target particles per unit volume is $2E_B/V$. To obtain a normalization-independet measure of the ingoing density, we take the flux as follows:

$$\text{Initial flux} = |v_a|\frac{2E_A}{V}\frac{2E_B}{V}. \tag{B.5}$$

---

[1] For a free particle with an associated wavefunction $\phi = Ne^{-ip\cdot x}$, the probability density is described as $\rho = 2E|N|^2$. Then, the number of particles in a volume V is just the integration over the probability density, which results 2E if we adopt the normalization $N = 1/\sqrt{V}$.

Inserting X, Y and Z into W, we arrive to the differential cross section $d\sigma$ for scattering into $d^3p_Cd^3p_D$:

$$d\sigma = \frac{1}{|v_A|2E_A2E_B}|\mathcal{M}|^2\delta^4(p_C + (p_D - p_A - p_B)\frac{(2\pi)^4}{(2\pi)^4}\frac{Vd^3p_C}{(2\pi)^32E_C}\frac{Vd^3p_D}{(2\pi)^32E_D}. \quad \text{(B.6)}$$

The differential cross section in the symbolic form can be writte as follows:

$$d\sigma = \frac{|\mathcal{M}|^2}{F}dLips, \quad \text{(B.7)}$$

where dLips and F represent the Lorentz invariant phase space factor and the flux respectively. The dLips expression is written as follows:

$$dLips = (2\pi)^4\delta^4(p_C + p_D - p_A - p_B)\frac{d^3p_C}{(2\pi)^32E_C}\frac{d^3p_D}{(2\pi)^32E_D}, \quad \text{(B.8)}$$

and can be generalized for N ingoing and outgoing scatter particles in the way:

$$dLips = (2\pi)^4\delta\left(\sum p'_f - \sum p_i\right)\prod\frac{d^3p'_f}{(2\pi)^32E'_f}. \quad \text{(B.9)}$$

The flux (F), for a general collinear collision between A and B, results

$$F = |v_A - v_B| \cdot 2E_A \cdot 2E_B = 4(p_AE_B + p_BE_A), \quad \text{(B.10)}$$

where $v_i = p_i/E_i$ correspond to the relative velocity of the particles i.

Since the dLips is an invariant, the most convenient frame can be selected. Working in the center of mass frame (CM), the dLips is written as follows:

$$\begin{aligned} dLips &= \frac{1}{4(2\pi)E'_1E'_2}\delta(E'_1 + E'_2 - \sqrt{s})\delta^3(\bar{p'}_1 + \bar{p'}_2)d^3p'_1d^3p'_2 && \text{(B.11)} \\ &= \frac{1}{4(2\pi)E'_1E'_2}\delta(E'_1 + E'_2 - \sqrt{s})d^3p'_1, && \text{(B.12)} \end{aligned}$$

where $\sqrt{s} = (E_1 + E_2)$ is a Mandeltam variable, and $p_1 + p_2 = 0$ in the CM. On the other hand,

$$d^3p'_1 = |p'_1|dp'_1d\Omega_{CM} \quad \text{(B.13)}$$

where $d\omega$ is de differential solid angle. dp'_1 can be evaluated taking into account that,

$$\int dx\delta(f(x)) = \sum_i |f'(x_i)|^{-1} \tag{B.14}$$

and

$$\frac{\partial}{\partial|p'_1|}(E'_1 + E'_2 - \sqrt{s}) = \frac{|p'_1|\sqrt{s}}{E'_1 E'_2}. \tag{B.15}$$

thus, the invariant Lorentz factor is written

$$dLips = \frac{|p'_1|}{16\pi^2\sqrt{s}} d\Omega_{CM}. \tag{B.16}$$

Finally, taking the expression of the flux in the CM ($4|p_1|\sqrt{s}$), the differential cross section per solid angle in the center of mass frame is written as follows:

$$\frac{d\sigma}{d\Omega_{CM}} = \frac{1}{64\pi^2 s}\frac{|p'_1|}{|p_1|}|\mathcal{M}|^2. \tag{B.17}$$

Using the Lorentz invariant variable

$$\begin{aligned} Q^2 = t &= m_1^2 + m_1^2 - 2E_1E'_1 + 2|p_1||p'_1|cos\theta. \\ dQ^2 = dt &= 2|p_1||p'_1|cos\theta \\ &= 2|p_1||p'_1|\frac{d\Omega_{CM}}{2\pi}, \end{aligned}$$

the cross section can be expressed as follows:

$$\frac{d\sigma}{dQ^2} = \frac{1}{64\pi^2 s}\frac{1}{|p_{1,CM}^2|}|\mathcal{M}|^2 \tag{B.18}$$

or in the laboratory frame:

$$\frac{d\sigma}{dQ^2} = \frac{1}{64\pi^2 m_2^2}\frac{1}{|p_{1,lab}^2|}|\mathcal{M}|^2. \tag{B.19}$$

Appendix C

Dipole Form Factor

In the scattering theory, the observables from scattering experiments can be interpreted as a Fourier transformation of the charge distribution of the scattering body[83]. Suppose for instance, an electron elastic experiment in which the scattering body is an atom. The procedure is to measure the anglular distribution of the scattered electrons and compare it to the cross section for scattering electrons from a point-like charge,

$$\frac{d\sigma}{d\Omega} = \frac{d\sigma}{d\Omega}_{point} |F(q)|^2, \tag{C.1}$$

where q is the momentum transfer between the incident electron and the target. If one considers a scattering of the unpolarized electrons of energy E from a static, spinless charge distribution Ze$\rho(x)$, normalized in the way

$$\int \rho(x) d^3x = 1, \tag{C.2}$$

for a static target, it is found that the form factor in C.1 is just the Fourier transformation of the charge distribution,

$$F(q) = \int \rho(x) e^{iq \cdot x} d^3x. \tag{C.3}$$

By the normalization condition, F(0)=1. If the momentum transfer is not too large, we can expand the exponential, giving the result

$$\begin{aligned} F(q) &= \int \left(1 + iq\cdot x - \frac{(q\cdot x)^2}{2} + ...\right) \rho d^3x && \text{(C.4)} \\ &= 1 - \frac{1}{6}|q|^2 < r^2 > +...., && \text{(C.5)} \end{aligned}$$

where the charge distribution (ρ) is assumed to be spherically symmetric (only function o $r \equiv |x|$). Therefore, the scattering angle is just measuring the square radious of the charged cloud aroud the atom. However this argument only works for low $|q|$, where the wavelength associated to the propagator ($1/|q|$) is larger or of the same order than the charge cloud radius.

If now the charge distribution has an exponential form,

$$\rho(r) = \rho(0)e^{-Mr}, \tag{C.6}$$

where M is the mass of the scattering body, the form factor results

$$F(|q|) \propto \left(1 - \frac{|q|^2}{M^2}\right)^{-2}, \tag{C.7}$$

that is, the form factor adopts the dipole form. Once again, this result is an approximation valid for low momentum transfer ($|q| \leq M$). For momentum transfer of the order of the mass of the target, not only the internal structure of the scattering body, but also the dynamical effects contribute to the form factor and the interpretation is more complicated[85].

When the target is a proton or a neutron, not only the charge distribution but also the magnetic moment must be included within the form factors. In a most realistic case, the target is not static but will recoil particle's bombardment. So in these cases, and assuming always low momentum transfer, the nucleon structure should be described by two form factors, one associated to the charged density (G_E) and another with the magnetic moment (G_M)[31][32].

Appendix D

Fake data studies

The fit method has been tested using the MC as data, so called *fake data*. With such an assumption, the minimization function should return fit parameters values equal to the unity.

The MC used in this fake data studies corresponds to the MC obtained after the CCQE selection cut. The fit method has been executed N=1000 times. In each iteration, a different fake data sample has been produced. The fake data sample production is based on adding different seeds to each MC event that is distributed randomly according to Poisson statistics. So each iteraction represents a different data configuration. Therefore, in each iteraction a set of fit parameters is obtained. Same conditions than those used with real data has been used, that is, a0 and a4 has been fixed to one. Figures D.1 and D.2 show the statistic fluctuations for each fit parameter[1] corresponding to 995 iterations. Notice that in all cases the fluctuations are peaked to one, except for the α parameter that, as expected, is peaked to cero.

The N-iteractions can then produce N-cross section values. The mean of the cross section value for each neutrino energy bin is shown in figure D.3. Statistical errors are associated to the fake data statistics. Notice a good agreement between fake data and MC, confirming the robustness of the fit.

---

[1] The statistics correspond to 995 events because 5 iterations failure due to convergence problem.

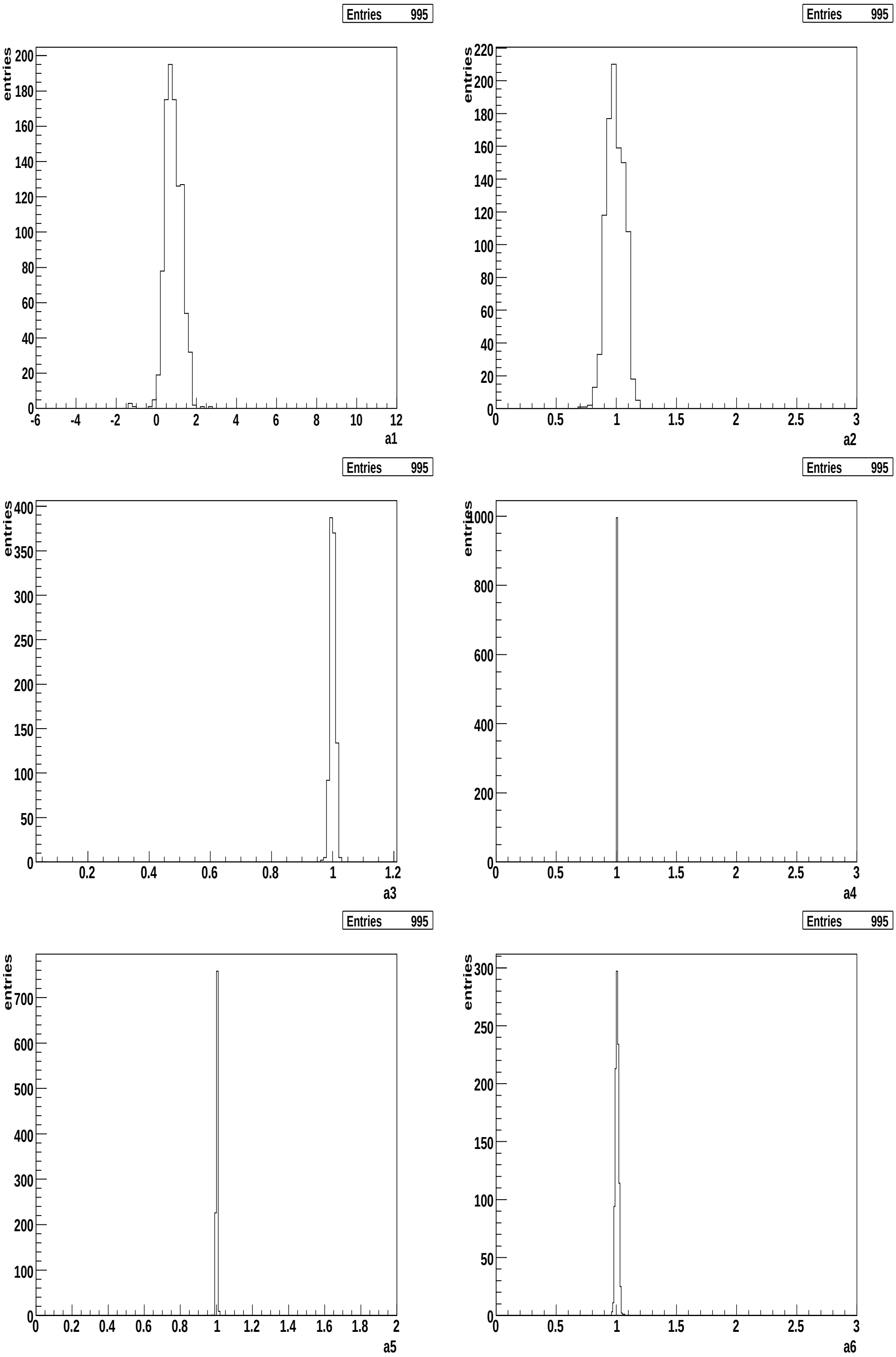

Figure D.1: Statistical fluctuations of the fit parameters corresponding to N=995 iterations of the fit process.

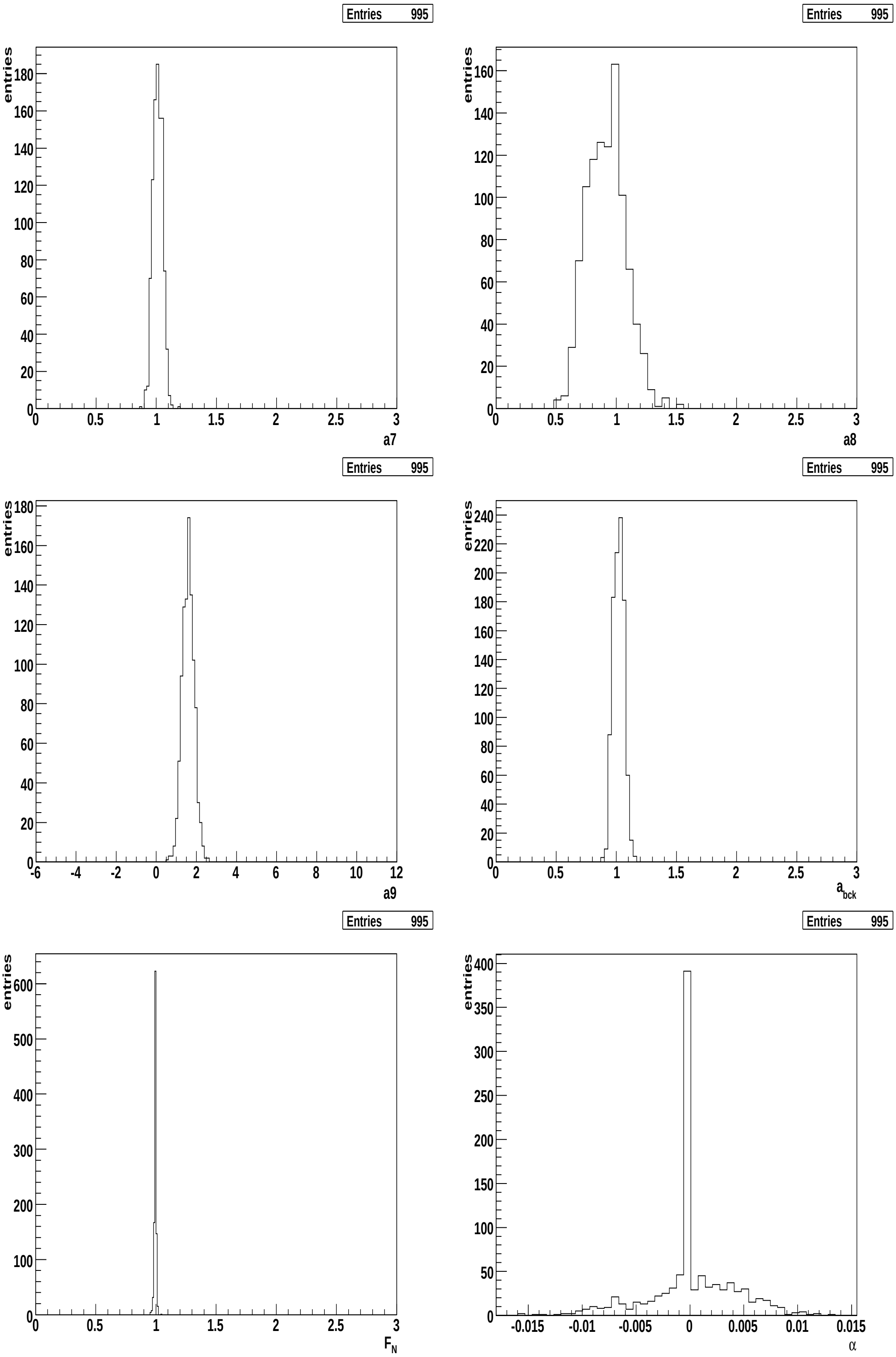

Figure D.2: Statistical fluctuations of the fit parameters corresponding to N=995 iterations of the fit process.

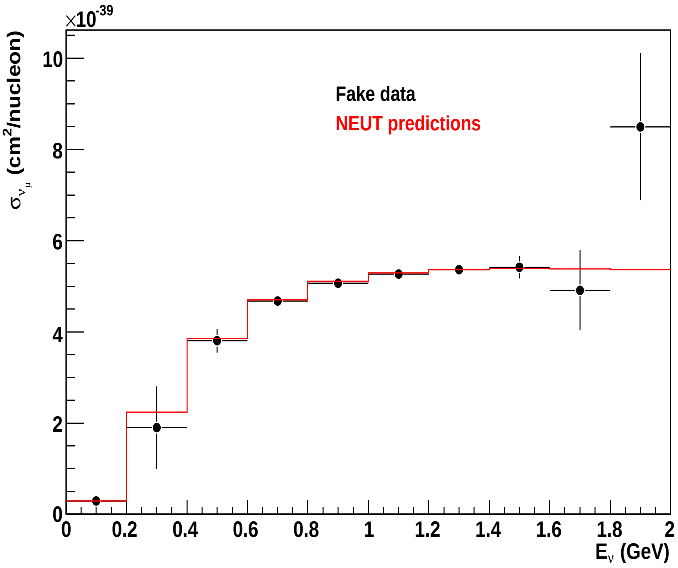

Figure D.3: ν_μ-CCQE absolute cross section per nucleon as a function of the neutrino energy using fake data. Red line corresponds to the NEUT predictions and black dots to fake data with statistic errors added.

Appendix E

POT normalization

When the Monte Carlo is normalized to the number of protons on target (POT) from data, a factor slightly higher than one appears as table E.1 shows. This factor is related to the the uncertainties associated to the cross section predictions.

Sample	Data/MC POT Norm.	Data/MC SciBar-MRD Norm
1-track	1.12	1.02
2-track QE	1.18	1.07
2-track nonQE	1.28	1.17

Table E.1: Data/MC ratios for different samples using the POT and the SciBar-MRD normalization factors.

The kinematics of the 1-track and 2-track QE and nonQE samples, with MC normalized to POT, are shown in figures E.2,E.3 and E.4. The color code is shown in figure E.1.

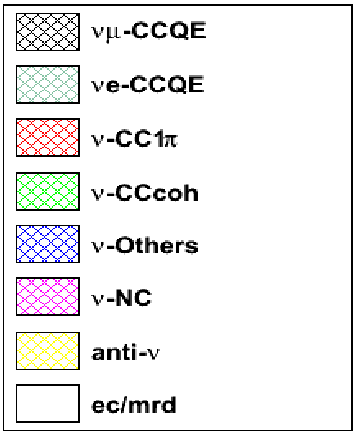

Figure E.1: Color code for MC interaction channels usig NEUT.

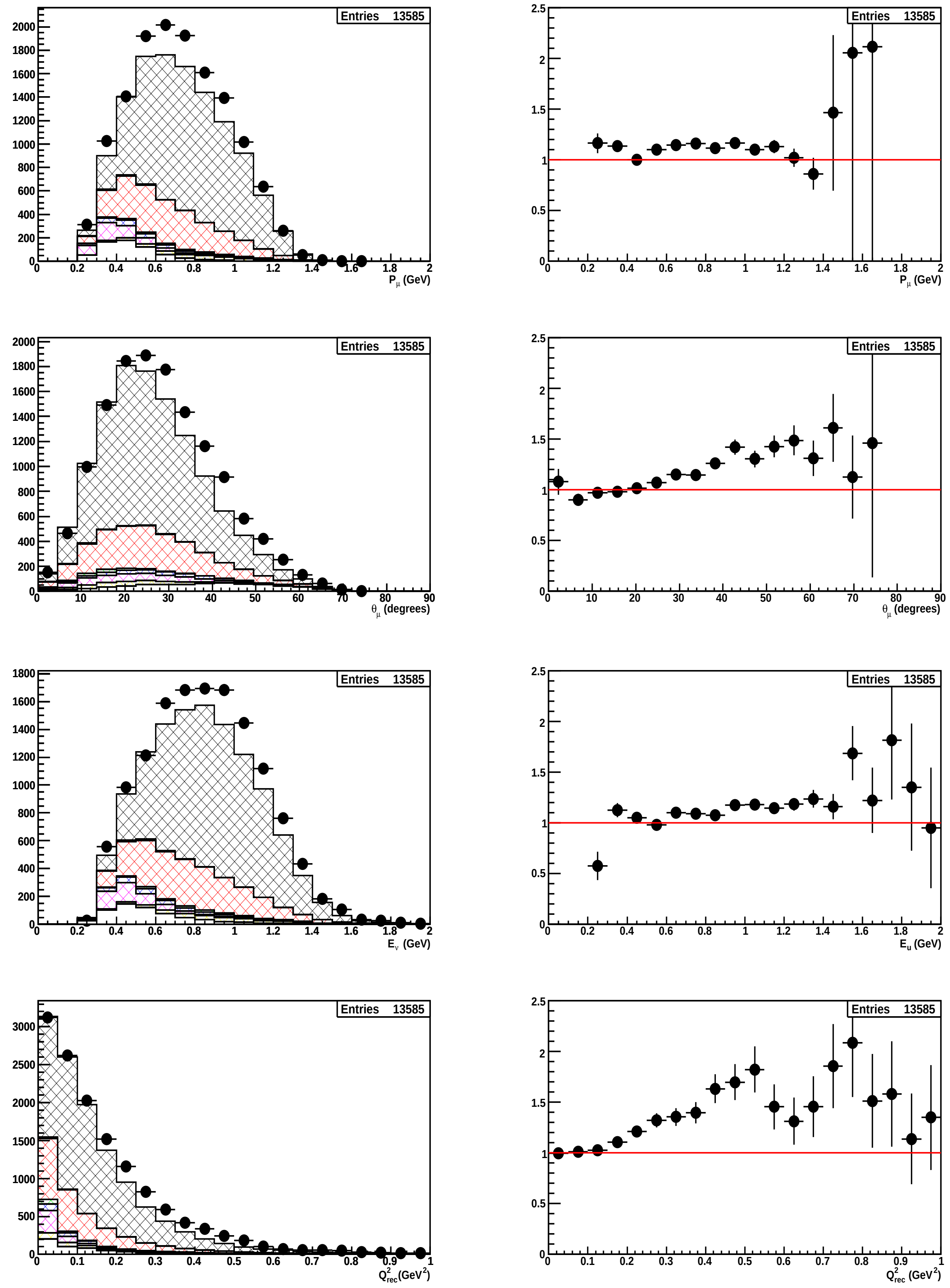

Figure E.2: Muon (P_μ, θ_μ) and event (E_ν, Q^2) kinematic distributions for 1-track sample. Right hand plots shows data/MC ratio of each distribution. MC is normalized to POT.

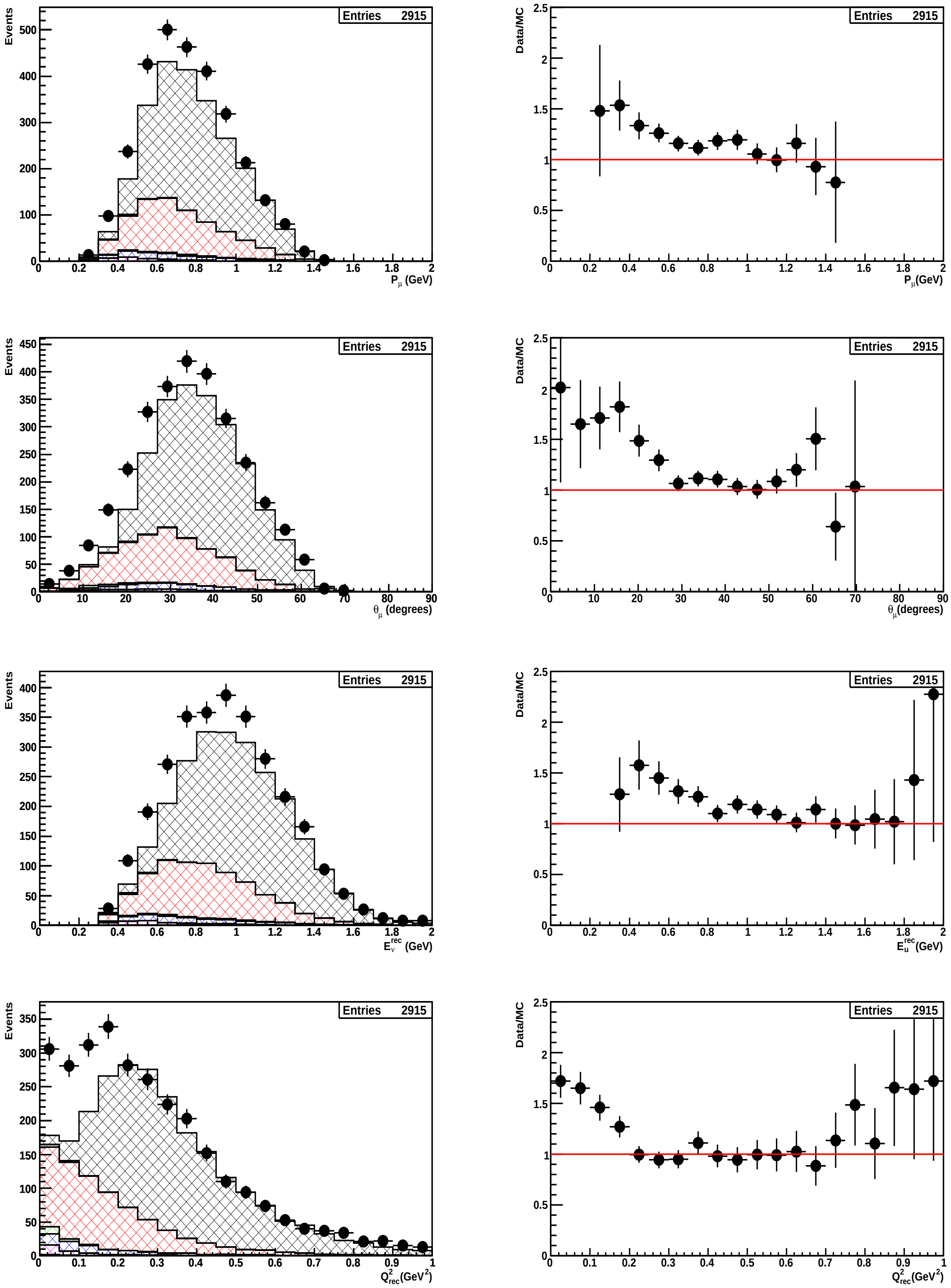

Figure E.3: Muon (P_μ, θ_μ) and event (E_ν, Q^2) kinematic distributions for 2-track QE enriched sample. Right hand plots shows data/MC ratio of each distribution. MC is normalized to POT.

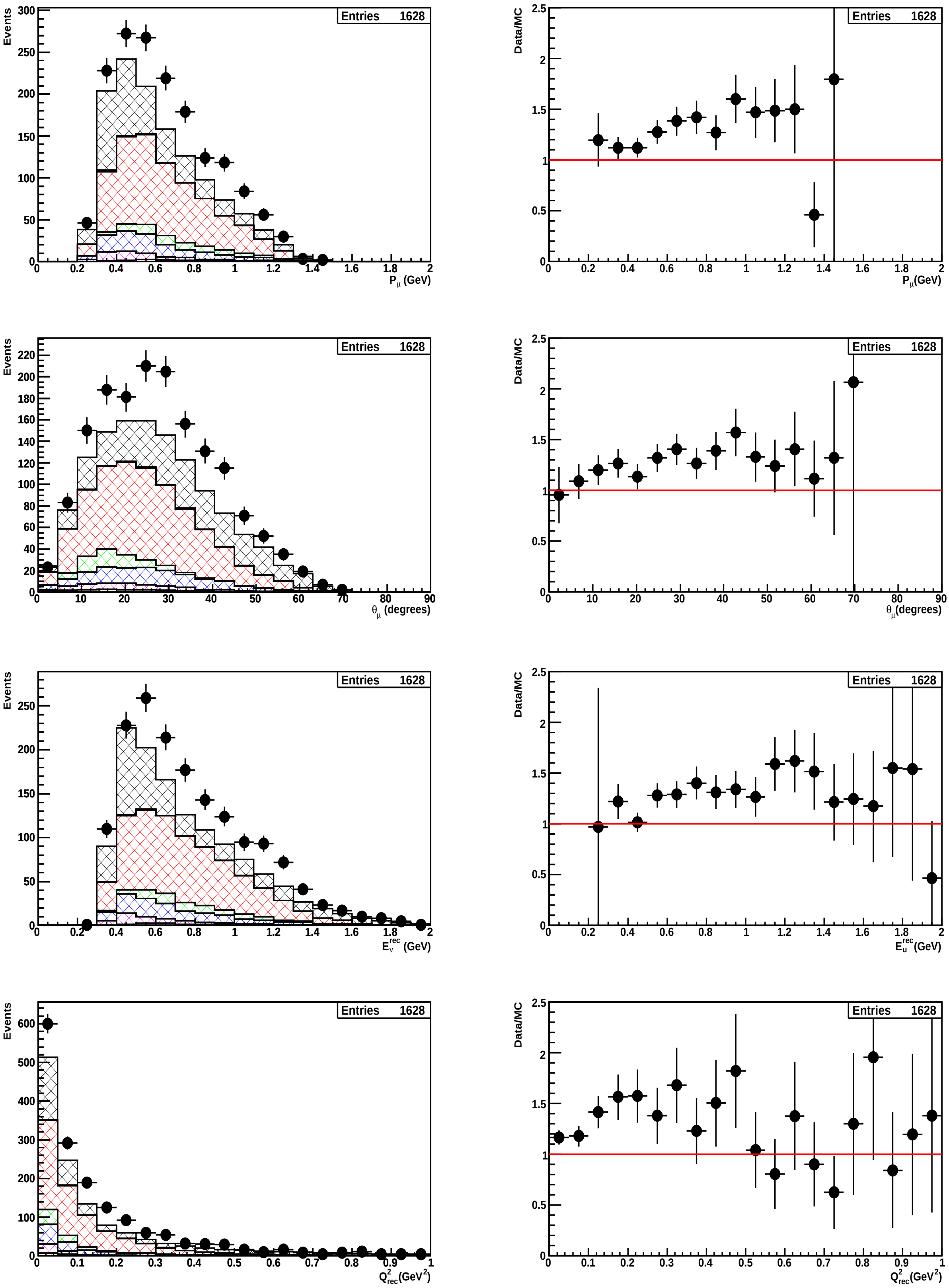

Figure E.4: Muon (P_μ, θ_μ) and event (E_ν, Q^2) kinematic distributions for 2-track nonQE enriched sample. Right hand plots shows data/MC ratio of each distribution. MC is normalized to POT.

Appendix F

The kinematic cut $\Delta\Theta_p$

The $\Delta\Theta_p$ is a kinematic cut used in CCQE analysis to distinguish between the CCπ and CCQE interactions. The $\Delta\Theta_p$ is the angle between the predicted and the observed proton. The predicted proton angle is calculated assuming CCQE kinematics.

Figure F.1 shows the $\Delta\Theta_p$ distribution for the 2-track enriched QE sample using NEUT MC. A high data/MC disagreement is observed for $\Delta\Theta_p < 20$ degrees. This data disagreement could be related with the data defficit observed at low Q^2_{rec} region in the 2-track QE sample. However, $\Delta\Theta_p$ distribution takes even higher data/MC discrepancies using NUANCE, as figure F.2 shows. The reason is that NUANCE CCπ predicted fraction is higher than in NEUT.

The optimal cut to reject CCπ events is around 25 degrees. However, the resultant CCQE selection after this cut, containing the events below 28 degrees, suffers from high data defficit in comparison with MC. That fact could bias the CCQE cross section measurement during the data/MC fits. For such a reason this cut has not been included in the analysis.

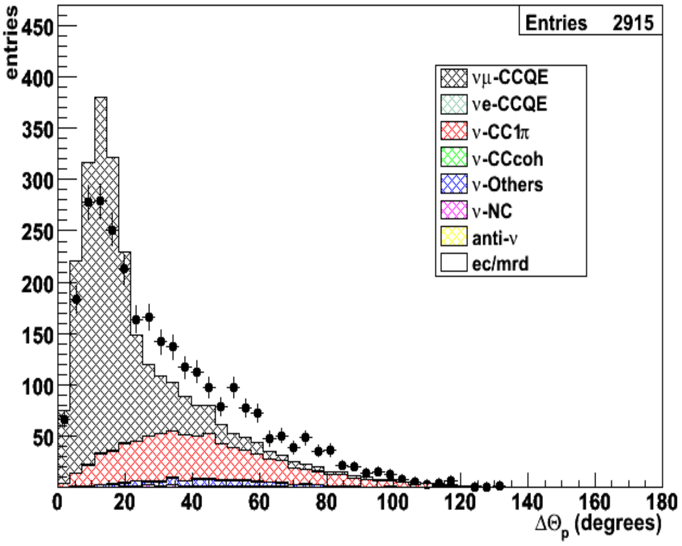

Figure F.1: $\Delta\Theta_p$ distribution for the 2-track enriched QE sample using NEUT MC. The MC is SciBar-MRD normalized.

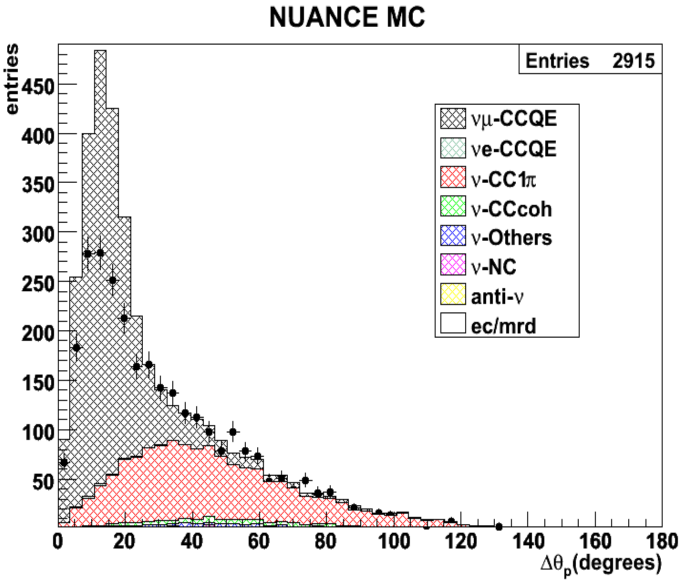

Figure F.2: $\Delta\Theta_p$ distribution for the 2-track enriched QE sample using NUANCE MC. The MC is SciBar-MRD normalized.

Appendix G

Neutrino-nucleus cross section at high Q^2 region

The sample selection from the SciBooNE data populates low Q^2 regions, with more than 66% of the total event selection below 0.2 GeV^2. At low Q^2 region, the modeling of the nuclear effects become relevant. Figure G.1 shows the cross section considering high Q^2 values, i.e., excluding events with $Q^2 < 0.15$ GeV^2. Note that, the nominal cross section (red dots) takes lower values compared with the cross section at high Q^2 region (blue dots). Both cross section only shows statistical errors. This behavior may be explained by the fact that more realistic nuclear effects trend to modify the cross section to lower values.

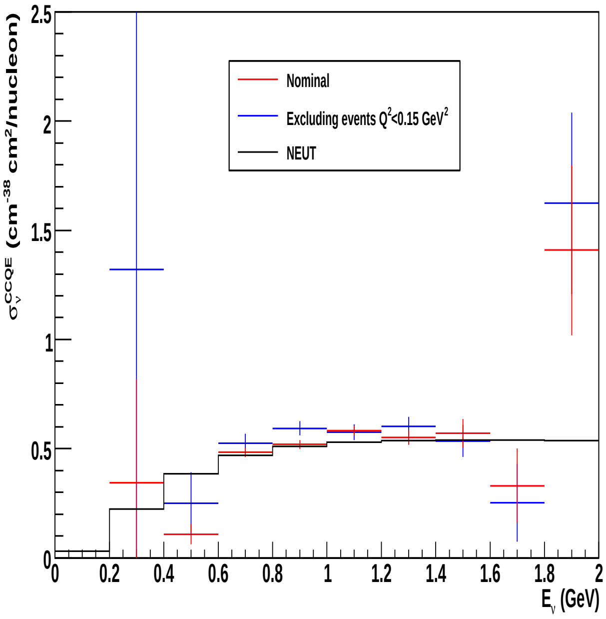

Figure G.1: Absolute CCQE cross section taking only high Q^2 events (blue dots) in comparison with nominal cross section (red dots). Only statistical errors are shown.